Measurement of the Low-x Behaviour of the Photon Structure Function F_2^γ

Edmund Clay
Department of Physics and Astronomy
University College London

Submitted for the degree of
Doctor of Philosophy
June 2000

Abstract

The photon structure function $F_2^\gamma(x, Q^2)$ has been measured using data taken by the OPAL detector at e^+e^- centre-of-mass energies of 91 GeV, 183 GeV and 189 GeV, over the Q^2 ranges 1.5–30.0 GeV^2 (LEP1), and 7.0–30.0 GeV^2 (LEP2), probing lower values of x than any previous experiment. New Monte Carlo models and new methods, including multi-variable unfolding, have been used to reduce model dependent systematic errors in the measurement of F_2^γ.

Acknowledgements

Firstly, I would like to thank my supervisor, David Miller, for introducing me to two-photon physics and for guidance throughout the course of my PhD. Jan Lauber was my second supervisor at UCL during the first two years and taught me many of the techniques used in the analysis. Richard Nisius also provided much assistance, especially with producing the OPAL paper for this analysis. He also calculated the radiative corrections used in this thesis. I thank the OPAL collaboration for running an efficient experiment, especially the Two Photon group and the editorial board for the paper, who improved greatly the quality of the analysis. The computing staff at UCL were very helpful in solving computer problems. This analysis would not have reached as far without the work of previous OPAL students. Those who were there before me include Jörg Bechtluft, Jason Ward, Tony Rooke and Edward McKigney.

I am grateful to my family for (firstly) putting up with long absences while I was at CERN, and (secondly) because I was living at home for the last three months of writing this thesis. While I was at CERN, many people provided support in the areas of drinking and skiing. Thanks especially to Max Sang for his skiing lessons - I didn't suffer any permanent injuries.

My PhD was funded by PPARC, and RAL and the UCL Graduate School provided additional travel funds. I thank the Birmingham University particle physics group for providing a terminal during the last three months.

Contents

List of Figures

List of Tables

Chapter 1

Introduction

The photon is the carrier of the electromagnetic force, and one of the fundamental particles of nature. In classical electrodynamics, the behaviour of photons is governed by Maxwell's equations, which are linear. This means that classically there is no structure in the photon, and in this theory it is not possible for two photons to interact. However, in quantum electrodynamics it is possible for a photon to fluctuate, for a brief period, into a pair of charged particles such as electrons or quarks. The pair always consists of a particle and its anti-particle. If there is no other particle present, the pair will recombine to form the photon again. But if a second photon enters the

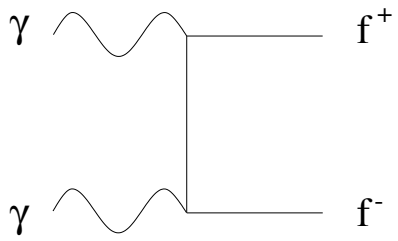

Figure 1.1: Production of a fermion–antifermion pair from two photons in QED.

picture, it may interact with one of the charged particles, so that the first photon is broken up. Thus by studying the interactions of two photons, it is possible to learn about the internal structure of the photon.

Figure 1.2: An aerial view of LEP.

Figure 1.1 shows the simplest two-photon interaction, in which the photons produce a pair of charged particles. The particles produced may be leptons or quarks, which produce a hadronic final state. In the case of leptons, the interaction can be calculated exactly using QED. However, hadronic photon interactions are not completely calculable because some parts of the solution are non-perturbative.

Much of the theoretical interest in photon structure is related to existing

ideas about proton structure, which has been measured accurately by a series of experiments beginning at SLAC [1] in the late 1960s. Some features of proton structure may be reflected in photon structure also, but photon structure has not been measured nearly so accurately.

The first measurements of hadronic photon structure were made in the early 1980s at the PETRA collider. This was an e^+e^- collider operating at a centre-of-mass energy of about 30 GeV. In $\gamma\gamma$ interactions at e^+e^- colliders, both the photon target and the photon probe are emitted from the beam electrons[1]. This means that the energy of the target is unknown, and must be reconstructed from the final state. Because is is not always possible to observe the whole of the final state, measurements of photon structure [2–19] do not have the accuracy of their proton counterparts.

The most recent measurements of photon structure have been made at LEP collider at CERN (Figure 1.2). Experiments at LEP are able to make these measurements over a large kinematic range, due to the high energy of the beams, and thus investigate many areas of photon physics.

This thesis describes a study of the hadronic photon structure function, using data from the OPAL experiment, at e^+e^- centre-of-mass energies of 91 GeV, 183 GeV and 189 GeV, collected during the years 1993–1995, and 1998.

[1] For conciseness, positrons are also referred to as electrons.

Chapter 2

LEP and OPAL

2.1 LEP

The LEP (Large Electron Positron) collider is an e^+e^- storage ring at CERN which began operating in 1989. It has a circumference of 27 km and is located 100 m underground. Four experiments are situated at symmetrical collision points around the ring: OPAL, ALEPH, DELPHI and L3. The layout of LEP is shown in Figures 2.1 and 2.2.

During the first phase of LEP (LEP1), from 1989–1995, the centre-of-mass energy of the electron and positron beams was close to the mass of the Z^0 particle at 91 GeV. The energy was increased for the LEP2 phase; first to 161 GeV to produce W^+W^- pairs, then in steps of a few GeV up to 189 GeV by 1998.

LEP has curved sections containing dipole magnets for bending the beams, with quadrupole and sextupole magnets for focusing, and four long, straight sections containing the accelerating cavities and the experiments. The accelerating components were originally room-temperature copper cavities, but many superconducting cavities have been added as part of a continuous upgrade process in order to increase the beam energy during the LEP2 phase.

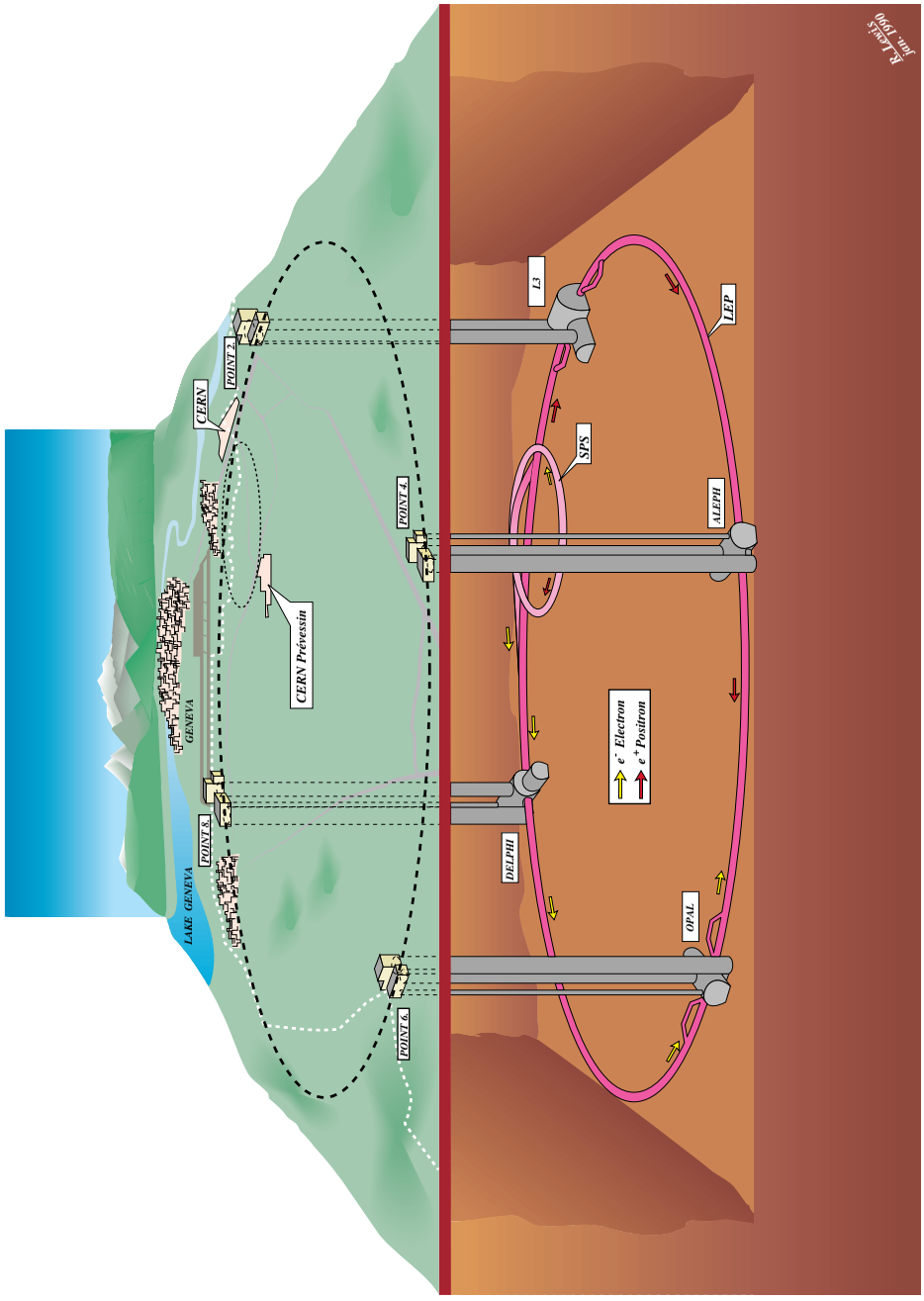

Figure 2.1: A diagram of the LEP ring, showing the positions of the CERN site and the four LEP experiments.

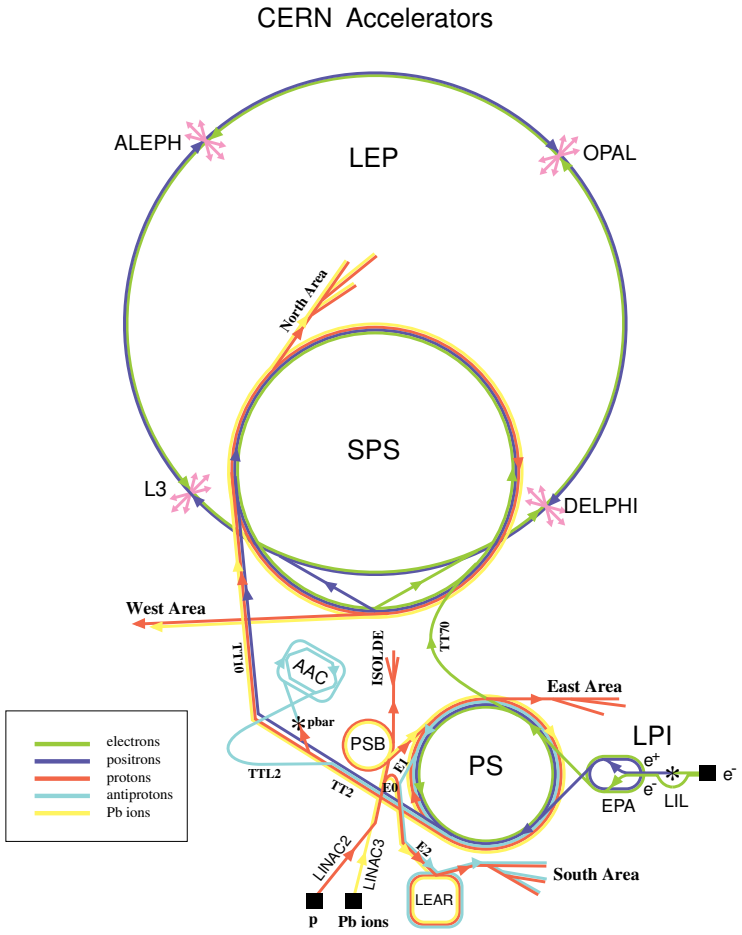

LEP: Large Electron Positron collider
SPS: Super Proton Synchrotron
AAC: Antiproton Accumulator Complex
ISOLDE: Isotope Separator OnLine DEvice
PSB: Proton Synchrotron Booster
PS: Proton Synchrotron
LPI: Lep Pre-Injector
EPA: Electron Positron Accumulator
LIL: Lep Injector Linac
LINAC: LINear ACcelerator
LEAR: Low Energy Antiproton Ring

Rudolf LEY, PS Division, CERN, 02.09.96

Figure 2.2: The CERN accelerator complex (not drawn to scale).

LEP was designed to use the existing accelerator system at CERN as an injector. The process begins in the LIL (LEP Injection Linac), where electrons from an electron gun are accelerated to 600 MeV. Positrons are produced by colliding some of the electrons with a fixed target. Particles from the LIL are accumulated in the EPA (Electron Positron Accumulator) into four or more bunches each of electrons and positrons. The bunches are injected into the PS (Proton Synchrotron) ring and accelerated to 3.5 GeV, then into the SPS (Super Proton Synchrotron) ring where they are accelerated to 20 GeV. The PS and SPS accelerators can accelerate different types of particle in a complex cycle, so fixed target experiments using protons can operate at the same time as LEP. From the SPS the beams are injected into LEP and accelerated to the final collision energy. The process of filling LEP takes 15-30 minutes, after which the beams can be collided for several hours, while the four experiments collect data.

2.2 Bunch modes in LEP

The electron and positron beams in LEP are made up of a number of bunches containing $\sim 10^8$ electrons or positrons. Various bunch modes may be used. From 1989 to 1992, LEP was operated with 4 bunches in each beam (4+4 bunch mode). In 1992 this was changed to 8+8 bunch mode to increase the luminosity. From 1995 onwards, LEP has used bunchtrains, containing up to 4 bunches each, with 4 bunchtrains in each beam.

2.3 OPAL

The OPAL (Omni Purpose Apparatus for LEP) [20] experiment has been operational since the start of LEP in 1989. It was designed to detect, classify and reconstruct a wide variety of events that can occur in e^+e^- collisions.

The main feature of OPAL are

- tracking of charged particles and vertex reconstruction in the central detector,
- detection (and identification in the central region) of photons and electrons,
- measurement of hadronic energy,
- identification of muons, and
- luminosity measurement by detecting electrons scattered at small angles.

A diagram of OPAL is shown in Figure 2.3. OPAL has numerous subdetectors, each of which has a two-letter shorthand name. For convenience, this convention is adopted in the following sections. Outside the central region, each subdetector is in two parts, one on either side of the detector.

2.3.1 The OPAL coordinate system

In the OPAL right-handed coordinate system, the x-axis points towards the centre of LEP and the z-axis points in the direction of the e^+ beam. This defines a y-axis a few degrees away from the vertical. Spherical and cylindrical coordinates are also used, with (r,θ,ϕ) defined in the usual way. The right and left sides of OPAL are defined such that right is the positive z direction.

2.3.2 The magnet

The magnet consists of a solenoidal coil and an iron yoke. It produces a nearly uniform magnetic field of 0.435 T within the tracking region. The yoke serves as part of the hadronic calorimeter, providing 4 interaction lengths of material for hadrons.

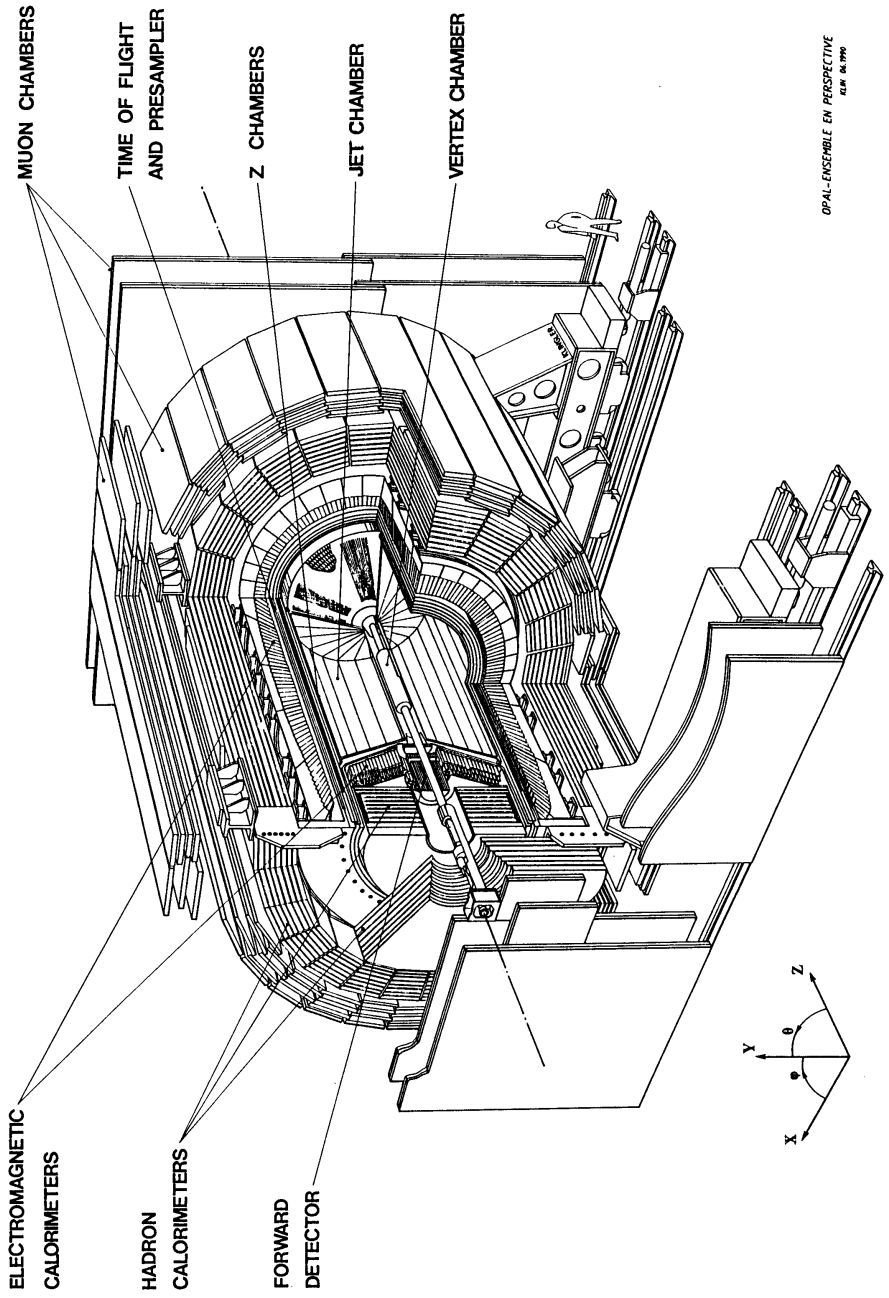

Figure 2.3: A cut-away diagram of OPAL showing the locations of the main subdetectors.

2.3.3 The central tracking system (CT)

The tracking detectors are designed to measure the momentum of charged particles. They are contained within a 4 bar pressure vessel at the centre of OPAL. The largest part of the tracking system is the jet chamber. Outside the jet chambers are the Z chambers, which give an improved measurement of the z position of tracks. A vertex chamber detects charged particles closer to the interaction region and finds secondary vertices. Between the pressure vessel and the beam pipe is the silicon microvertex detector, which accurately measures the primary vertex and the decays of particles such as τ leptons and heavy flavour hadrons.

The jet chamber (CJ)

CJ measures the momentum of charged particles with good spatial resolution of tracks and the possibility of particle identification. It is 4 m long, with an inner radius of 0.25 m and and outer radius of 1.85 m. It is divided into 24 sectors each with 159 sense wires parallel to the beam. Cathode wires planes form the boundaries between the sectors. CJ covers 98% of the total solid angle with at least 8 wire hits on a track (out of a maximum of 159).

The coordinates r and ϕ of a hit are determined accurately from the drift time and the wire positions; z is found by the charge division method using the integrated charge at both ends of the wire. The energy loss $\mathrm{d}E/\mathrm{d}x$ of a particles is measured from the total charge reaching the signal wires, and is used for particle identification.

The typical spatial resolution of CJ is 135 μm in r–ϕ, and 6 cm in z. The momentum resolution is $\sigma_p/p^2 = 2.2 \times 10^{-3}$ GeV^{-1}.

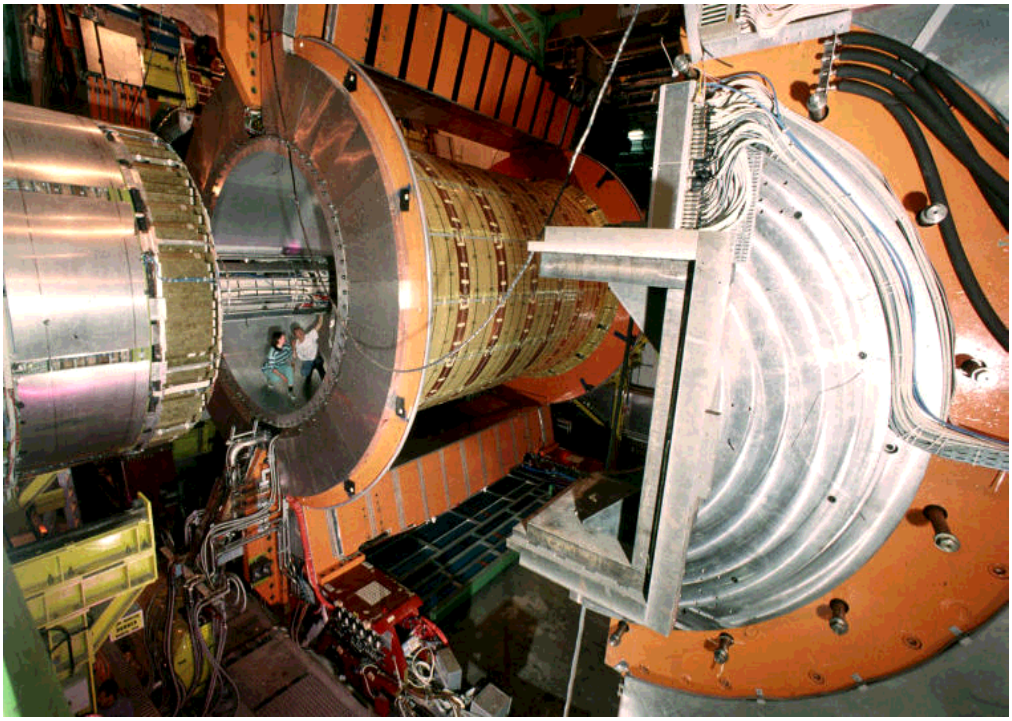

Figure 2.4: The OPAL experiment, opened to expose the central barrel region. Also visible on the left is one of the endcap electromagnetic calorimeters.

The Z chambers (CZ)

CZ is used to give a better z measurement for charged particles after they leave CJ, which has poor z resolution because of the orientation of the sense wires. CZ forms a barrel around CJ. It consists of 24 drift chambers, each 4 m long, 0.5 m wide and 59 mm thick. Each drift chamber is divided into 8 sections in the z direction, with 6 sense wires in each section.

The average z resolution of CZ is 150 μm.

The vertex chamber (CV)

CV is designed to find secondary vertices from particle decays by providing precise positional measurements of charged particles close to the interaction region. It surrounds the carbon fibre pressure pipe, inside the jet chamber. CV is a 1 m long cylindrical drift chamber with radius 0.24 m. It has an inner layer of 36 axial cells with 12 wires along the beam direction, and an outer layer of of 36 stereo cells with 6 wires each, at 4 degrees to the beam direction. The axial cells have an average resolution in r–ϕ of 55 μm, and give a coarse z measurement which is used for fast triggering. The combination of axial and stereo cells provides accurate measurements in r, ϕ and z.

The silicon microvertex detector (SI)

SI is the closest subdetector to the interaction region, and is used to accurately locate the position of the primary vertex and to find secondary vertices from the decays of particles such as τ-leptons and heavy flavour hadrons. It is inside the carbon fibre pressure tube, outside the beam pipe. SI was first installed in 1991 as two barrels of silicon wafers providing measurements in r–ϕ. Further wafers were added in 1993 to allow z measurements.

The resolution of SI is 5 μm in r–ϕ and 13–20 μm in z, depending on the angle of the particle.

2.3.4 The time of flight system (TOF)

The time-of-flight system is used for triggering and identification of charged particles. It also helps to reject cosmic rays.

Time of flight barrel (TB)

TB covers the barrel region outside the solenoid, for $|\cos\theta| < 0.82$. It consists of 160 6.84 m long scintillation counters. Light from the scintillators is

collected at the ends of each counter via lightguides glued to phototubes.

The time resolution of TB is about 300 ps.

The tile endcap (TE) and MIP plug

TE [21] was installed in 1996 to enhance the triggering information from the forward region. It is located between the pressure bell and the endcap electromagnetic presampler. The tile-based design was used because of severe space constraints and the high magnetic field in that region. A 10 mm scintillating layer is read out with wavelength shifting fibres and phototubes. The timing precision is about 5 ns, which is sufficient to determine unambiguously the collision time when LEP is operating in bunchtrain mode.

The MIP plug was added in 1997 as an low-angle extension to TE. It is used as a muon veto, and to detect forward particles. It partly overlaps with the gamma catcher (see Section 2.3.8).

2.3.5 Electromagnetic calorimetry (ECAL)

The electromagnetic calorimeters detect and measure the energy of electrons and photons. They are made of lead glass blocks which provide total absorption of electromagnetic showers. They are outside the pressure vessel and the coil - which present about 2 interaction lengths of material to electrons and photons - making presamplers necessary for accurate energy measurement.

The barrel electromagnetic presampler (PB)

PB is located outside the coil and in front of the lead glass. It has 16 chambers with 2 layers of limited streamer mode tubes, covering a cylinder of radius 2.39 m and length 6.62 m.

The resolution in r–ϕ for a single charged particle is 1–2 mm depending on the angle, and the resolution in z is about 10 cm. The energy resolution for

the combined presampler and lead glass calorimeter is given in the following section.

The barrel lead glass calorimeter (EB)

EB has 9440 lead glass blocks, instrumented with magnetic field tolerant phototubes. The blocks point at the interaction region, tilted slightly to remove gaps. EB covers the region $|\cos\theta| < 0.82$. The energy resolution including information from the presampler is $\sigma_E/E \approx 10\%/\sqrt{E}$, where E is in GeV.

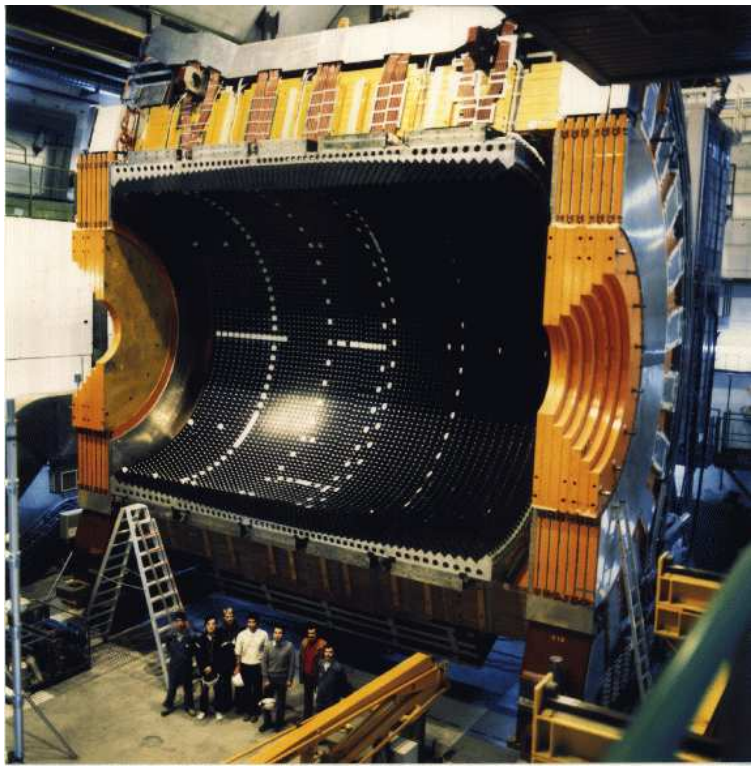

Figure 2.5: A picture taken during the construction of OPAL, showing half of the barrel lead glass calorimeter.

The endcap electromagnetic presampler (PE)

PE is located between the pressure bell and the lead glass calorimeters (TE was installed in front of PE in 1996). It consists of 32 thin multiwire chambers at each end of OPAL.

The resolution in r–ϕ is 2–4 mm, and the resolution in θ is about 4.6 mrad.

The endcap electromagnetic calorimeter (EE)

Like the barrel electromagnetic calorimeter, EE uses an array of lead glass blocks. They are not pointing at the interaction region but are coaxial with the beam line. The readout system uses single stage multipliers known as vacuum photo triodes, which are able to operate in the full axial field of the magnet.

The energy resolution of EE is $\sigma_E/E \approx 5\%/\sqrt{E}$, where E is in GeV.

2.3.6 Hadron calorimetry (HCAL)

The electromagnetic calorimeters totally absorb electrons and photons, but present only about 2.2 interaction lengths of material to hadrons. The remaining hadronic energy is measured by the hadron calorimeter. The iron yoke of the magnet is segmented into layers, with planes of detectors between the layers. The hadron calorimeter is divided into three parts, together covering 97% of the total solid angle: the barrel, the endcaps and the pole tips.

Hadron endcap and barrel calorimeters (HB/HE)

There are 9 layers of chambers in the barrel calorimeter, alternating with slabs of iron. Each end is closed by a doughnut-shaped endcap, with 8 layers of chambers and iron. The active elements of the detectors are limited streamer tubes, with wires parallel to the beam in the barrel and horizontal in the endcaps. The signal is read out from pads; the wires are used only

for monitoring purposes. Layers of pads are grouped together to form towers which divide the solid angle into 976 equal elements.

The energy resolution is typically $\sigma_E/E \approx 120\%/\sqrt{E}$, where E is in GeV.

The hadron pole-tip calorimeter (HP)

The pole-tip calorimeters extend the coverage of the hadronic calorimeters to $|\cos\theta| < 0.99$. To avoid perturbing the magnetic field, the gap between the iron layers is only 10 mm compared to 25 mm in the barrel and endcaps. The detectors are thin multiwire chambers, similar to those in the endcap electromagnetic presampler.

The energy resolution is $\sigma_E/E \approx 100\%/\sqrt{E}$ for 15 GeV hadrons, where E is in GeV, but degrades at higher energies due to leakage.

2.3.7 The muon detectors (MB/ME)

Muons, like hadrons but unlike electrons, tend to pass through the electromagnetic calorimeters. The muon detectors are outside the hadronic calorimeters. Muons are identified by matching tracks in the muon detectors and the central tracking detectors. The main background is from hadrons which either fail to interact before the muon detectors or produce secondary particles which give tracks in the muon detector.

The barrel part of the muon detector (MB) consists of 110 drift chambers in 4 layers covering $|\cos\theta| < 0.68$, while the endcaps (ME) extend the coverage to $|\cos\theta| < 0.98$ with limited streamer tubes.

2.3.8 The forward detector (FD)

The forward detector's main uses are to measure luminosity by counting Bhabha events and to tag low-angle electrons in two photon events. There are four parts to the forward detector: the main calorimeter, the tube chambers,

the gamma catcher and the far forward monitor. Two other components of the forward detector, the fine luminosity monitor and the drift chambers, were removed between the 1992 and 1993 running periods in order to make room for the silicon tungsten detector (Section 2.3.9). The layout of the forward detectors is shown in Figure 2.6.

The forward calorimeter (FK)

The main calorimeter of FD has 35 layers of lead-scintillator sandwich, presenting 24 radiation lengths of material to electrons. Hadronic showers are not well contained by FK, leading to poor hadronic energy measurement in the forward region. The first four layers are a presampler, and are read out on the outer edge only. The remaining layers are read out on the inner and outer edges, giving a coarse measurement of θ. There are 16 azimuthal sectors, giving a ϕ measurement from the ratio of signals in adjacent sectors.

The energy resolution of FK is $\sigma_E/E \approx 17\%/\sqrt{E}$, where E is in GeV.

The tube chambers (FB)

The tube chambers give a more accurate measurement of the position of showers than the calorimeters, and are situated between the presampler and the rest of the main calorimeter. There are three layers of proportional tubes; the first two are at right angles to each other and the third lies diagonally across the other two.

The resolution is about 2 mrad in θ and ϕ.

The gamma catcher (FE)

FE is non-containing calorimeter which fills the gap between FK and EE. It consists of 7 layers of lead-scintillator sandwich in 8 azimuthal sections.

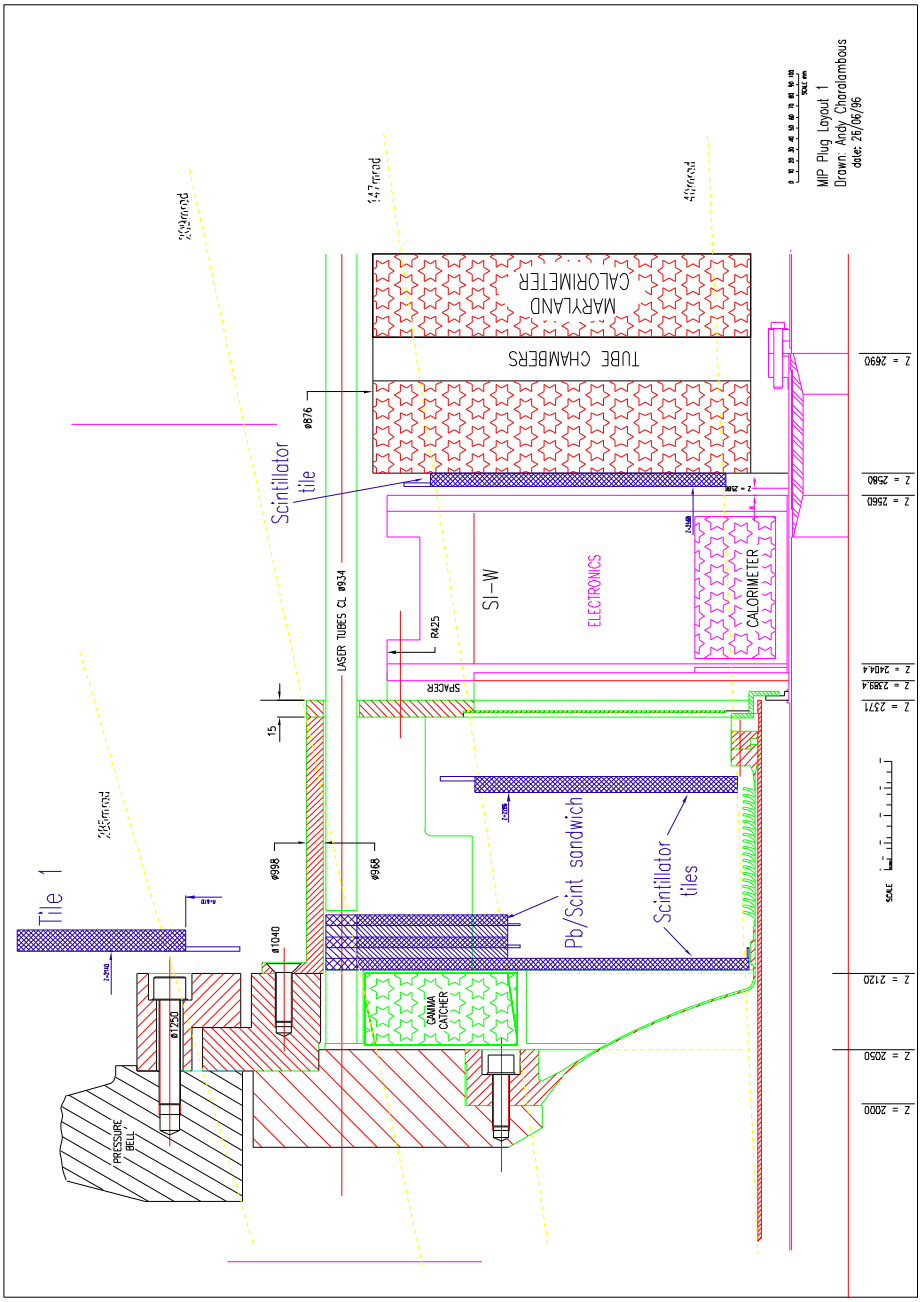

Figure 2.6: A diagram of the layout of the forward detectors, showing the silicon-tungsten calorimeter, the main forward calorimeter, the tube chambers, the gamma catcher and the MIP-plug (labelled as 'scintillator tiles').

The far forward monitor (FF)

FF consists of two small lead-scintillator calorimeters 7.7 m from the interaction point, on either side of the beam pipe. Its main use is for online luminosity measurements, but it can also be used for tagging very low-angle electrons, and has recently been upgraded to improve the positional measurement of electrons [22].

2.3.9 The silicon tungsten detector (SW)

The silicon tungsten detector was installed between the 1992 and 1993 running periods in order to provide a more accurate luminosity measurement than is possible with FD. It covers the region in θ from 25–59 mrad. For LEP2 running, a shield was installed to protect the central tracking detectors from synchrotron radiation. This moved the lower edge of the useful SW acceptance to 33 mrad. SW has 19 layers of silicon detectors interleaved with 1–2 radiation lengths of tungsten, with a layer of silicon in front for presampling. The detector is divided into 16 wedge shaped segments in ϕ, arranged to avoid gaps. Each wedge is divided into 64 pads for positional measurements.

The energy resolution of SW is $\sigma_E/E \approx 24\%/\sqrt{E}$ (where E is in GeV) at LEP 1 energies, and degrades to about 6% at LEP2 energies due to leakage. The angular resolution is about 1 mrad in θ and ϕ.

During 1995, the first year of bunchtrain running, SW could only be read out on every third bunch crossing. This greatly reduced the amount of tagged $\gamma^*\gamma$ data available for that year, while introducing complications for the luminosity measurement. For this reason, the 1995 data with electrons tagged in SW is not used in this analysis.

2.3.10 The trigger

The LEP bunch crossing rate is 45 kHz, which is much faster than the OPAL detector can be read out. By making fast decisions about whether a bunch crossing initiated an interesting physics event, the trigger system [23] reduces the event rate to 1–10 Hz. The trigger also has to reject cosmic rays, beam gas interactions and noise from detector elements. Most events are triggered by multiple independent conditions in different parts of the detector. Having more than one trigger condition increases the trigger efficiency and aids in estimating the efficiency.

There are two types of trigger: those that depend on an energy threshold in a single subdetector, and those that require a coincidence in more than one subdetector, for example a track in CJ and a corresponding cluster in EB, in the same θ–ϕ region.

The trigger system has two levels, the pretrigger and the main trigger. The faster response of the pretrigger was required when LEP was operating in 8+8 bunch mode (1992 to 1994).

The most important trigger signals for selecting $\gamma^*\gamma$ events are listed in Table 2.1. The trigger conditions are programmable, and vary slightly from year to year. More details are given in Sections 5.5.1 and 5.5.2.

2.3.11 The data acquisition system

The different subdetectors have a variety of different readout hardware, and are coordinated from a central control system. If a positive trigger decision is made, data from each subdetector is read out and passed to the event builder and filter, which is a multiprocessor system contained in two VME crates. The filter takes data from the event builder and is able to make a more sophisticated decision than the trigger on whether to keep or reject each event. A farm of HP workstations reconstructs and archives the events that pass the filter.

trigger signal	subdetector(s)	description
FDHIOR*	FD	total energy at either end $\geq$ high threshold
SWHIOR	SW	total energy at either end $\geq$ high threshold
TBM1	CT	$\geq$ 1 barrel track
TM1	CT	$\geq$ 1 track
TM2	CT	$\geq$ 2 tracks
TM3*	CT	$\geq$ 3 tracks
EBTOTLO	EB	total barrel energy $\geq$ low threshold
EBWEDGE	EB	energy in 'wedge' $\geq$ threshold
EERLO	EE	total energy on left side $\geq$ low threshold
EELLO	EE	total energy on right side $\geq$ low threshold
EEPRLR	EE	logical OR of left and right pretrigger signals
TPTTTO(B)	CT/TOF	$\geq$ 1 correlated θ-ϕ bin
TPTTEM	CT/ECAL	$\geq$ 1 correlated θ-ϕ bin
TPTOEM(B)*	TOF/ECAL	$\geq$ 1 correlated θ-ϕ bin
TPEML	ECAL	$\geq$ 1 ϕ bin over threshold, left side
TPEMR	ECAL	$\geq$ 1 ϕ bin over threshold, right side
TPTO(1/B)	TOF	$\geq$ 1 θ-ϕ bin
TPEM1	EM	$\geq$ 1 θ-ϕ bin
TBEBS	TB/EB	same ϕ sectors hit
LCALLO	FK	$\geq$ low threshold left
RCALLO	FK	$\geq$ low threshold right

Table 2.1: Description of the OPAL trigger signals. The high and low energy thresholds for each trigger condition vary, especially between LEP1 and LEP2. Those marked with an asterisk are stand-alone triggers, while the rest require coincidences with other triggers.

Chapter 3

Theory of photon structure

3.1 Deep inelastic scattering of quasi-real photons

The kinematics of a two-photon event at an e^+e^- collider are illustrated in Figure 3.1. Each beam electron emits a virtual photon and is scattered. The two photons interact to produce a final state which may be hadronic or leptonic. The case of leptonic final states can be calculated in QED. This study is concerned with hadronic final states, calculation of which involves not only QED but also QCD, in both perturbative and non-perturbative regimes.

The cross-section for two-photon events can be factorised into two parts: a luminosity function, which describes the production of the two photons from the beam electrons, and a term describing the interaction of the two photons. It can be written as [24]

$$\mathrm{d}\sigma_{e^+e^-\to e^+e^-\mathrm{X}} = L_{\gamma\gamma}[\sigma_{\mathrm{TT}} + \epsilon_1\sigma_{\mathrm{LT}} + \epsilon_2\sigma_{\mathrm{TL}} + \epsilon_1\epsilon_2\sigma_{\mathrm{LL}} + \frac{1}{2}\epsilon_1\epsilon_2\tau_{\mathrm{TT}}\cos 2\phi + 2\sqrt{\epsilon_1(1+\epsilon_1)}\sqrt{\epsilon_2(1+\epsilon_2)}\tau_{\mathrm{TL}}\cos 2\phi]\frac{\mathrm{d}p'_1}{E_{\mathrm{tag}}}\frac{\mathrm{d}p'_2}{E_{\mathrm{tag2}}} \quad (3.1)$$

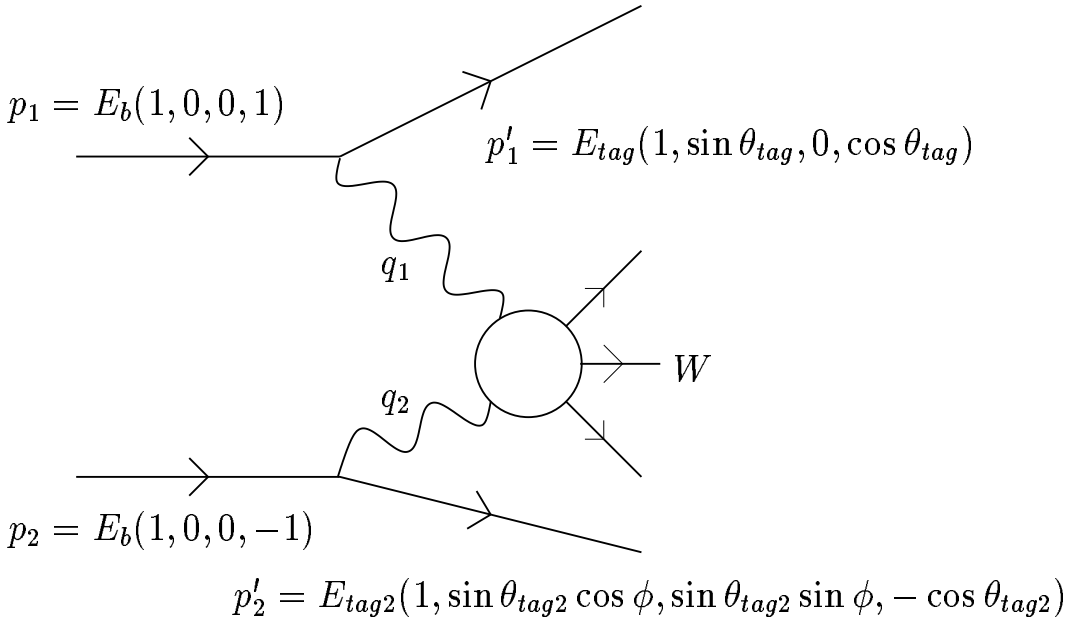

Figure 3.1: Deep inelastic electron-photon scattering.

where X represents the hadronic final state. The photons can be either transversely or longitudinally polarised, so the cross-section has four parts: σ_{TT}, σ_{LT}, σ_{TL} and σ_{LL}. The luminosity function $L_{\gamma\gamma}$ and the factors ϵ_1 and ϵ_2 can be calculated in QED. The interference terms τ_{TT} and τ_{TL} vanish after integration over ϕ, the angle between the scattering planes of the two electrons. This integration is necessary because in the events studied in this thesis, only one of the scattered electrons is observed.

If one of the photons is nearly real, the two-photon interaction can be thought of as deep inelastic scattering (DIS) of an electron from a photon target. It is useful to introduce the usual DIS variables (neglecting the elec-

tron mass):

$$Q^2 = -{q_1}^2 = 2E_bE_{\rm tag}(1-\cos\theta_{\rm tag}) \quad (3.2)$$

$$P^2 = -{q_2}^2 = 2E_bE_{\rm tag2}(1-\cos\theta_{\rm tag2}) \quad (3.3)$$

$$W^2 = (q_1+q_2)^2 \quad (3.4)$$

$$x = \frac{Q^2}{2q_1\cdot q_2} = \frac{Q^2}{Q^2+P^2+W^2} \quad (3.5)$$

$$y = \frac{q_1\cdot q_2}{p_1\cdot q_2} \simeq 1-\frac{E_{\rm tag}}{E_b}. \quad (3.6)$$

The DIS picture is valid when $P^2 \ll Q^2$. This requires that one of the electrons is scattered at a large angle, while the other is scattered at an angle $\theta_{\rm tag2} < \theta_{\rm min}$. The luminosity function $L_{\gamma\gamma}$ peaks for low scattering angles, so the untagged electron will in most cases be scattered at a much lower angle than the tagged electron.

Equation 3.1 can then be integrated over the angular distribution of the undetected electron, to give the cross section for the process $e\gamma \to eX$. In order to make a simple connection with the parton level, the cross section is usually written in terms of the structure functions

$$F_T^\gamma = \frac{Q^2}{4\pi^2\alpha x}\sigma_{\rm TT}, \quad (3.7)$$

$$F_L^\gamma = \frac{Q^2}{4\pi^2\alpha}\sigma_{\rm LT}, \quad (3.8)$$

or

$$F_1^\gamma = \frac{Q^2}{4\pi^2\alpha x}(\sigma_{\rm TT}), \quad (3.9)$$

$$F_2^\gamma = \frac{Q^2}{4\pi^2\alpha}(\sigma_{\rm TT}+\sigma_{\rm LT}). \quad (3.10)$$

This leads ultimately to

$$\frac{{\rm d}^2\sigma_{\rm e\gamma\to eX}}{{\rm d}x{\rm d}Q^2} = \frac{4\pi\alpha^2}{x\,Q^4}\left[(1-y)F_2^\gamma - xy^2F_1^\gamma\right]. \quad (3.11)$$

3.2 Parton distribution functions

The differential cross section for elastic scattering of an electron and a free quark within a hadron or photon can be calculated in QED [25]:

$$\frac{\mathrm{d}^2\sigma_{\mathrm{eq}\to\mathrm{eq}}}{\mathrm{d}x\mathrm{d}Q^2} = \frac{4\pi\alpha^2}{Q^4}(1+(1-y)^2)\frac{1}{2}e_q^2\delta(x-\zeta) \tag{3.12}$$

where e_q^2 is the charge of the scattered quark which carries momentum fraction ζ of the target photon, and travels in the direction of the target photon (i.e. with small transverse momentum). Rearranging Equation 3.11 gives

$$\frac{\mathrm{d}^2\sigma_{\mathrm{e}\gamma\to\mathrm{eX}}}{\mathrm{d}x\mathrm{d}Q^2} = \frac{2\pi\alpha^2}{x\,Q^4}\left[\left(1+(1-y)^2\right)F_2^\gamma(x,Q^2) - y^2F_{\mathrm{L}}^\gamma(x,Q^2)\right]. \tag{3.13}$$

It can be seen by comparing Equations 3.12 and 3.11 and integrating over the momentum fraction carried by the struck quark, that in the leading order DIS model,

$$\begin{aligned} F_2 &= \sum_{q,\overline{q}}\int x{e_q}^2\delta(x-\zeta)q(\zeta)\mathrm{d}\zeta \\ &= \sum_{q,\overline{q}} x{e_q}^2 q(x) \end{aligned} \tag{3.14}$$

where $q(x)$ is the parton distribution function (PDF) for a quark of type q within the hadron. The sum runs over all quarks and anti-quarks with $4{m_q}^2 < W^2$. The delta function ensures that the momentum fraction of the scattered quark is equal to the variable x, which was defined previously in terms of the final state quantities. The longitudinal cross-section is zero in the leading-order parton model; this is because a real spin $\frac{1}{2}$ quark cannot absorb a longitudinal photon. However, this is clearly not the complete picture even in QED, because of the restriction on the transverse momentum of the target quark.

In next-to-leading order (NLO), the quark–photon scattering process is one step removed from the parton distribution functions. The quark can emit

a gluon before interacting, or a gluon can become a quark–antiquark pair and thus interact with the photon, which is impossible in the leading order calculation. There is also the possibility that the struck quark came directly from the target photon; thus the NLO picture includes the direct photon–photon interaction of QED. The transverse momentum of the struck quark is no longer required to be small, which has important consequences for the Q^2 evolution of the structure function. F_L is non-zero in NLO. Because the direct contribution is so important, it is generally included in LO parameterisations of F_2^γ, although it is strictly a NLO term.

There are several factorisation schemes for NLO structure function parameterisations, in which different NLO terms are absorbed into the definition of the parton distribution functions. In the DIS scheme, all the NLO terms are absorbed, leading to a definition of F_2^γ that is identical to the LO case (Equation 3.14). The other extreme is the $\overline{\text{MS}}$ (Minimal Subtraction) factorisation scheme, in which only certain divergent parts are absorbed. Also commonly used is the DIS_γ factorisation scheme, in which only the direct term and the divergent parts are absorbed.

3.3 Theoretical models of photon structure

3.3.1 QED calculation of F_2^γ

If the interaction of quarks with gluons is ignored, the photon structure functions can be calculated within QED. The result in the limit of light quark mass and a real target photon is [26]

$$\begin{aligned} F_2 &= 3\alpha \sum_q \frac{{e_q}^4 x}{16\pi^2} \left[(1 - 2x + 2x^2) \ln \frac{Q^2(1-x)}{x{m_q}^2} - x + 8x^2(1-x) \right] \\ F_L &= 3\alpha \sum_q \frac{{e_q}^4 x}{4\pi^2} x^2(1-x) \end{aligned} \tag{3.15}$$

where the sum runs over all quark flavours with $4{m_q}^2 < W^2$. The QED structure function is shown in Figure 3.2. QCD corrections [26] to Equation 3.15 show that at asymptotically high Q^2, while the shape of the structure functions is altered by quark–gluon interactions, the Q^2 dependence remains the same; $F_2 \propto \ln Q^2$. The QED result corresponds to the direct photon term of the next-to-leading order DIS model. For the proton, the prediction of scaling violations and non-zero F_L requires gluon interactions, yet these effects are already present for the photon in free quark theory. Because of this, the direct term is sometimes referred to as the 'anomalous' part of the photon structure function.

The QED photon structure functions have been measured using the process $e^+e^- \rightarrow e^+e^-\mu^+\mu^-$ [27].

3.3.2 Vector meson dominance

At low Q^2 the hadronic part of F_2^γ is dominant. It is not possible to calculate the shape of the structure function in this region, because the calculation involves non-perturbative QCD. It is possible to calculate the evolution of F_2^γ with Q^2, but a low Q^2 input is still required.

The usual way of approximating F_2^γ at low Q^2 is to use the Vector Meson Dominance (VMD) model. The photon can fluctuate into a vector meson (ρ, ω or ϕ), which has the same quantum numbers as the photon, and thereby interact as a hadron. The vector meson structure functions have not been measured, but can be identified with the pion structure function, which has been measured using the interaction $\pi^- + p \rightarrow \mu^+\mu^- + X$ for $x > 0.2$ [28]. The VMD prediction for F_2^γ is then [24]

$$F_2{}^{\mathrm{VMD}} = 0.2\alpha(1-x). \tag{3.16}$$

Alternatively, a VMD estimate can be obtained from a fit to low-Q^2 $\gamma^\star\gamma$ data. This was done by the TPC/2γ experiment, which parameterised the

VMD component of F_2^γ as [7]

$$F_2^{\rm VMD} = \alpha[0.22x^{0.31}(1.0-x)^{0.95} + 0.06(1.0-x)^{2.5}]. \quad (3.17)$$

These parameterisations are shown in Figure 3.2.

3.3.3 QCD evolution

At asymptotically high values of Q^2, F_2^γ is completely calculable, because the perturbative QCD terms dominate [26]. However, at moderate values of Q^2, from 1–100 GeV^2, neither the asymptotic formula nor the VMD model can be expected to satisfactorily describe $\gamma^\star\gamma$ interactions. The usual approach is to take an input distribution at low Q^2, either from the VMD model or from a fit to $\gamma^\star\gamma$ data, and evolve to higher Q^2 using QCD evolution equations. These equations take into account that at higher Q^2 the available phase space for gluon emission by the struck quark is increased. Since the momentum of the parent quark is shared between the emitted gluon and the quark itself, the average momentum fraction of the struck parton is lowered. Also, the gluons can produce sea quarks with even lower momentum. This means that a shift from high x to low x is expected in the hadronic part of the structure functions as Q^2 increases. In addition, the contribution from the bare photon increases with Q^2 over the whole x range.

For massless quarks, the evolution of the quark distributions $q_i(x,Q^2)$ and the gluon distribution $g(x,Q^2)$ is given by the DGLAP (Dokshitzer-Gribov-Lipatov-Altarelli-Parisi) [29] equations, which to leading order are[1]:

$$\begin{aligned}\frac{{\rm d}q_i(x,Q^2)}{{\rm d}\log Q^2} &= \frac{\alpha}{2\pi}P_{\gamma q}(x) + \\ &\frac{\alpha_s}{2\pi}\int_x^1 \frac{{\rm d}x'}{x'}\left(q_i(x',Q^2)P_{qq}(\frac{x}{x'}) + g_i(x',Q^2)P_{qg}(\frac{x}{x'})\right) \quad (3.18)\end{aligned}$$

[1]For derivations of the DGLAP equations, see [30] or [25].

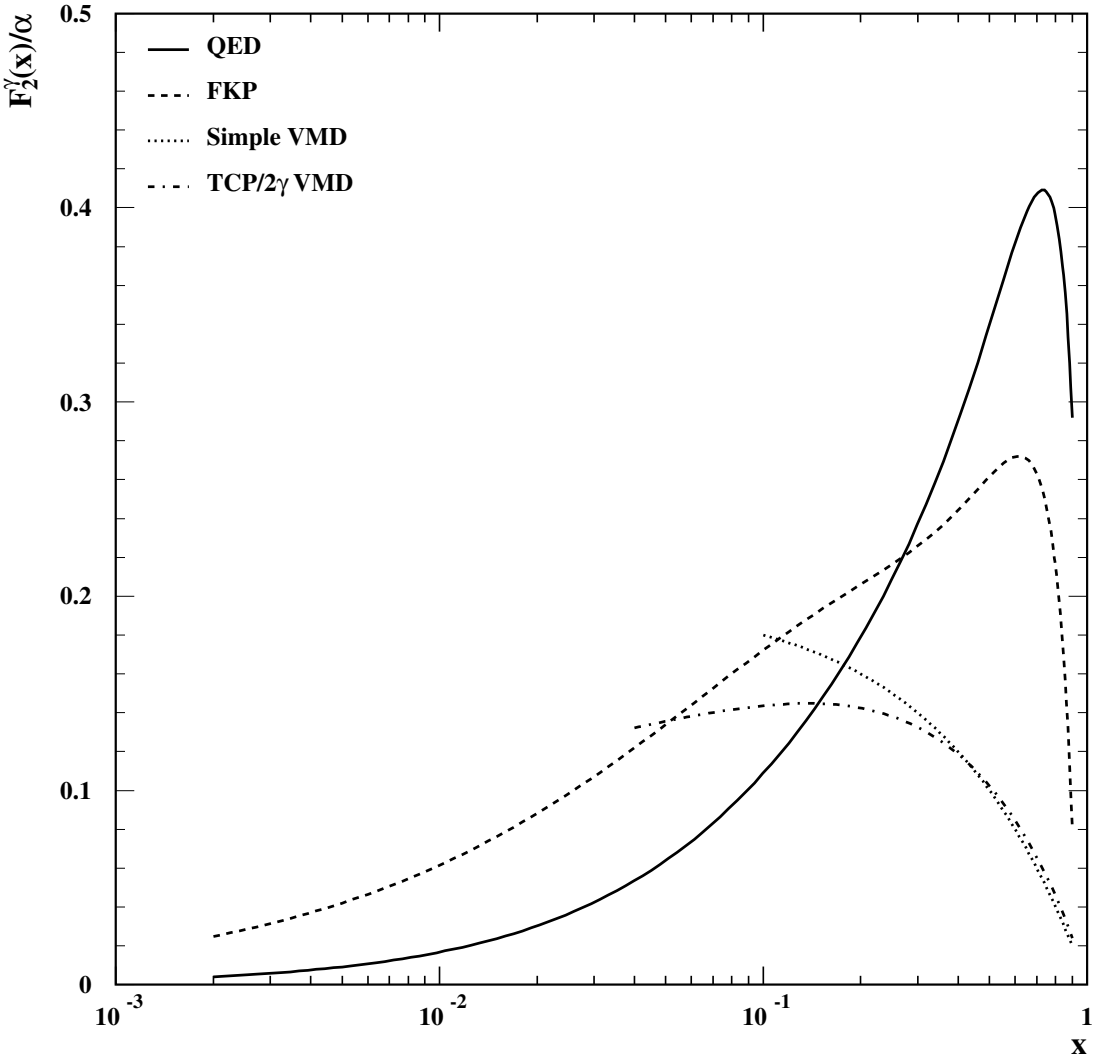

Figure 3.2: Components of F_2^γ according to different models: QED (Equation 3.15) and FKP (Section 3.4.1) at Q^2=10.0 GeV^2, simple VMD (Equation 3.16) and the TPC/2γ VMD parameterisation (Equation 3.17).

$$\frac{\mathrm{d}g_i(x,Q^2)}{\mathrm{d}\log Q^2} = \frac{\alpha_s}{2\pi}\int_x^1 \frac{\mathrm{d}x'}{x'}\left(\sum_i q_i(x',Q^2)P_{gq}(\frac{x}{x'}) + g_i(x',Q^2)P_{gg}(\frac{x}{x'})\right). \tag{3.19}$$

The splitting function $P_{ij}(z)$ is the probability of finding a parton of type i inside a parton of type j with momentum fraction z.

3.3.4 Low x

Results from the HERA [31, 32] experiments show that the proton structure function F_2^{p} rises at low x, which indicates the presence of a large sea-quark contribution (Figure 3.4). In this region, the evolution is expected to be dominated by the gluon distribution, which becomes more significant as x becomes lower. Hence low-x measurements can constrain the gluon distribution, even though in leading order F_2 is not sensitive to gluons. It has not yet been possible to determine whether a similar low-x rise exists in the photon structure function, because of the limited low-x reach of eγ scattering experiments compared to ep scattering experiments.

The DGLAP equations should begin to break down at low x because $\log(1/x)$ terms become important. At asymptotically high Q^2 the DLLA (Double Leading Log Approximation) retains the leading log terms and predicts the low x behaviour. Ignoring the effect of the quark distributions, the gluon distribution is given by [25]

$$g(x,t) \sim \frac{1}{x}\exp\sqrt{\frac{144}{(33-2n_f)}\log\frac{\log t/\Lambda^2}{\log t_0/\Lambda^2}\log\frac{1}{x}}. \tag{3.20}$$

The factorisation scale t is the virtuality of the gluon, and t_0 is the starting point of the evolution.

At lower Q^2, it is necessary to re-sum the leading log terms in $1/x$ to all orders. This is accomplished using the BFKL equation, in which the integration is performed over the full phase space of the gluons. The result

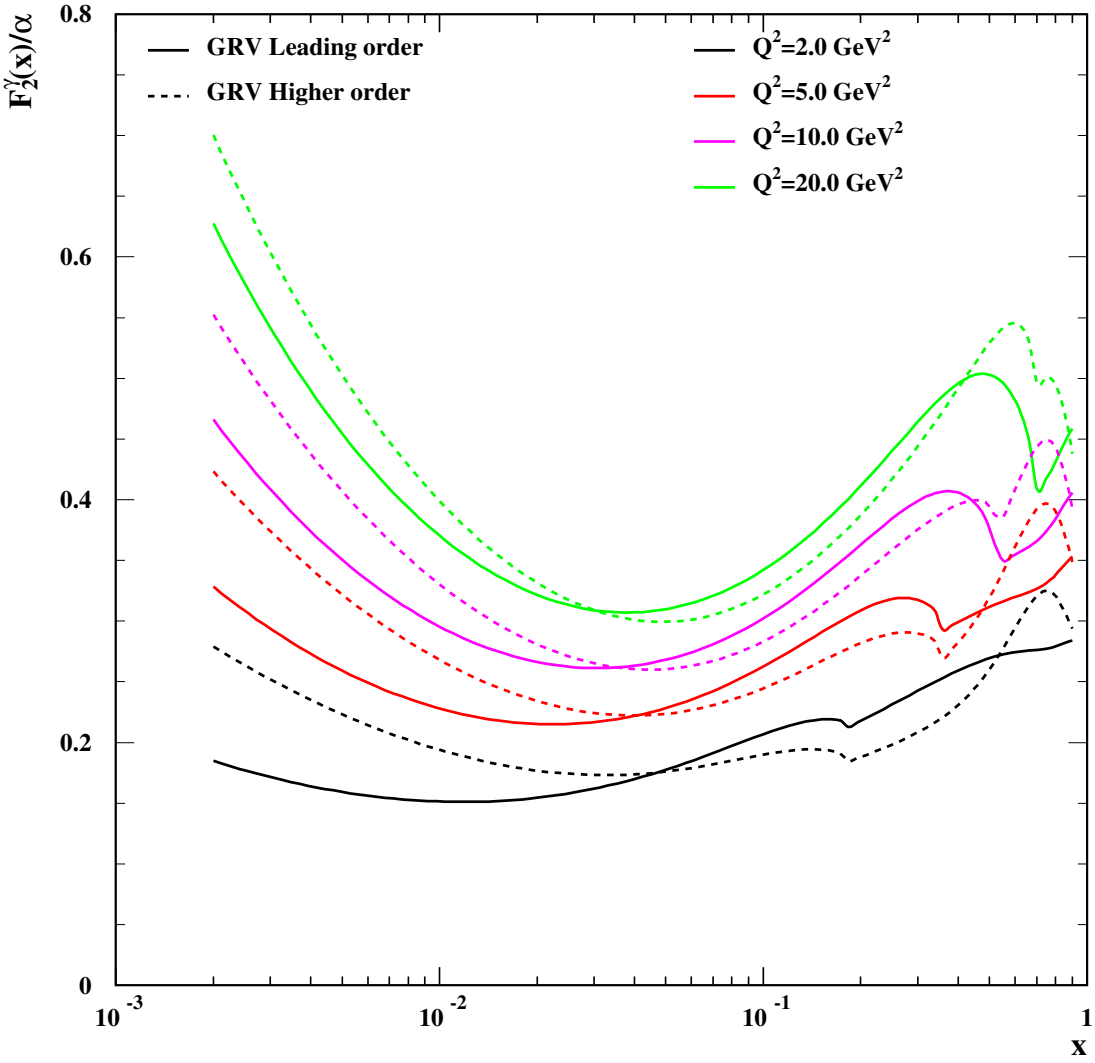

Figure 3.3: The evolution of F_2^γ according to the GRV parameterisation, from Q^2=2.0 GeV^2 to Q^2=20.0 GeV^2. Both the leading order and higher order predictions are shown.

is [25]

$$g(x,t) \sim \frac{1}{x}\int^{Q^2} \mathrm{d}{k_t}^2 h(k_t) x^{-\lambda} \tag{3.21}$$

where $h(k_t) \sim {k_t}^{\frac{1}{2}}$ at large k_t and $\lambda = 12 \log 2 \frac{\alpha_s}{\pi} \sim 0.5$.

There is not yet any evidence that the BFKL approach is required to explain experimental data, even in kinematic regions where it ought to apply.

3.3.5 Heavy flavour contributions

The charm mass is much larger than that of the light quarks, and it is not a good approximation to treat charm as massless over the full kinematic range. The constraint $W^2 > 4{m_q}^2$ means that the charm contribution to F_2^γ will be absent at high x, but the cut-off is not sharp because the phase space for charm production is limited near the threshold. At lower x the charm contribution is large due to the $\frac{2}{3}$ charge. The contribution from b quarks is negligible at LEP energies because of their much higher mass and smaller charge. Calculation of charm evolution requires the massive quark DGLAP equations; however, a combination of direct and resolved QPM contributions is a good approximation and treats the charm threshold correctly [33].

3.3.6 The P^2 dependence of F_2^γ

The discussion in the previous sections has assumed that the target photons are real. In fact the virtuality P^2 is only restricted to be less than a fixed maximum, which is also the minimum Q^2 for the tagged electron. the minimum Q^2 by the anti-tag requirement. The distribution of P^2 can be calculated as a luminosity function (the actual distribution of P^2 in the data is experimentally unknown). It is strongly peaked at the minimum P^2, which in single-tagged two-photon events is zero. It is therefore usual to treat the target photons as real for the purposes of kinematics. This does not necessarily mean that the impact of non-zero P^2 on the structure function is negligible.

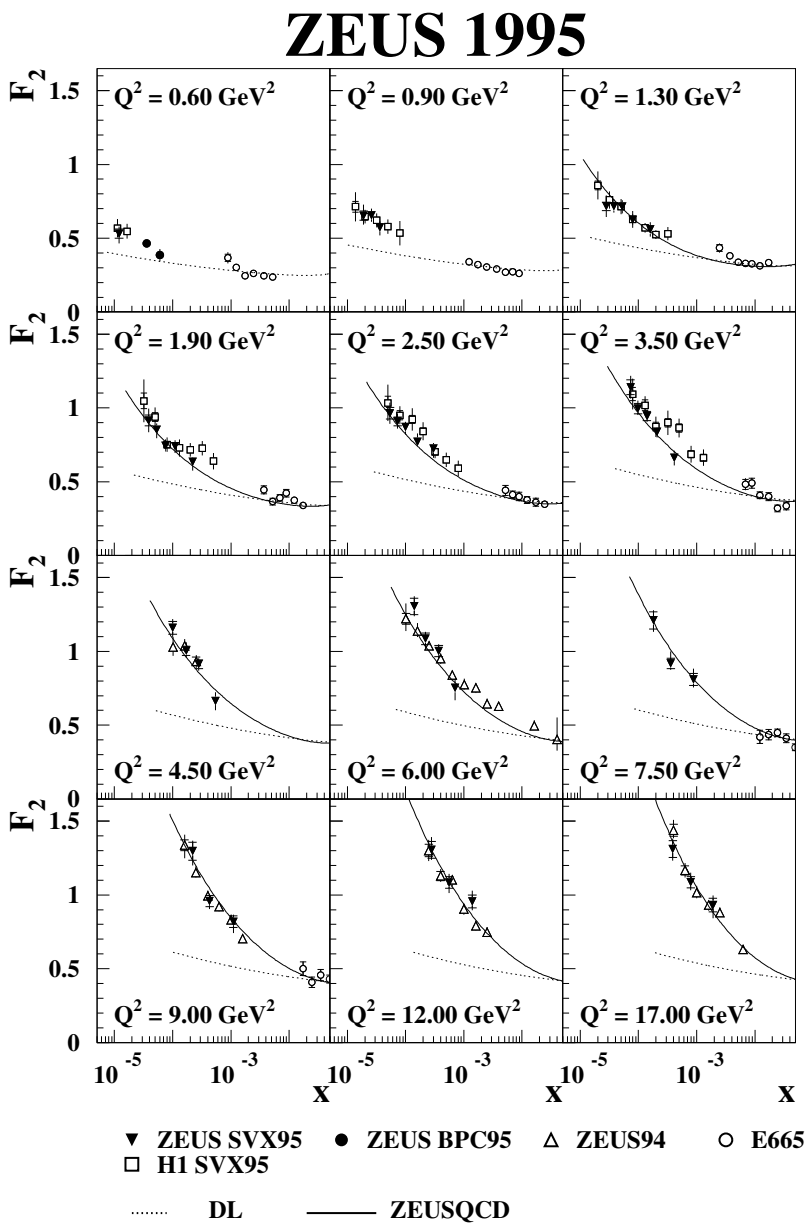

Figure 3.4: Measurements of F_2^p by ZEUS [32].

Virtual photons exhibit a more pointlike behaviour than real photons. The hadronic part of the structure function is therefore suppressed, and this may have consequences at low x, where the hadronic part of F_2^γ dominates.

Predictions for the P^2 dependence of F_2^γ involve interpolation between the hadronic and perturbative regions. Typically, the input distribution is modified according to P^2 before evolving with Q^2. There are problems in finding a suitable VMD input for virtual structure functions, as the only data available is for real mesons, and in extending the model to large $P^2 \simeq Q^2$. There are large variations between the available parameterisations of $F_2^\gamma(\mathrm{x}, Q^2, P^2)$, though they show the same qualitative behaviour.

3.4 Parameterisations of F_2^γ

3.4.1 Field, Kapusta and Poggioli (FKP)

This is an all-order QCD calculation of the perturbative part of the photon structure function [34]. The perturbative and non-perturbative parts are separated by a p_t cut for the quarks at the target vertex. The calculation was performed using iterated Altarelli-Paresi equations.

No fit to data was performed, and an extra contribution is required for the non-perturbative part, such as, for example, the TPC/2γ low Q^2 parameterisation [7] which was used by AMY [35].

Schuler and Sjöstrand [36] argued that there is no consistent way to combine perturbative and non-perturbative parts within the FKP framework, and that the FKP model does not work well at low x and low Q^2.

The FKP parameterisation for $Q^2 = 10.0$ GeV^2 is shown in Figure 3.2.

3.4.2 Levy Abramowicz and Charcula (LAC)

The LAC [37] parameterisations use as an input distribution a general form suggested by the solution of the DGLAP equations:

$$\begin{aligned} xq_0(x) &= Ae_q{}^2 x\frac{x^2+(1-x)^2}{1-B\ln(1-x)} + Cx^D(1-x)E \\ xg_0(x) &= C_g x^{D_g}(1-x)^{E_g}. \end{aligned} \tag{3.22}$$

The first and second terms in the quark distributions correspond to the forms expected for the pointlike and hadronic parts, respectively. There are in total 12 parameters, which were fitted to data in the range Q^2=4–100 GeV^2 (LAC1, LAC2), or Q^2=1–100 GeV^2 (LAC3). The LAC1 and LAC2 parameterisations use different forms for the gluon distribution. Charm is treated in the same way as the light quarks, except that the charm contribution is only included when $W^2 > 4M_c{}^2$, which leads to a discontinuity at high x. The LAC structure functions are illustrated in Figure 3.5

The gluon distribution is not well constrained by the data, leading to unphysical behaviour in some regions. Because of this the LAC approach was criticised by Vogt [38]. Gordon and Storrow [39] argued that the LAC3 structure function gives a good fit to the data at the expense of an unrealistic gluon distribution.

3.4.3 Gordon and Storrow (GS)

According to Gordon and Storrow [39], evolving from a low starting scale is inappropriate because the low Q^2 region is outside the region of applicability of perturbative QCD. Consequently they begin the evolution at Q^2=5.3 GeV^2, using only data above this Q^2 value. The input functions are a combination of VMD and QPM, since with a high starting scale the pointlike contribution is significant. The free parameters are the total momentum fractions carried by sea quarks and by gluons, and the masses of the light quarks used

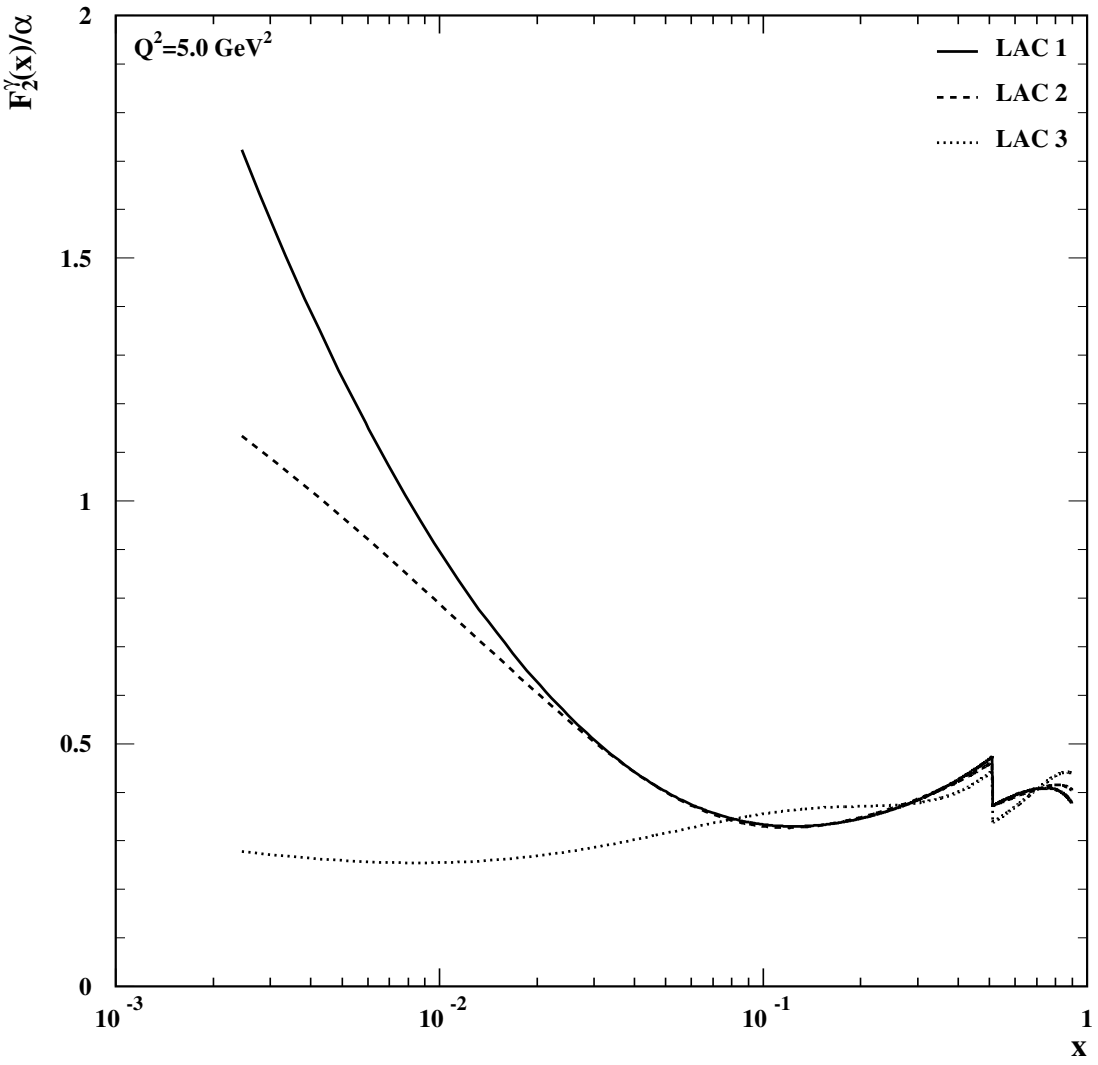

Figure 3.5: The LAC parameterisations of F_2^γ at Q^2=5.0 GeV^2, for 4 flavours. The discontinuity is due to the charm threshold.

in the QPM formula. The gluon momentum fraction is constrained (though within a fairly wide range) to avoid the unphysical behaviour seen in the LAC structure functions. Charm is treated similarly to the light quarks, but has a fixed mass of 1.5 GeV.

This was the first parameterisation of F_2^γ to include a next-to-leading order calculation. The NLO input distributions at the starting scale of Q^2=5.3 were the same as the LO input.

3.4.4 Glück, Reya and Vogt (GRV)

The GRV [40] parameterisation is evolved from a low starting scale using a VMD input based on measurements of the pion structure function, with the form

$$xf_\pi \sim x^a(1-x)^b \tag{3.23}$$

where a and b are determined by experiment [28]. The only free parameter is the normalisation of the VMD input, which corresponds to uncertainty in the inclusion of the ω and ϕ mesons. A least squares fit was performed to data in the range Q^2=0.7–100 GeV^2. Leading order and higher order structure functions were produced. The massive quark QPM model (Bethe-Heitler [41]) was used for the charm contribution.

The GRV approach requires the assumption that perturbative QCD is valid at a low enough starting scale to take a purely VMD based input. The evolution starts from 0.25 GeV^2 (LO) and 0.3 GeV^2 (HO), where there is no data to check the validity of this assumption. Nevertheless, the GRV structure functions fit all available data well.

These authors have also produced parton distribution functions for the pion and proton that describe the available data in the low-x region, successfully predicting a low-x rise. It has not yet been possible to test the photon structure function in the same region.

3.4.5 Glück, Reya and Stratmann (GRS)

The GRS parameterisation [42] is a development of the GRV model which allows for virtual target photons, i.e. $P^2 > 0$. Unlike the GRV parameterisation, the input distribution at the starting scale is not purely VMD, but an interpolation between VMD and a perturbative, pointlike contribution which dominates for large P^2. As with GRV, the input VMD distribution is taken from measurements of the pion structure function. However, the structure function of *virtual* pions is unknown. Therefore the VMD input is fixed for all P^2 up to the starting scale of the evolution.

The GRS parameterisation is valid for $P^2 \ll Q^2$, with a smooth transition to $P^2 = 0$. The virtual structure function is suppressed compared to the real one, with the largest difference at low x. The theoretical uncertainties are largest at low P^2 due to the large non-perturbative contribution. At $P^2 \simeq Q^2$ the DIS picture is no longer valid.

3.4.6 Hagiwara *et al.* (WHIT)

The WHIT [33] parameterisations are essentially a study of the effect of the gluon content of the photon on the structure functions. Measurements of F_2^γ are not directly sensitive to the gluon distribution, but the DGLAP equations predict that it will it will affect the Q^2 evolution of F_2^γ.

The initial distribution is a fit to

$$\begin{aligned} \frac{xq(x)}{\alpha} &= Ax^B(1-x)^C, \\ \frac{xg(x)}{\alpha} &= A_g x^B(1-x)^{C_g}, \end{aligned} \tag{3.24}$$

using data with $Q^2 > 4$ GeV^2. Some low x data points were omitted from the fit because of the possibility of large systematic uncertainties. The gluon parameters A_g and C_g were not fitted to the data but were varied systematically, leading to six different parton distribution functions with different

gluon content. The charm contribution was taken to be the sum of the QPM direct and resolved processes. The evolution was performed in leading order only, as the variations in the gluon content are so large that there would be little advantage in using the higher order equations.

3.4.7 Schuler and Sjöstrand (SaS)

In their parameterisation [36], Schuler and Sjöstrand divide the photon structure function into three parts:

$$f^{\gamma}(x,Q^2) = f^{\gamma,\mathrm{dir}}(x,Q^2) + f^{\gamma,\mathrm{VMD}}(x,Q^2,{Q_0}^2) + f^{\gamma,\mathrm{anom}}(x,Q^2,{Q_0}^2). \quad (3.25)$$

They argue that the hadronic part can be separated by a scale ${Q_0}^2$ into perturbative (anomalous) and non-perturbative parts, the latter modelled using vector-meson states. The different parts of F_2^{γ} are also expected to have different properties in the hadronic final state.

Unlike the case for the GRV parameterisation, the VMD input functions are not taken from the pion structure function, but are found by fitting to data. However, the normalisation is constrained because the higher mass vector meson states (above ρ, ω and ϕ) are included in the definition of the anomalous part. In the GRV approach, the separation between low and high mass vector meson states is not made explicit. The evolution is performed in leading order only, and the Bethe-Heitler cross section is used for the charm contribution. There are four sets of SaS structure functions, corresponding to two different starting scales for the Q^2 evolution and two factorisation schemes: SaS1D (DIS_{γ}, Q_0=0.6 GeV^2), SaS2D (DIS_{γ}, Q_0=2.0 GeV^2), SaS1M ($\overline{\mathrm{MS}}$, Q_0=0.6 GeV^2) and SaS2M ($\overline{\mathrm{MS}}$, Q_0=2.0 GeV^2). The SaS structure functions also contain a prediction for the P^2 dependence. This is modelled in a similar way to the GRS approach, though fitted within the SaS framework. The SaS and GRV structure functions are compared in Figure 3.6.

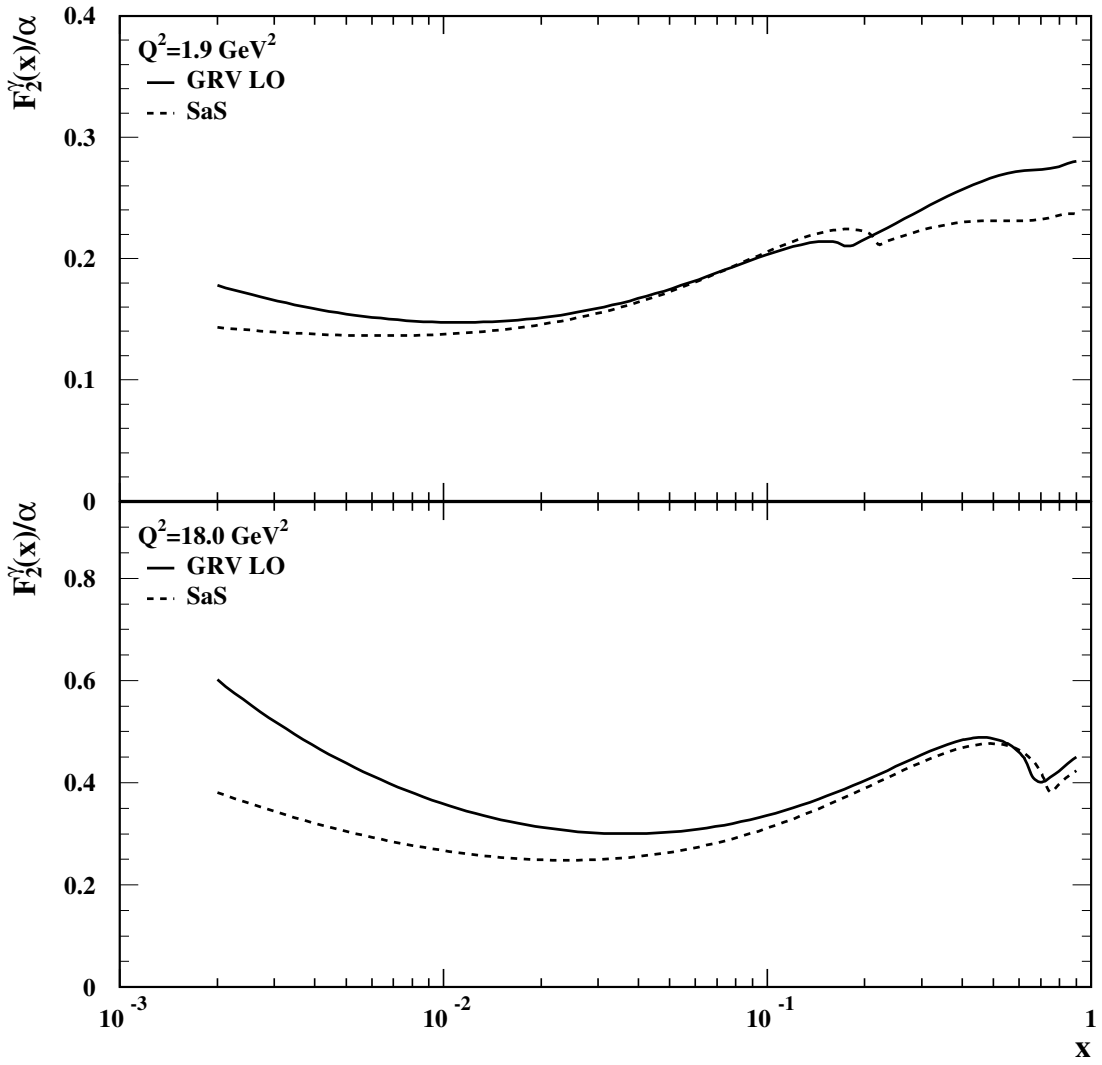

Figure 3.6: Comparison of the GRV LO and SaS1D parameterisations of F_2^γ.

Chapter 4

Monte Carlo models

The main use for Monte Carlo in this analysis is for correcting detector effects. With a perfect detector, F_2^γ could be determined simply by measuring x and Q^2 from the hadronic activity and the tagged electron, and counting events. However, much of the hadronic energy of $\gamma\gamma$ events is deposited in the non-tracking region of OPAL and is not well measured, so some way of estimating the missing energy is needed. This is done using Monte Carlo events (the actual technique used is called unfolding and is discussed later). For accurate correction of missing energy, the Monte Carlo program must provide a good model of the data, particularly of the distribution of the hadrons in the final state. Unfortunately even the best models are only an approximation, so it is necessary to make the best use of the available information from the detector.

Another use for Monte Carlo programs is in providing a description of the physics background, so that it can be subtracted from the data distributions. Modelling error is not such a problem here because the percentage of background is small, and generally, background processes are accurately modelled, or at least accurately described. Events with leptonic final states can be generated using exact matrix elements, while hadronic Monte Carlo

generators can be tuned to fit the data.

For F_2^γ measurements it is not enough to have a Monte Carlo model that gives a good description of the data, because the form of the final state depends on the input F_2^γ as well as the final state model. What is needed are models that give the best possible description of the underlying physics, possibly tuned to other processes, but not to $\gamma\gamma$ data.

Since $\gamma\gamma$ interactions involve non-perturbative QCD and many-particle final states, they cannot be modelled exactly. Instead, Monte Carlo programs split the problem into several stages that are dealt with separately using various approximations. The stages are usually

- emission of photons from one or both of the beam electrons,
- the hard sub-process,
- parton showers, and
- hadronisation of the final state partons.

Different Monte Carlo programs emphasise different aspects of the problem. In HERWIG (Hadron Emission Reactions With Interfering Gluons) [43], the focus is on providing an accurate description of the parton showers, while simulating a wide variety of hard processes. PHOJET [44] concentrates on collisions of photons and hadrons, particularly in the consistent treatment of soft and hard interactions. The advantage of F2GEN [45] is simplicity (it is purely a $\gamma\gamma$ generator) combined with the ability to select different final state models, represented by the angular distribution of the outgoing quarks. In this analysis, F2GEN is used only in pointlike mode, which means that the distribution of the outgoing quarks is the same as would be expected for a pair of leptons.

4.1 The luminosity function

The cross-section for $\gamma\gamma$ interactions in e^+e^- events can be factorised into two parts, one describing the production of a two-photon state and another describing the interaction of the two photons:

$$d\sigma_{e^+e^-\to e^+e^-X} = L^{TT}_{\gamma\gamma}\sigma^{TT}_{\gamma\gamma\to X}. \tag{4.1}$$

Only the transverse part of the cross-section is included here, because the longitudinal part is small when the virtuality of the target photon is small.

For nearly-real photons, the luminosity function factorises into two parts, one for each photon. This is the Equivalent Photon Approximation (EPA), in which the photon flux is determined from the splitting function

$$f_{\gamma/e}(z,P^2) = \frac{\alpha}{2\pi}\left(\frac{1+(1-z)^2}{zP^2} - \frac{2{m_e}^2 z}{P^4}\right). \tag{4.2}$$

HERWIG neglects the ${m_e}^2/P^4$ term, and in the DIS model, the EPA is only used for the target photon, not the probe photon. PHOJET and F2GEN use the full EPA for both photons.

In the structure functions, it is assumed that $P^2 = 0$. Although some parameterisations of F_2^γ include a prediction for the P^2 dependence, these predictions vary widely and were not used when generating events for this analysis.

4.2 The hard sub-process

Monte Carlo events are characterised by a single hard scattering, to which corrections are applied in the form of initial and final state radiation. The hard scattering is calculated using matrix elements.

A variety of hard processes are used in generating $\gamma\gamma$ events. The main examples are

- DIS, eq $\rightarrow$ eq,
- Direct, $\gamma\gamma \rightarrow$ qq,
- Photon-gluon fusion, g$\gamma \rightarrow$ qq, and
- Gluon Compton scattering, q$\gamma \rightarrow$ qg.

These processes are illustrated in Figure 4.1. HERWIG uses the DIS process, with the momentum fraction of the scattered quark taken from a parton distribution function selected by the user. F2GEN simulates only the direct process, with the cross-section given by the selected structure function. F2GEN has a limited ability to simulate other processes by changing the angular distribution of the outgoing quarks. PHOJET simulates the direct process along with the two resolved processes, using its own internal cross-sections. This means that PHOJET cannot generate events according to a user-defined structure function, though a similar effect can be achieved by reweighting the events.

4.3 Soft and multiple interactions

At low W, the cross-section for $\gamma\gamma$ scattering is dominated by processes for which there is no hard scale, such as diffraction or Regge scattering. Soft and hard processes are usually separated by a p_t cut. PHOJET contains a detailed model of soft processes, including soft reggion and pomeron exchange. Soft and hard interactions are unitarised together, allowing for multiple soft and hard interactions in the same event. As soft interactions are not perturbatively calculable, they are tuned to data, but the same model should be applicable to various types of events: hadron-hadron, photon-hadron or photon-photon. This gives the model some predictive power. HERWIG allows optionally the generation of a Soft Underlying Event (SUE), which is

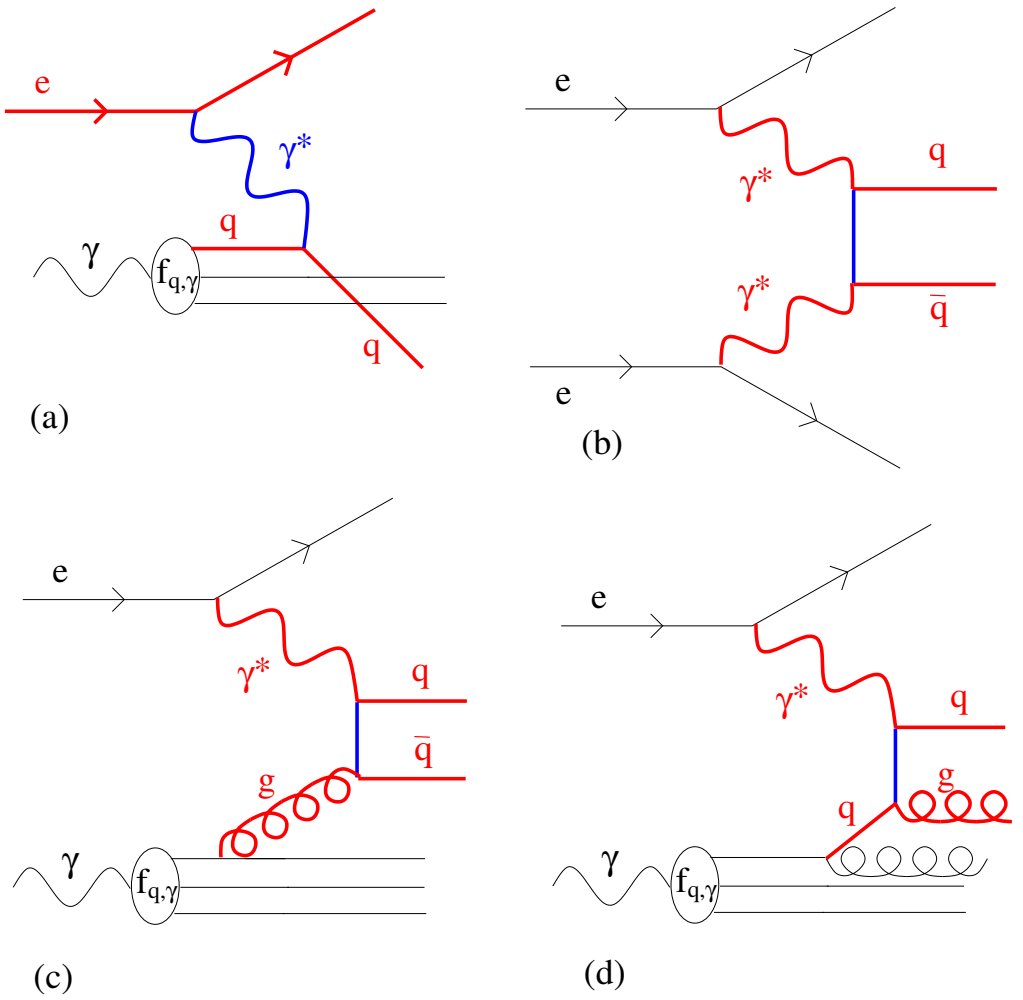

Figure 4.1: Hard processes simulated by Monte Carlo programs. Particles taking part in the hard interaction are drawn with bold lines: (a) deep inelastic scattering, (b) direct $\gamma\gamma$ interaction, (c) photon-gluon fusion and (d) gluon Compton scattering.

the interaction of the photon remnant with its nearest neighbour from the hard event. This increases the transverse energy of the event. The SUE is turned off by default, because of poor agreement with HERA data. The events used in this analysis were generated without the SUE option.

F2GEN does not model soft processes.

4.4 Parton showers

The partons involved in the hard scattering may emit radiation before or after the scattering. For example, a quark may emit a gluon, or a gluon may become a quark pair. The probabilities of such branchings are given by the DGLAP splitting functions. Initial state radiation is calculated backwards, away from the hard scattering, and final state radiation is calculated forwards. Partons emitted as part of a shower can undergo further splitting, which is always at a lower virtuality than previous emissions, to account for interference effects. The emission continues until a cut-off is reached.

HERWIG has routines for both initial and final state radiation. The parton entering the hard scattering may be evolved back to the target photon, in which case the event is classified as anomalous, or the cut-off may be reached first, in which case the event is classified as hadronic. The distinction has consequences for the treatment of the photon remnant.

PHOJET and F2GEN use JETSET [46] for final state radiation. F2GEN has no initial state radiation, while PHOJET incorporates its own model, similar to the one in HERWIG.

The parton shower model is accurate in the limits of soft and collinear radiation. In order to provide a more accurate treatment of hard radiation, HERWIG includes NLO matrix elements, which are matched in phase space to the rest of the parton shower to avoid double counting.

4.5 Hadronisation

All partons produced by initial and final state showering, as well as the photon remnant, enter the hadronisation or fragmentation stage, in which partons are converted to hadrons. Hadronisation is a complex problem which is not understood from first principles. However, several phenomenological models exist which describe most features of the data. The most commonly used models are cluster fragmentation [47] which is used in HERWIG, and string fragmentation [48], used in JETSET.

In the cluster model, partons form colour-singlet clusters which decay isotropically in their centre-of-mass frame to pairs of hadrons. The hadrons are selected at random from a table of posible decays. A few clusters may be too heavy for two-body decay to be reasonable; these are split to form lighter clusters. Clusters that are too light to decay to a pair of hadrons decay to a single hadron, exchanging 4-momentum with a neighbouring cluster to maintain energy and momentum conservation.

In the string model, pairs of quarks originating from parton showers or directly from the hard interaction are connected by colour strings. Gluons in the final state appear as kinks in the strings. As the quarks move apart, they give energy to the string, which has energy per unit length consistent with hadron spectroscopy data. Eventually the string fragments into pairs of quarks, which combine to form hadrons.

4.6 Radiative corrections

The Monte Carlo programs discussed in this chapter do not include radiative corrections to the DIS process (see Figure 4.2). These were evaluated using the RADEG program [49]. They are dominated by initial state radiation from the deeply inelastically scattered electron. Final state radiation is experimentally integrated out due to the finite granularity of the detector. The

Compton scattering process in which the probe photon is emitted at a low angle but the electron is tagged due to final state radiation at a large angle, contributes very little, and corrections due to radiation from the electron that produces the target photon have been shown to be small [50].

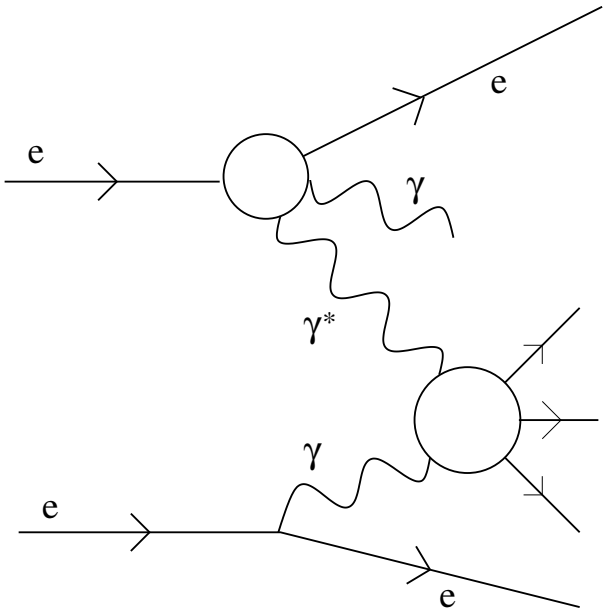

Figure 4.2: Radiative corrections to two-photon DIS.

RADEG performs the calculation using mixed variables, which means that W is calculated from hadronic variables, while Q^2 is calculated from electron variables. This means that x is calculated from both electron and hadronic variables, without using the energy of the target photon - as in the experimental analysis. Without the additional radiation, both sets of variables would be identical.

Radiative corrections to the Monte Carlo cross-section are calculated in bins of x and Q^2, applying the experimental restrictions on $E_{\rm tag}$, $\theta_{\rm tag}$, W and the anti-tag angle. They are largest at low values of x, and will be used later

to correct the measurement of F_2^γ when using Monte Carlo samples without radiative corrections.

4.7 Tuning HERWIG

Accurate measurement of F_2^γ requires a Monte Carlo program with a good description of the hadronic final state. However, there are discrepancies between existing models and the data. For example, HERWIG 5.9 shows a less pointlike behaviour than the data in variables such as the transverse energy out of the tag plane,

$$E_{\mathrm{T}}^{\mathrm{out}} = \sum_i E_{i,\mathrm{t}} |\sin \phi_{i,\mathrm{tag}}| \tag{4.3}$$

where i runs over all particles in the hadronic final state, with transverse energy $E_{i,\mathrm{t}}$, and azimuthal angle $\phi_{i,\mathrm{tag}}$ measured from the tag. The differences also appear in the energy flow (the average hadronic energy per event deposited in the detector as a function of rapidity).

HERWIG 5.9+k_{t}(dyn) is a modified version of HERWIG which gives an increased amount of transverse energy to the events. This is achieved by modifying the distribution of the transverse momentum of the struck parton in the target photon [51]. The default in HERWIG is an exponential distribution; HERWIG 5.9+k_{t}(dyn) uses a power law, which was originally tuned for photoproduction events at HERA [52]. The result is a small but noticeable improvement in the agreement with the data distributions (Figure 4.3), and a shifting of energy flow towards the central region of the detector (Figure 4.4). The 'dyn' label refers to the fact that the cut-off for the exponential distribution is a function of Q^2, and hence dynamic. In an earlier version, a fixed cut-off was used. HERWIG 5.9+k_{t}(dyn) still falls short of the data at high $E_{\mathrm{T}}^{\mathrm{out}}$. Further tuning would be possible, but has not been performed because tuning directly to $\gamma^\star\gamma$ data might lead to biased measurements of F_2^γ.

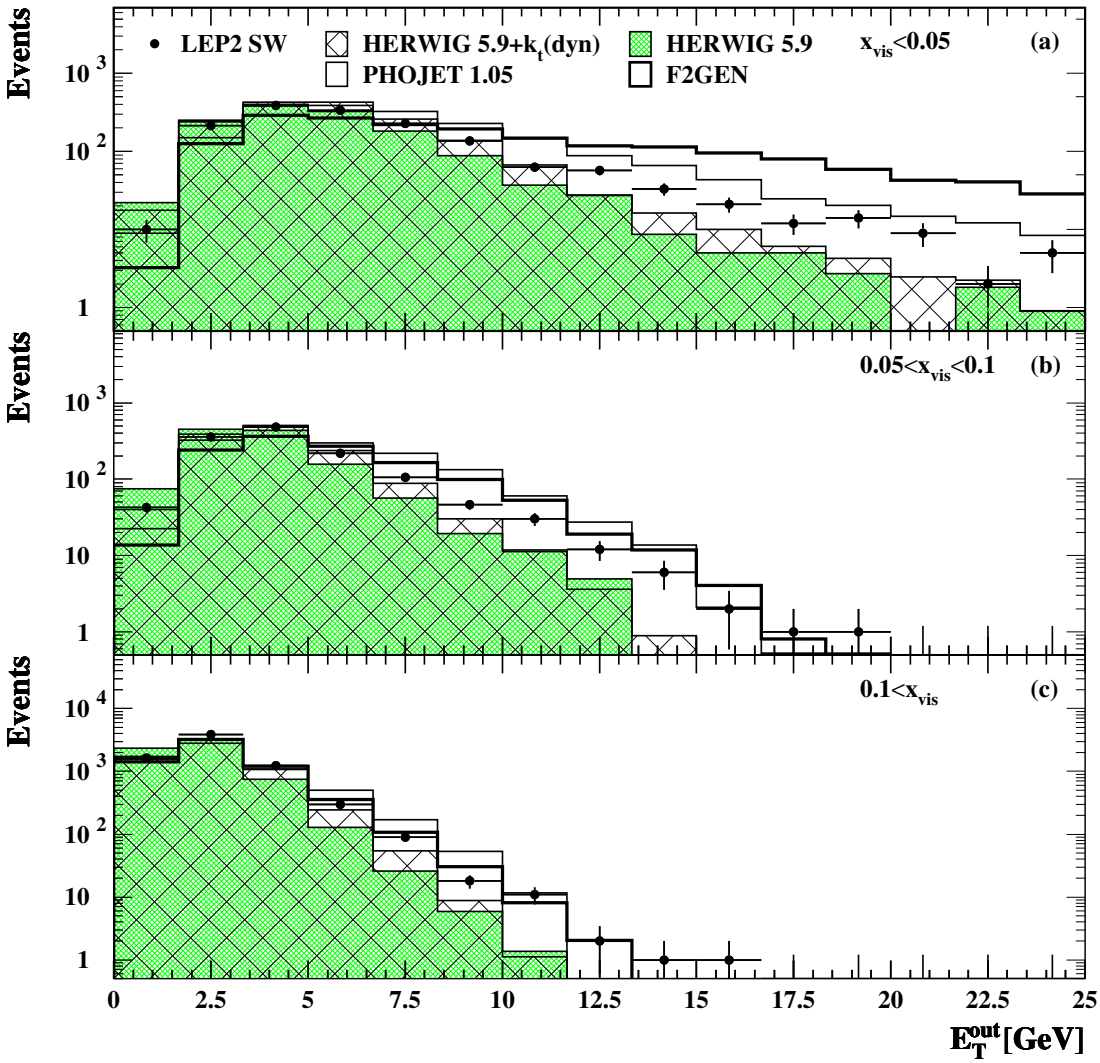

Figure 4.3: Comparison of the transverse energy out of the tag plane, $E_{\mathrm{T}}^{\mathrm{out}}$, for data and Monte Carlo. The sample is divided into three bins of x_{vis}.

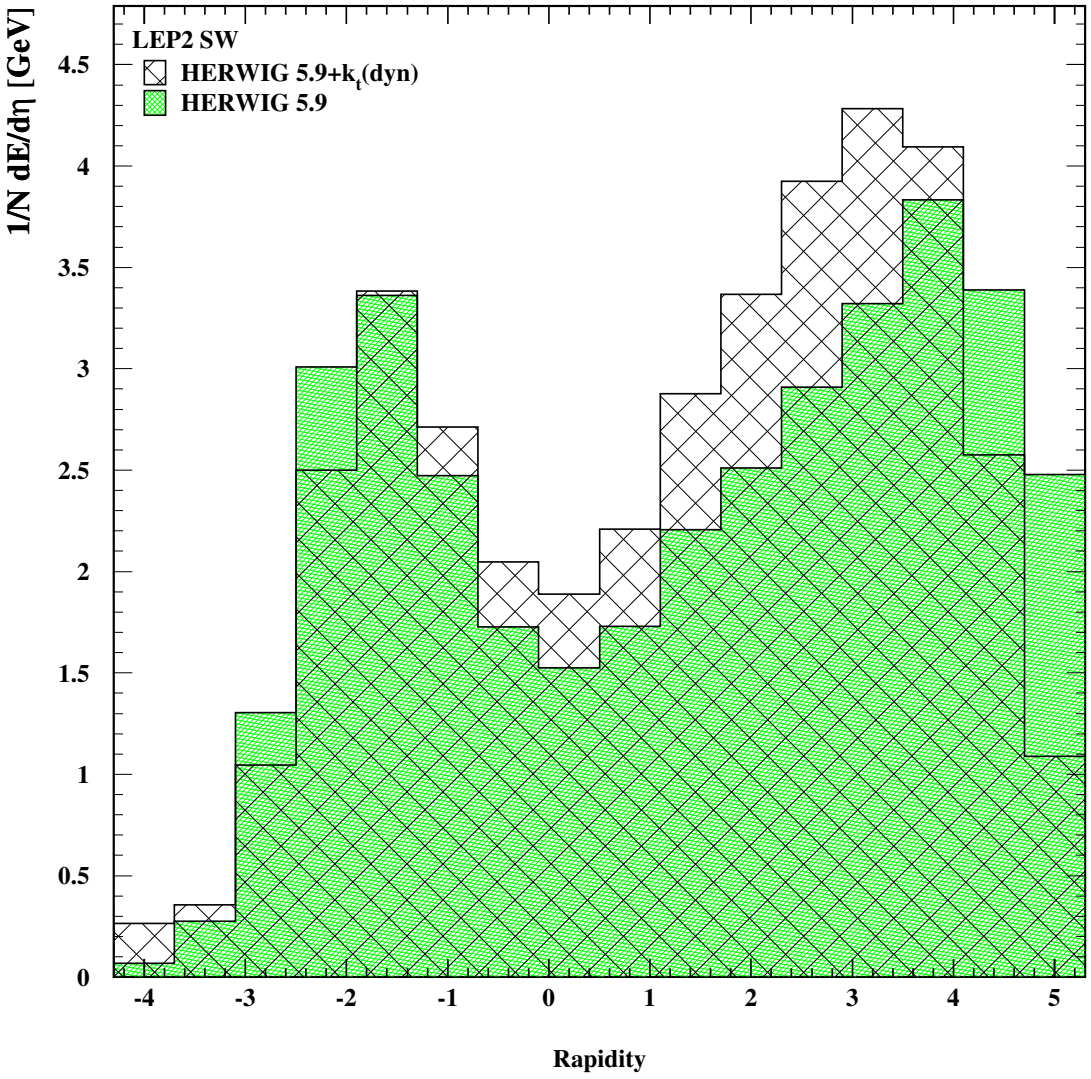

Figure 4.4: Comparison of hadronic energy flow per event as a function of pseudorapidity, $\eta = -\log(\tan(\theta/2))$, where θ is measured with respect to the beam axis on the tag side. The distributions for HERWIG 5.9 and HERWIG 5.9+k_t(dyn) are shown, at generator level, at centre-of-mass energy 189 GeV.

Chapter 5

Event Selection

5.1 The event samples

The largest data samples taken by OPAL prior to this analysis were at the energies 91 GeV, 184 GeV and 189 GeV. There are two tagging subdetectors, FD and SW. The beam energy and range of tagging angles in each sample determines the range of Q^2 in which F_2^γ can be measured (Equation 3.2). A lower tag angle also means that the minimum accessible value of x is lower. In order to measure F_2^γ to the lowest possible values of x, the SW detector is used for tagging at all beam energies. It happens that the range of Q^2 for the data with electron tags in FD at LEP1 is approximately the same as for the data with electrons tagged in SW at LEP2. This gives a useful cross-check of the result.

Three samples of events are used, classified by the beam energy and the tagging subdetector. They are referred to as the LEP1 SW, LEP1 FD and LEP2 SW samples. The 183 GeV and 189 GeV data cover a similar region of x and Q^2 and are both included in the LEP2 SW sample.

5.2 Event reconstruction

The program ROPE (Reconstruction of OPal Events) is used to transform raw data from OPAL into a list of tracks and clusters that can be used for analysis. It also provides the basic framework for physics analysis. ROPE can be run on real or simulated data, ensuring that the same code is used for data and Monte Carlo events.

The first step in a $\gamma^*\gamma$ analysis is to flag candidate events, so that they can be accessed with greater efficiency later. This is performed by the subroutine RTWOPH in ROPE. It has very loose requirements and many events selected by RTWOPH are rejected in later stages of the analysis. RTWOPH requires two good tracks and an energy deposit of 35% of the beam energy in FD, SW or EE. The conditions for a good track are that

- there are at least 20 hits in CJ,
- the minimum distance in r–ϕ from the interaction point, $d_0 < 2.5$ cm,
- the minimum distance in z from the interaction point, $z_0 < 50$ cm,
- the radius of first measured point in CJ is less than 75 cm, and
- the transverse momentum $p_t > 0.1$ GeV.

5.2.1 Detector status

For every run, each subdetector is given a status code indicating how well it is working. These codes are described in Table 5.1. For those subdetectors that are vital for the analysis, a status code of 3 is required. These are the tracking detectors CV and CJ, the electromagnetic calorimeters EB and EE, and the tagging subdetectors FD and SW.

Status code	Description
0	dead or off
1	unreliable
2	minor problems
3	fully functional

Table 5.1: Description of the subdetector status codes.

5.2.2 Track quality requirements

In order for a track to be accepted for use in the analysis, it has to satisfy certain quality requirements. These are designed to reject tracks originating from, for example, particles backscattered in the solenoid, beam gas interactions or cosmic rays. The requirements (stricter than those in RTWOPH) are that

- there are at least 20 hits in CJ,
- the number of hits in CJ is at least half the number of expected hits for the track,
- the minimum distance in r–ϕ from the interaction point, $d_0 < 2.5$ cm,
- the minimum distance in z from the interaction point, $z_0 < 30$ cm,
- the transverse momentum $p_t > 0.12$ GeV, and
- the angle θ of the track satisfies $|\cos\theta| < 0.9622$.

5.2.3 Cluster quality requirements

To remove clusters due to noise from the analysis, there are also quality requirements for clusters. First, all clusters are compared to a list of known

'hot' clusters, and the cluster is rejected if its energy is below the threshold for the expected noise. There are further requirements depending on the subdetector, which are listed in Table 5.2.

subdetector	$E_{\min}$ (GeV)	other conditions
EE	0.25	at least 2 adjacent lead-glass blocks
EB	0.1	at least 1 lead-glass block
HB	0.6	at least 1 tower
HE	0.6	at least 1 tower
HP	0	at least 1 tower
FD	1.0	at least 20% in the main calorimeter
SW	2.0	-

Table 5.2: Quality requirements for calorimeter clusters.

5.2.4 Track–cluster matching

Particles leaving tracks in the central tracking region will usually also leave clusters in the electromagnetic or hadronic calorimeters. In order to avoid double-counting it is necessary to match clusters and tracks in the same θ–ϕ region. This is done by the MT package [53].

MT takes the list of accepted tracks and clusters, and outputs a list of 4-vectors. In the matching process, there are three possibilities for a track and cluster. The first is that they do not match in θ and ϕ, in which case both the track and cluster are used. The second is that they match, and the energy of the cluster is less than that expected for the track plus a certain tolerance. In this case the cluster is discarded and only the track is used, because the energy resolution of the tracking system is usually better than that of the calorimeters. The third possibility is that the track and cluster match, but the cluster energy is too large for it to be accounted for by the

track alone. In this case the energy of the cluster is reduced by the amount expected from the track, and both the track and the reduced-energy cluster are used.

Clusters from the forward region (FD and SW) are not matched to tracks, as the tracking system does not extend to such low angles.

5.3 Final selection cuts

To select the events to be used in the final analysis, cuts are made on the tagged electron and on the hadronic final state. The aim of these cuts is to reduce background while retaining a high efficiency for $\gamma^{\star}\gamma$ events. The variables on which cuts are applied are

- the energy of the tagged electron, E_{tag},
- the angle of the tagged electron, θ_{tag},
- the energy of the most energetic cluster on the opposite side of the detector to the tag (the anti-tag), E_{a},
- the number of charged tracks, N_{ch},
- the number of tracks identified as electrons from their $\mathrm{d}E/\mathrm{d}x$ weight, N_{e} and
- the invariant mass of the hadronic final state, W_{vis}.

The cuts applied to each of the data samples are listed in Table 5.3. The reasons for these cuts are explained in the following section, which discusses background.

cut	LEP1 SW	LEP1 FD	LEP2 SW
$E_{\rm tag}/E_{\rm b}$ min	0.75		0.775
$\theta_{\rm tag}$ min [mrad]	27	60	33.25
$\theta_{\rm tag}$ max [mrad]	55	120	55
$E_{\rm a}/E_{\rm b}$ max	0.25		
$N_{\rm ch}$ min	3 (2 non-electron tracks)		
$W_{\rm vis}$ min [GeV]	2.5		
$W_{\rm vis}$ max [GeV]	40		60

Table 5.3: The selection cuts applied to each data sample.

5.4 Background

There are many processes that could potentially produce a background to $\gamma^\star\gamma$ events. It is important to know which of these are significant and to exclude them as far as possible from the data sample when measuring F_2^γ. The main tool used for for understanding background is Monte Carlo simulation. Standard OPAL Monte Carlos samples were used to estimate the contributions from the processes described in this section. The details of the Monte Carlo samples and the number of events passing the final cuts are listed in Tables 5.4 and 5.5.

5.4.1 Hadron production from e^+e^- annihilation

At LEP1 there are many more hadronic Z^0 decay events than $\gamma^\star\gamma$ events, so they could form a significant background. They are likely to pass the minimum $N_{\rm ch}$ and minimum $W_{\rm vis}$ cuts, but usually do not have a high-energy, low-angle particle to act as a tag. Therefore, the tag requirements reduce this background considerably. The remaining hadronic events tend to have higher $W_{\rm vis}$ than $\gamma^\star\gamma$ events, so a maximum $W_{\rm vis}$ cut is applied. This cut is higher at LEP2 because the cross-section for hadronic events is lower than at

process	generator	luminosity [pb^{-1}]	selected	
			LEP1 SW	LEP1 FD
$Z^0 \rightarrow$ hadrons	JETSET 7.4 [46]	133.3	28±4	126±10
$Z^0 \rightarrow \tau^+\tau^-$	KORALZ 4.0 [54]	405.0	2±1	2±1
$\gamma^\star\gamma \rightarrow e^+e^-$	VERMASEREN 1.01 [55]	391.0	11±1	9±2
$\gamma^\star\gamma \rightarrow \mu^+\mu^-$	VERMASEREN 1.01	456.0	1±1	2±1
$\gamma^\star\gamma \rightarrow \tau^+\tau^-$	VERMASEREN 1.01	201.0	200±9	156±9
$e^+e^- \rightarrow e^+e^-e^+e^-$	GRC4F 2.1 [56]	500	0	0
$e^+e^- \rightarrow e^+e^-\mu^+\mu^-$	FERMISV [57]	1000	0	0
$e^+e^- \rightarrow e^+e^-\tau^+\tau^-$	FERMISV	1000	0	0
$e^+e^- \rightarrow e^+e^-q\overline{q}$	FERMISV	1000	0	0
$e^+e^- \rightarrow l^+l^-l^+l^-$	FERMISV	1000	0	0
$e^+e^- \rightarrow l^+l^-q\overline{q}$	FERMISV	1000	0	0
$\gamma\gamma \rightarrow$ hadrons	PHOJET 1.05c [44]	209.2	4±1	1±1
$\gamma^\star\gamma^\star \rightarrow$ hadrons	PHOJET 1.1 [44]	150.0	51±5	72±7

Table 5.4: Summary of the background Monte Carlo samples for LEP1. The numbers of selected events have been normalised to the luminosity of the data sample. The errors are statistical only.

process	generator	luminosity [pb^{-1}]	selected (LEP2 SW)
$Z^0 \rightarrow$ hadrons	PYTHIA 5.722 [58]	5000	23±1
$Z^0 \rightarrow \tau^+\tau^-$	KORALZ 4.02 [54]	10000	2±1
$e^+e^- \rightarrow W^+W^-$	PYTHIA 5.722 [58]	6191	0
$\gamma^\star\gamma \rightarrow e^+e^-$	VERMASEREN [55]	994	9±1
$\gamma^\star\gamma \rightarrow \mu^+\mu^-$	VERMASEREN	337	6±2
$\gamma^\star\gamma \rightarrow \tau^+\tau^-$	VERMASEREN	982	357±9
$e^+e^- \rightarrow e^+e^-e^+e^-$	GRC4F 2.1 [56]	5000	0
$e^+e^- \rightarrow e^+e^-\mu^+\mu^-$	GRC4F 2.1	5000	0
$e^+e^- \rightarrow e^+e^-\tau^+\tau^-$	GRC4F 2.1	5000	0
$e^+e^- \rightarrow e^+e^-q\overline{q}$	GRC4F 2.1	5000	9±1
$e^+e^- \rightarrow l^+l^-l^+l^-$	GRC4F 2.1	5000	0
$e^+e^- \rightarrow l^+l^-q\overline{q}$	GRC4F 2.1	5000	0
$e^+e^- \rightarrow q\overline{q}q\overline{q}$	GRC4F 2.1	5000	0
radiative Bhabha	TEEGG [59]	993	5±1
$\gamma\gamma \rightarrow$ hadrons	PHOJET 1.10 [44]	94.7	0
$\gamma^\star\gamma^\star \rightarrow$ hadrons	PHOJET 1.10	2259.0	71±3

Table 5.5: Summary of the background Monte Carlo samples for LEP2. The numbers of selected events have been normalised to the luminosity of the data sample. The errors are statistical only.

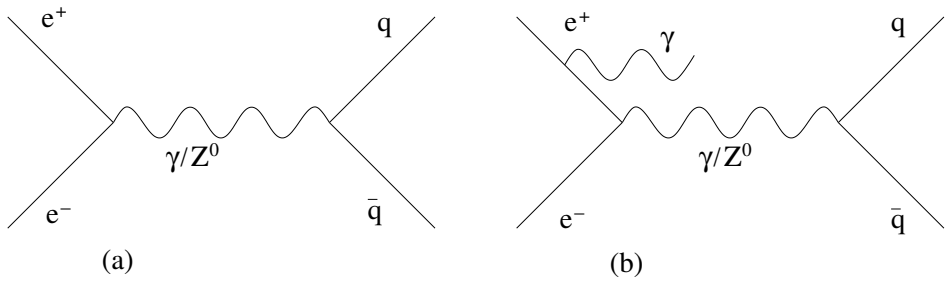

Figure 5.1: Hadron production from Z^0 decay: (a) non-radiative, (b) radiative return.

LEP1, and also because $W_{\rm vis}$ for $\gamma^\star\gamma$ events at LEP2 is higher than at LEP1, due to the higher beam energy. At LEP2 the radiative photon can provide a tag.

5.4.2 Tau pair production from Z^0 decay

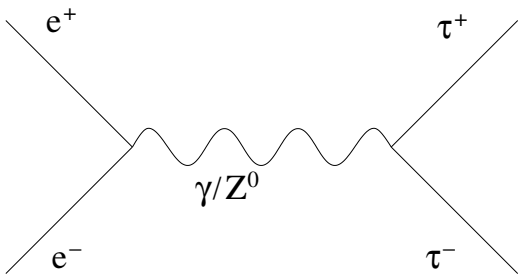

Figure 5.2: Tau pair production from Z^0 decay.

These events have similar characteristics to the hadronic Z^0 decays except that the total visible energy may be lower due to the neutrinos from tau decay, so the $W_{\rm vis}$ cut is not so effective in removing these events. However, the cross-section is much lower than that of hadronic Z^0 decay.

5.4.3 Lepton pair production in two-photon events

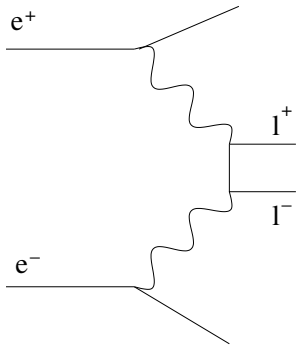

Figure 5.3: Lepton pair production in two-photon events.

These events are similar to hadronic $\gamma^*\gamma$ events, but leptons are produced in the two-photon collision instead of quarks. These events produce tagged electrons and so must be rejected by requirements on the hadronic final state. Having only two leptons in the final state, the electron-pair and muon-pair events usually fail the minimum $N_{\rm ch}$ cut. However, it is possible for a single particle to produce more than one track in the reconstructed event, for example by bremsstrahlung or bad reconstruction of a track, so some events survive the cut. This is much more likely to happen for electrons than for muons. An additional cut is made on the number of identified electrons, which further reduces the electron-pair background. Very little can be done to reduce the two-photon tau-pair background, but it is well modelled in Monte Carlo and can be subtracted from the data distribution when measuring F_2^γ.

5.4.4 W pair production

At LEP2, W pairs can be produced. They are rejected in a similar way to the hadronic Z^0 decays, but the cross-section is much lower than that of

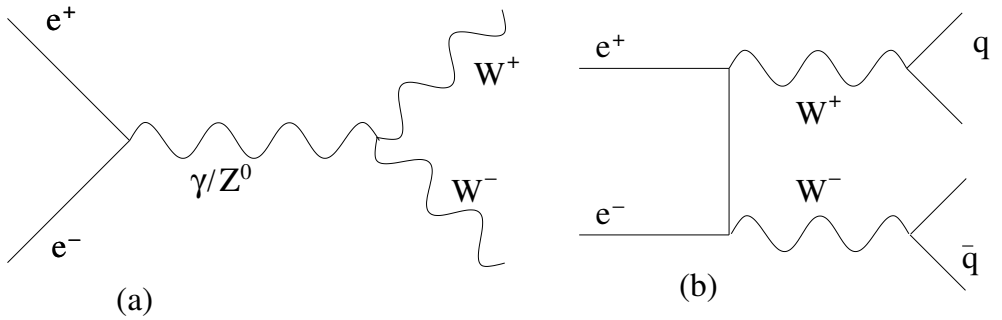

Figure 5.4: W pair production and decay: (a) annihilation, (b) conversion.

the Z^0 events at LEP1 and this background is small enough to neglect.

5.4.5 Non-multiperipheral four-fermion events

There are other processes besides two-photon events that produce four-fermion final states, but none have a high cross-section or a high probability to produce a tagged electron. The background from these processes is negligible.

5.4.6 Double-tagged two-photon events

These are the same type of events that make up the signal, but with a high enough value of P^2 that both of the scattered beam electrons are seen in the detector. The cross-section for $\gamma^\star\gamma^\star$ events is much lower than for $\gamma^\star\gamma$ events, but is not negligible. These events could cause several problems for the analysis: firstly, the approximation of real target photons breaks down for these events; secondly, they are not in the Monte Carlo samples that are used for comparison with the data, and thirdly, the second tagged electron would be included in the measurement of $W_{\rm vis}$, leading to an over-estimation of the hadronic energy. To reduce the number of these events, an anti-tag requirement is made on the energy of the most energetic cluster in the side

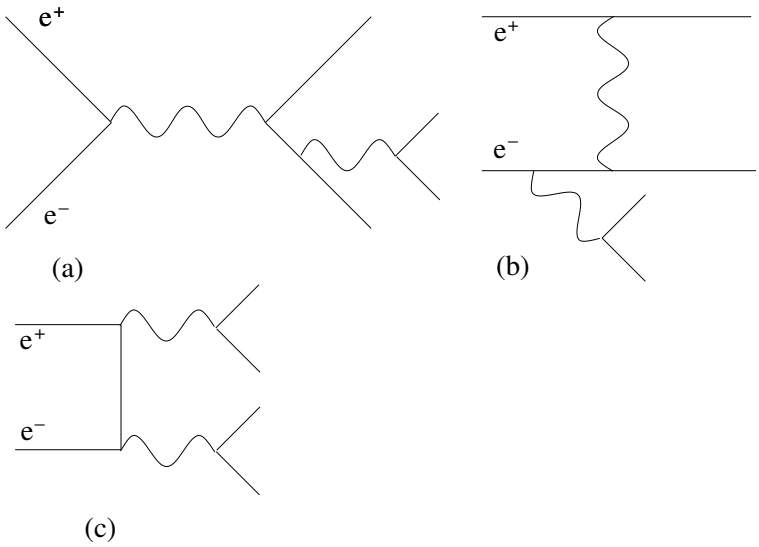

Figure 5.5: Non-multiperipheral four-fermion production: (a) annihilation, (b) bremsstrahlung, (c) conversion.

of the detector opposite the tag. This also has the effect of limiting the amount of energy that may be mistakenly included in the final state, for those double-tagged events which pass the cut.

5.4.7 Off-momentum electrons

If an electron interacts with gas in the beam pipe, it can be deflected by the focusing quadrupoles on either side of the OPAL detector at a sufficient angle to be observed in SW or FD. If this occurs at the same time as a hadronic Z^0 decay or untagged two-photon event, the combination can look like a tagged $\gamma^*\gamma$ event. Unlike physics events, these events are not symmetrical in ϕ. It is possible to see the effect of off-momentum electrons at low values of $E_{\rm tag}$ in the ϕ distribution (Figure 5.6). It can also be seen that above the minimum $E_{\rm tag}$ cut this background is negligible.

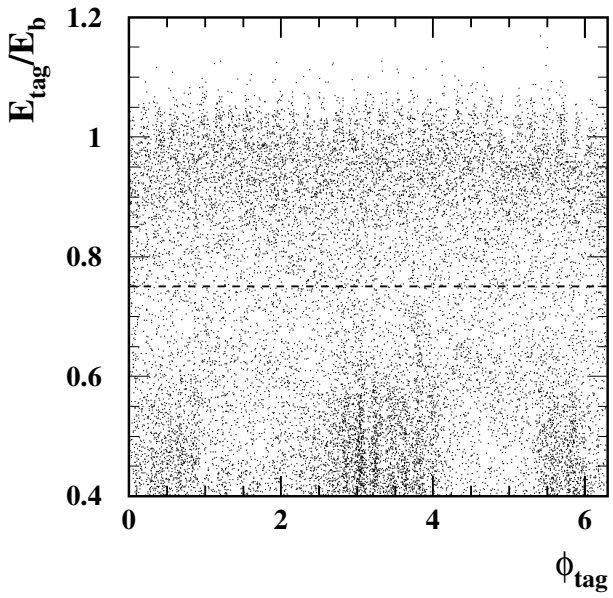

Figure 5.6: Energy against polar angle for the tagged electrons in the LEP2 SW sample. The dashed line represents the cut on the tag energy.

5.5 Estimation of the trigger efficiency

5.5.1 Estimation of trigger efficiency for the FD sample

Calculation of the trigger efficiency involves the use of two triggers that are statistically independent, i.e. the probability of one trigger firing is the same whether the other trigger fires or not.

With two triggers, A and B, the sample of N events can be divided into three classes:

- N_{A} events in which only trigger A fires,
- N_{B} events in which only trigger B fires, and
- N_{AB} events in which both triggers fire.

It is assumed that all relevant triggers are contained in either A or B, so that events in which neither trigger fires are not recorded.

The efficiencies of triggers A and B are

$$\epsilon_A = \frac{N_{AB}}{(N_{AB} + N_B)}, \quad \epsilon_B = \frac{N_{AB}}{(N_{AB} + N_A)}. \tag{5.1}$$

If A and B are independent, the total trigger efficiency is

$$\epsilon_{TOT} = \epsilon_A + \epsilon_B - \epsilon_A \epsilon_B. \tag{5.2}$$

For events with electrons tagged in FD, there are separate triggers for the tagged electron and for the hadronic final state. It is assumed that these triggers are independent, and the efficiency is calculated according to the method described above, using the following triggers:

- **Trigger A**:
  FDHIOR,
- **Trigger B**, logical OR of:
  TPTTTO[1]
  TPTTEM[2]
  TM3
  TPTOEM
  ((TBM1.or.EBTOTLO).and.(LCALLO.or.RCALLO))
  (TM1.and.(EELLO.or.EERLO.or.EBTOTLO)).

A description of these triggers signals is given in Table 2.1.

5.5.2 Estimation of trigger efficiency for the SW samples

For events with electrons tagged in SW, there is no trigger for the tagged electron that is independent of the hadronic final state triggers, because a

[1] From 1993, TPTTTO requires a coincidence with TBEBS.
[2] From 1993, TPTOEM requires a coincidence with EBWEDGE.

coincidence is required with the tracking or ECAL triggers. In this case, it is necessary to use a third trigger to check the correlation of the first two triggers. The third trigger is used to define a subset of N' events, which can be classified in a similar way to the case with two triggers described in Section 5.5.1 (but there is now an additional class):

- N_{NOT} events in which neither A nor B fire,
- N_{A} events in which only trigger A fires,
- N_{B} events in which only trigger B fires, and
- N_{AB} events in which both triggers fire.

The correlation of triggers A and B for the subset of events in which trigger C fires is

$$\mathrm{Corr}_{\mathrm{AB}} = \frac{\epsilon_{\mathrm{AB}} - \epsilon_{\mathrm{A}}\epsilon_{\mathrm{A}}}{\sigma_{\mathrm{A}}\sigma_{\mathrm{B}}} \tag{5.3}$$

where the efficiencies are now given by

$$\epsilon_{\mathrm{A}} = \frac{N_{\mathrm{AB}} + N_{\mathrm{A}}}{N'}, \quad \epsilon_{\mathrm{B}} = \frac{N_{\mathrm{AB}} + N_{\mathrm{B}}}{N'}, \quad \epsilon_{\mathrm{AB}} = \frac{N_{\mathrm{AB}}}{N'} \tag{5.4}$$

and the standard deviations are

$$\sigma_{\mathrm{A}} = \epsilon_{\mathrm{A}}(1 - \epsilon_{\mathrm{A}}), \quad \sigma_{\mathrm{B}} = \epsilon_{\mathrm{B}}(1 - \epsilon_{\mathrm{B}}). \tag{5.5}$$

It is assumed that the correlation of triggers A and B is independent of the firing state of trigger C. If the correlation between triggers A and B is small, a lower estimate for the total trigger efficiency is

$$\epsilon_{\mathrm{TOT}} = \epsilon_{\mathrm{A}} + \epsilon_{\mathrm{B}} - \epsilon_{\mathrm{A}}\epsilon_{\mathrm{B}}. \tag{5.6}$$

It is a lower estimate because it does not include the effect of trigger C on the total efficiency.

The triggers used to estimate the efficiencies for the SW tagged samples were

$\langle Q^2 \rangle$ [GeV^2]	sample	luminosity [pb^{-1}]	events	Q^2 range [GeV^2]
1.9	LEP1 SW	74.6	4356	1.5–2.5
3.7			4010	2.5–6.0
8.9	LEP1 FD	97.8	1909	6.0–12.0
17.5			1578	12.0–30.0
10.7	LEP2 SW	222.9	4593	7.0–13.0
17.8			5495	13.0–30.0

Table 5.6: The integrated luminosity, number of selected events in the data, Q^2 range, and trigger efficiency for each data sample. The error on the trigger efficiency is estimated to be about 1%.

- **Trigger A**, logical OR of:
  SWHIOR.and.(TPEML.or.TPEMR) (not active in 1993)
  SWHIOR.and.TBM1
  TPTTTO[3].and.TBEBS
  (TPEML.and.TPTTR).or.(TPEMR.and.TPTTL),

- **Trigger B**, logical OR of:
  (TM1.or.TPTO1[4]).and.(EELLO.or.EERLO.or.EBTOTLO)
  TPTOEM[5].and.EBWEDGE,

- **Trigger C**
  TPTTEM.

[3]Renamed TPTTOB in 1996
[4]Renamed TPTOB in 1996
[5]Renamed TPTOEMB in 1996

5.6 Comparison of data with Monte Carlo predictions

Figures 5.7 to 5.24 show data distributions compared to Monte Carlo for a number of variables.

The cross-section for the selected events is similar in the data and Monte Carlo samples, though the data is significantly higher than both HERWIG 5.9+k_t(dyn) and PHOJET 1.05 in the LEP1 SW sample.

The variables relating to the tagged electron (E_{tag}/E_b, θ_{tag} and Q^2) are generally well described by both Monte Carlo models (Figures 5.7 to 5.12). The cuts on the Q^2 distributions show how the samples are each divided into two Q^2 regions for the F_2^γ measurement.

The LEP1 SW data shows a higher peak at low E_a/E_b than either of the Monte Carlo samples. This suggests that the energy distribution of the particles in the final hadronic state is not perfectly described. The anti-tagged electrons do not influence this plot very much, as they are mostly at higher values of E_a/E_b.

PHOJET 1.05 has too few events at low W, which is a known problem with the program. For the unfolding, PHOJET 1.05 is reweighted in x (and therefore in W) to match HERWIG 5.9+k_t(dyn). For the plots in this section, the unweighted distributions are shown. The difference between HERWIG 5.9+k_t(dyn) and PHOJET 1.05 can be clearly seen in the x_{vis} distributions; Figures 5.16, 5.17 and 5.18.

There are some differences in the N_{ch} distributions (Figures 5.13b, 5.14b and 5.15b), with the Monte Carlo samples having on average fewer tracks than the data.

The variables E_T^{out}/E_{total} (Equation 4.3) and E_{for}/E_{total} are designed to be sensitive to the angular distribution of the hadrons in the final state. E_{for} is the total energy measured in SW and FD. These variables show that

the data has more energy in the central region of the detector than either of the Monte Carlo models (Figures 5.13, 5.14 and 5.15). This can also be seen in the energy flow plots; Figures 5.22, 5.23 and 5.24. Large peaks in the central region are characteristic of the 'pointlike' QED coupling of two photons. F2GEN, an entirely pointlike model, has peaks above the data in the central region.

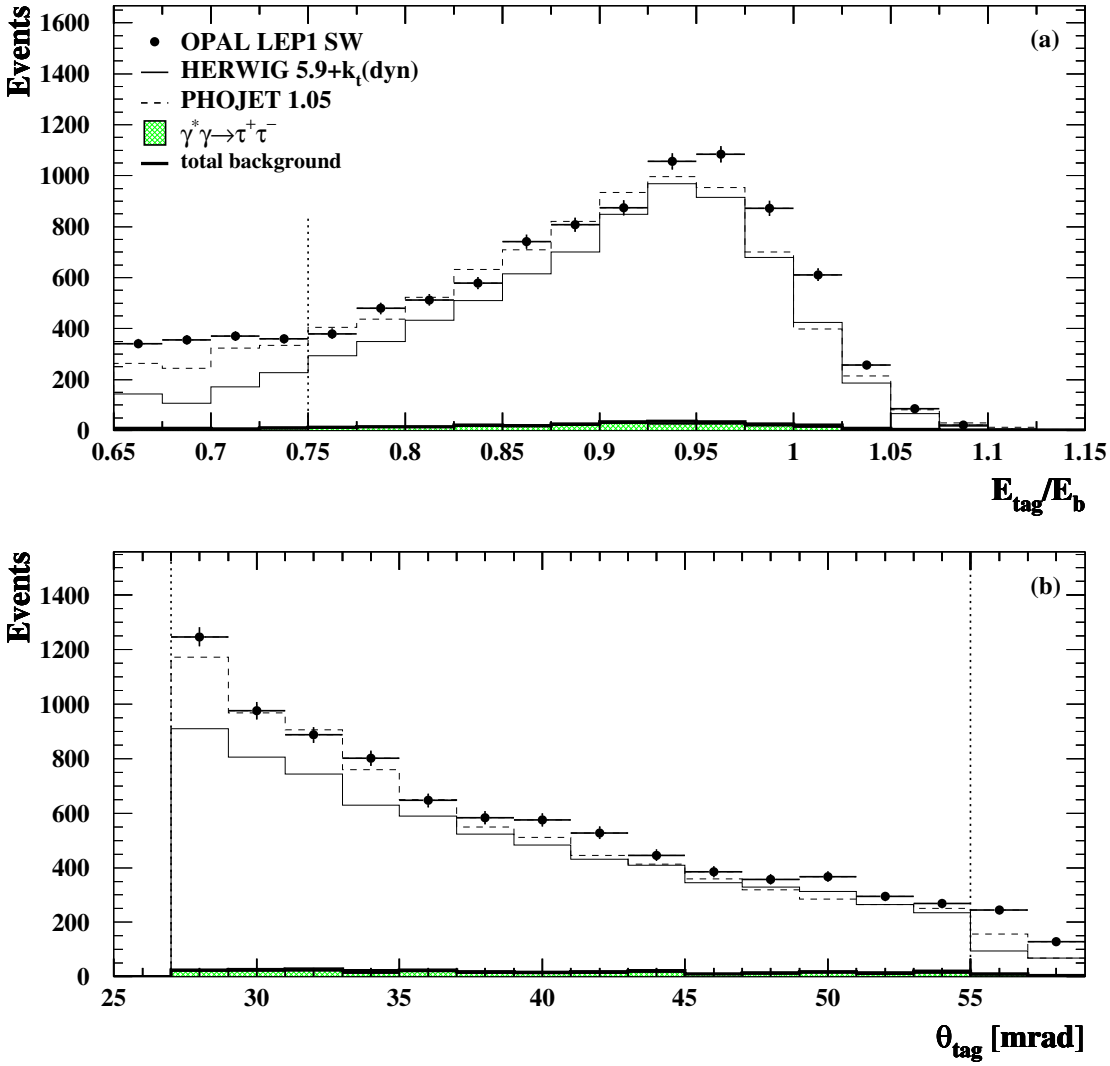

Figure 5.7: Comparison of data distributions with Monte Carlo predictions for the LEP1 SW sample. The dominant background source, $\gamma^{\star}\gamma \rightarrow \tau^{+}\tau^{-}$, the total background and the sum of the signal and the total background for HERWIG 5.9+k_{t}(dyn) and PHOJET 1.05 are shown. The Monte Carlo samples have been normalised to the data luminosity. All selection cuts have been applied, except for any cut on the variable in the plot. The cuts are shown as dotted lines. The errors are statistical only. The distributions shown are: a) $E_{\mathrm{tag}}/E_{\mathrm{b}}$, the energy of the tagged electron as a fraction of the beam energy, and b) θ_{tag}, the polar angle of the tagged electron.

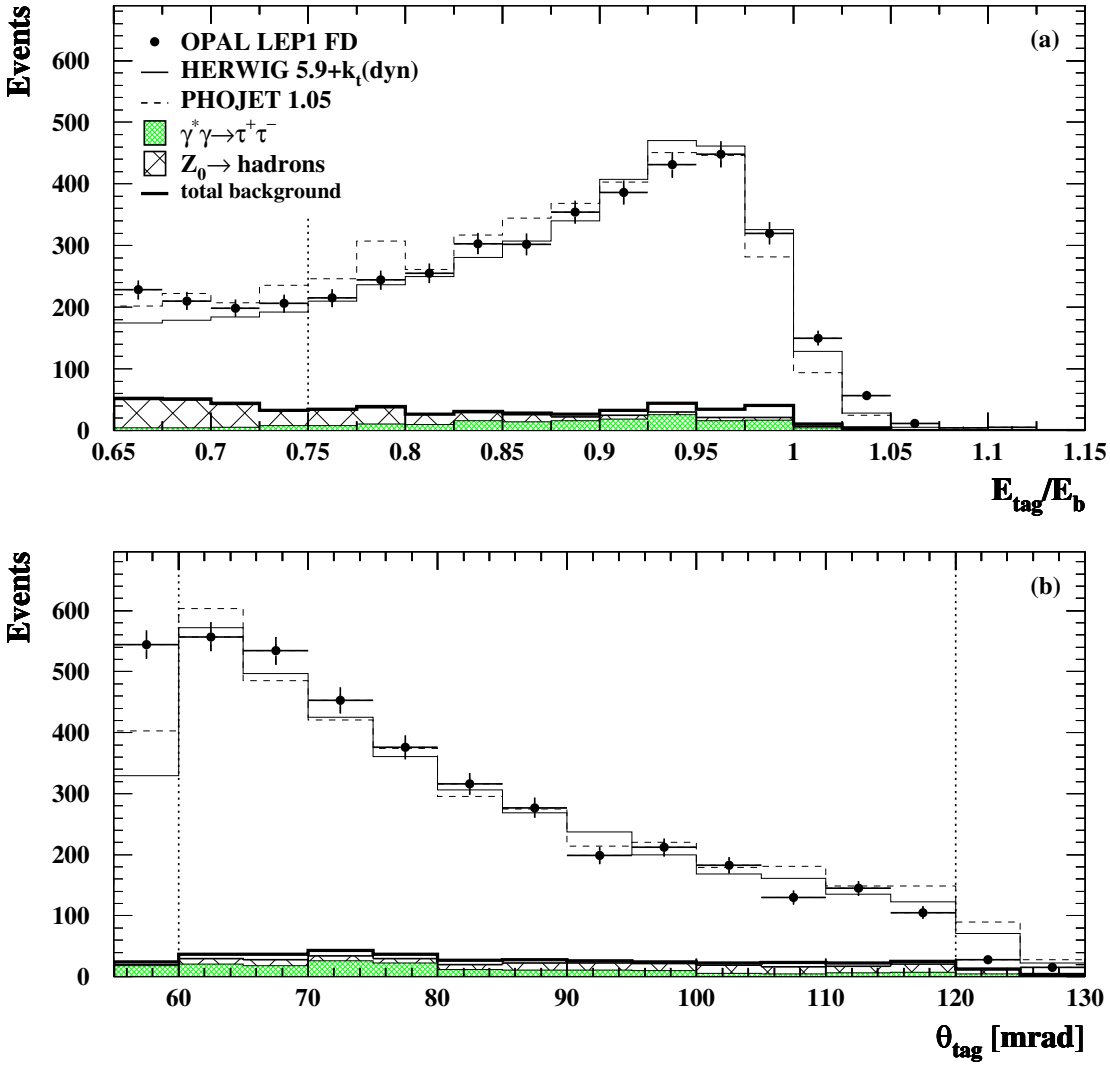

Figure 5.8: Comparison of data distributions with Monte Carlo predictions for the LEP1 FD sample. The dominant background sources, $\gamma^{\star}\gamma \rightarrow \tau^{+}\tau^{-}$ and $Z^{0} \rightarrow$ hadrons, the total background and the sum of the signal and the total background for HERWIG 5.9+k_{t}(dyn) and PHOJET 1.05 are shown. The Monte Carlo samples have been normalised to the data luminosity. All selection cuts have been applied, except for any cut on the variable in the plot. The cuts are shown as dotted lines. The errors are statistical only. The variables in the plots are as defined in Figure 5.7.

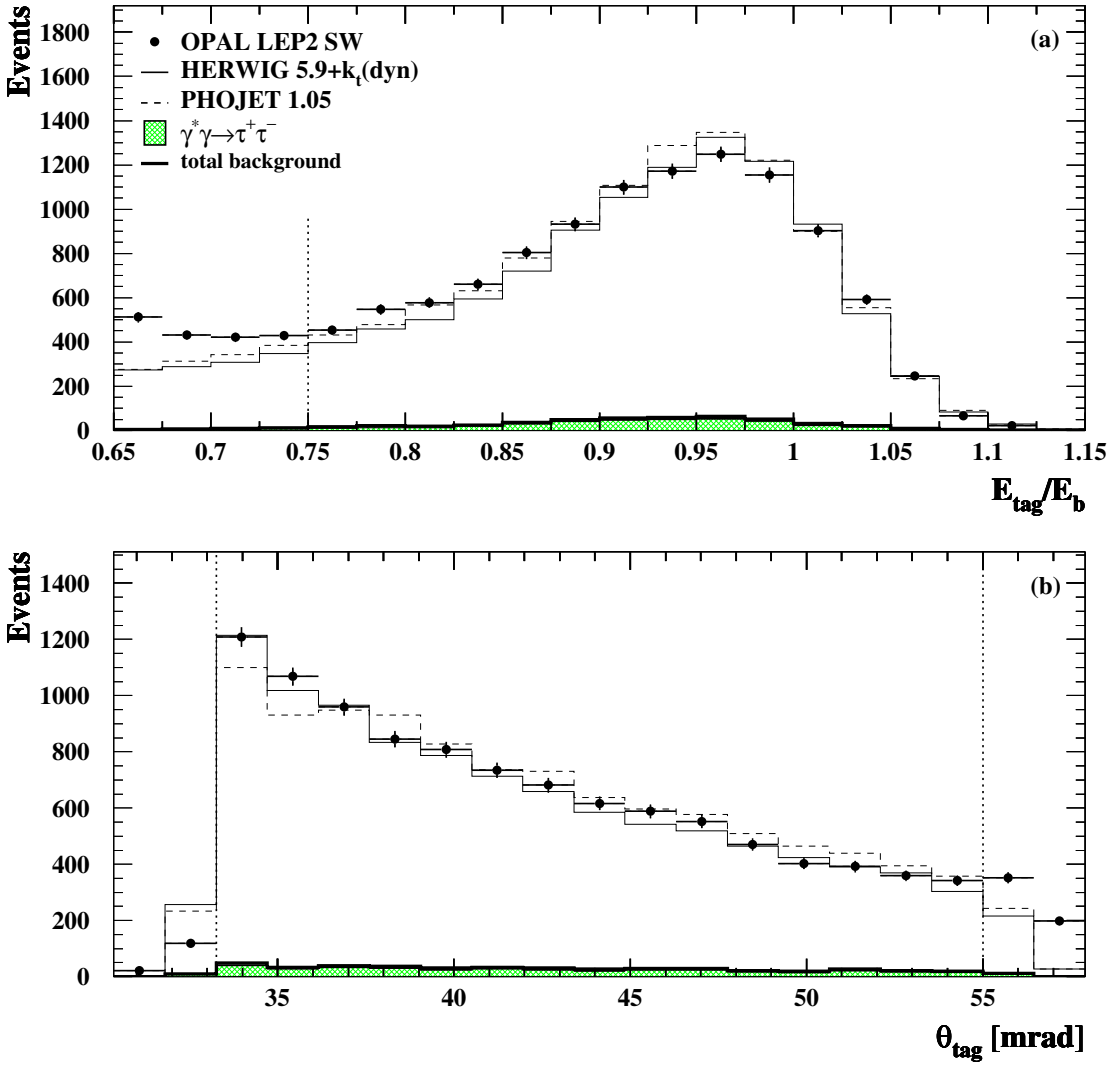

Figure 5.9: Comparison of data distributions with Monte Carlo predictions for the LEP2 SW sample. The dominant background source, $\gamma^{\star}\gamma \rightarrow \tau^{+}\tau^{-}$, the total background and the sum of the signal and the total background for HERWIG 5.9+k_{t}(dyn) and PHOJET 1.05 are shown. The Monte Carlo samples have been normalised to the data luminosity. All selection cuts have been applied, except for any cut on the variable in the plot. The cuts are shown as dotted lines. The errors are statistical only. The variables in the plots are as defined in Figure 5.7.

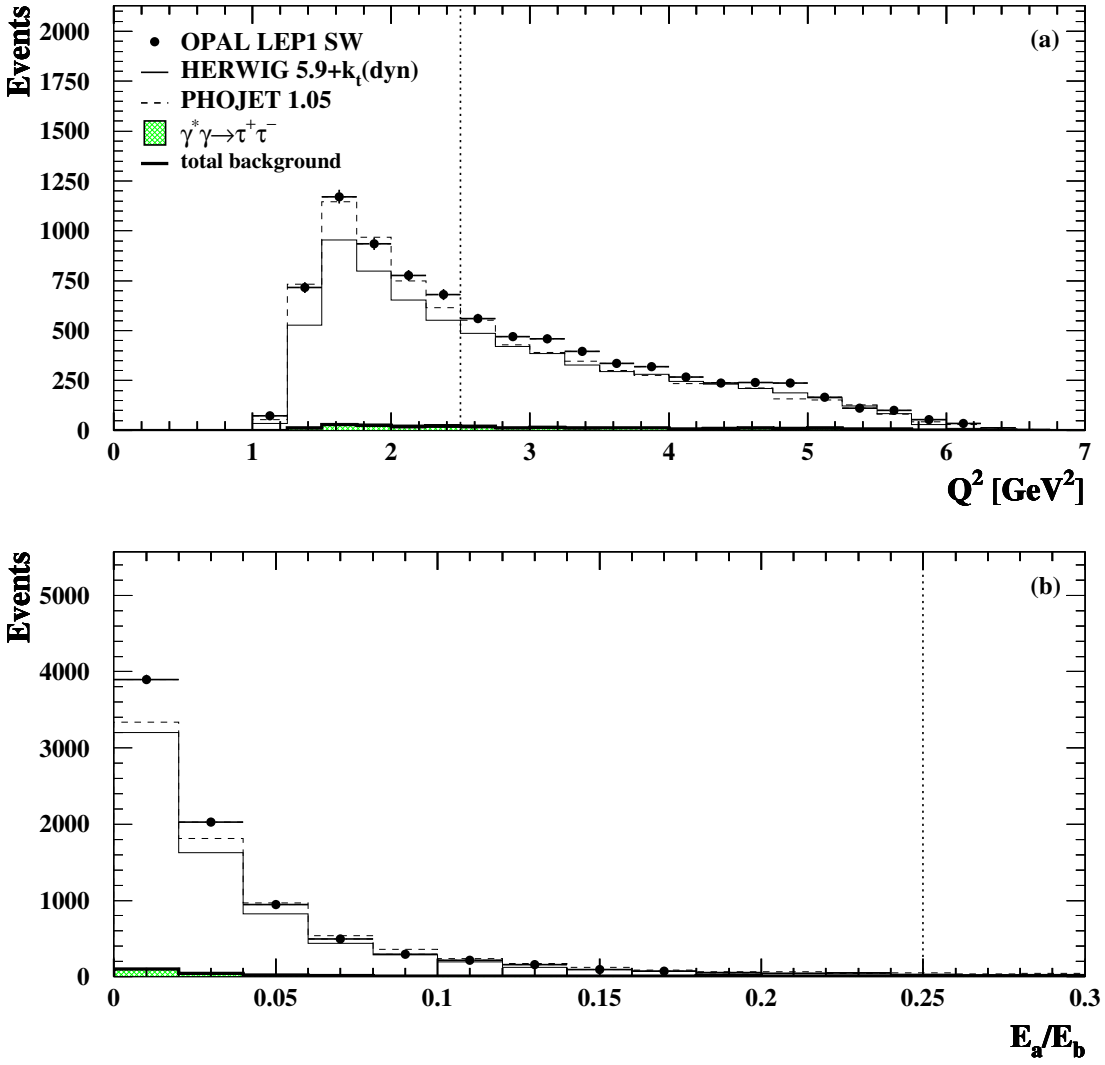

Figure 5.10: Comparison of data distributions with Monte Carlo predictions for the LEP1 SW sample. The dominant background source, $\gamma^{\star}\gamma \rightarrow \tau^{+}\tau^{-}$, the total background and the sum of the signal and the total background for HERWIG 5.9+k_{t}(dyn) and PHOJET 1.05 are shown. The Monte Carlo samples have been normalised to the data luminosity. All selection cuts have been applied, except for any cut on the variable in the plot. The cuts are shown as dotted lines. The errors are statistical only. The distributions shown are: a) the measured Q^2, and b) $E_{\mathrm{a}}/E_{\mathrm{b}}$, the energy of the most energetic electromagnetic cluster in the hemisphere opposite the tagged electron, as a fraction of the beam energy.

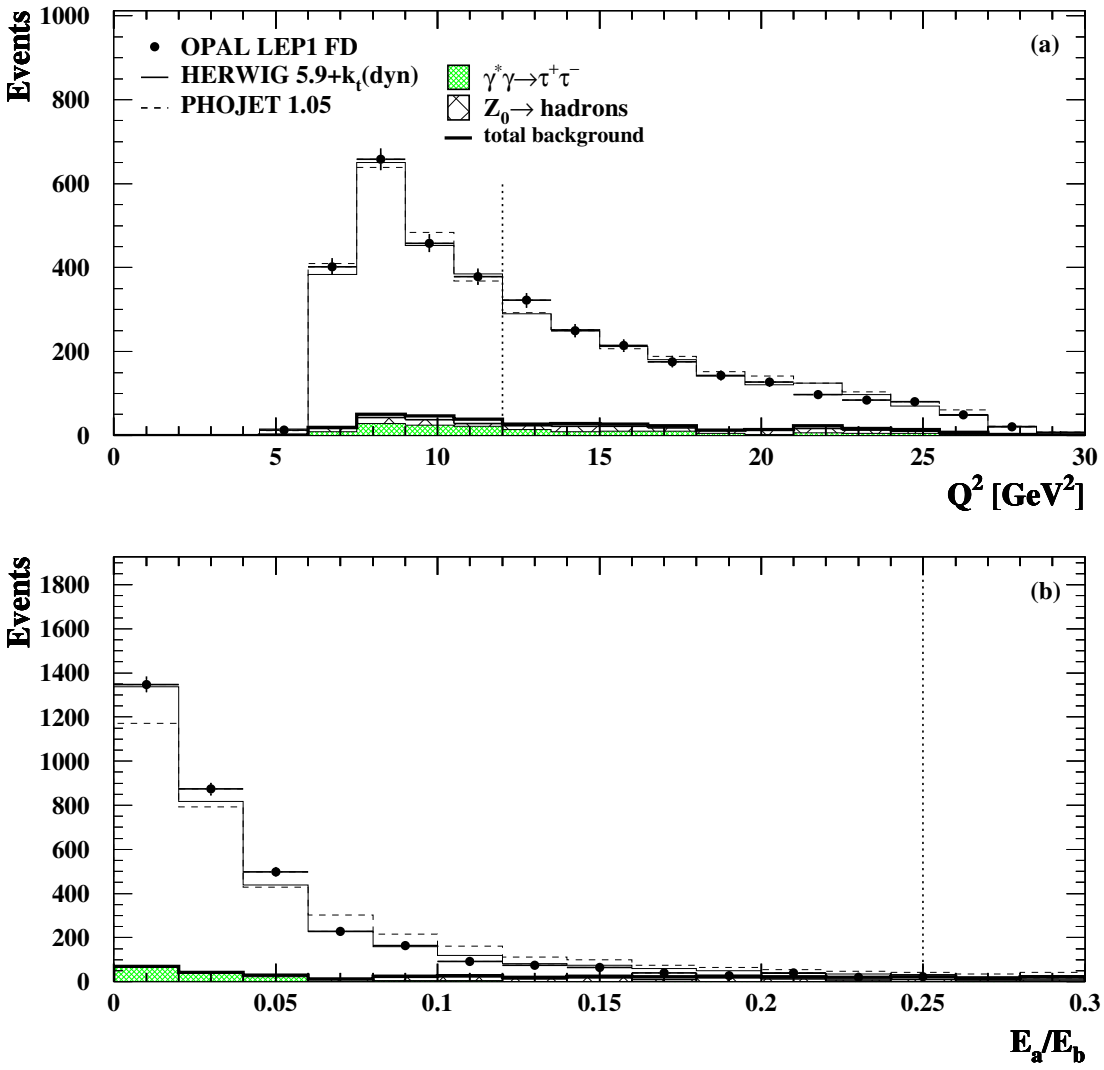

Figure 5.11: Comparison of data distributions with Monte Carlo predictions for the LEP1 SW sample. The dominant background sources, $\gamma^{\star}\gamma \to \tau^{+}\tau^{-}$ and $Z^{0} \to$ hadrons, the total background and the sum of the signal and the total background for HERWIG 5.9+k_{t}(dyn) and PHOJET 1.05 are shown. The Monte Carlo samples have been normalised to the data luminosity. All selection cuts have been applied, except for any cut on the variable in the plot. The cuts are shown as dotted lines. The errors are statistical only. The variables in the plots are as defined in Figure 5.10.

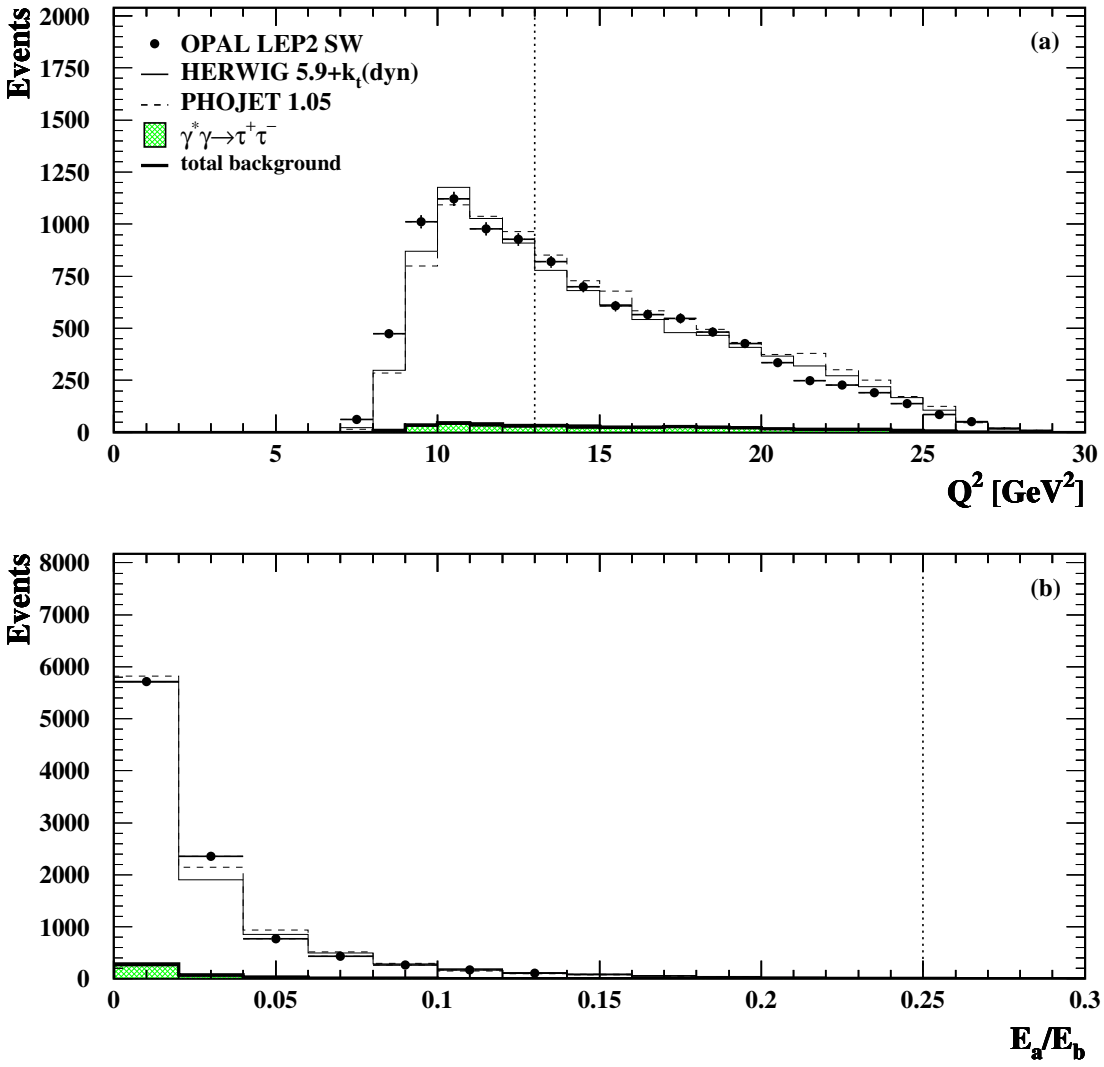

Figure 5.12: Comparison of data distributions with Monte Carlo predictions for the LEP2 SW sample. The dominant background source, $\gamma^{\star}\gamma \rightarrow \tau^{+}\tau^{-}$, the total background and the sum of the signal and the total background for HERWIG 5.9+k_{t}(dyn) and PHOJET 1.05 are shown. The Monte Carlo samples have been normalised to the data luminosity. All selection cuts have been applied, except for any cut on the variable in the plot. The cuts are shown as dotted lines. The errors are statistical only. The variables in the plots are as defined in Figure 5.10.

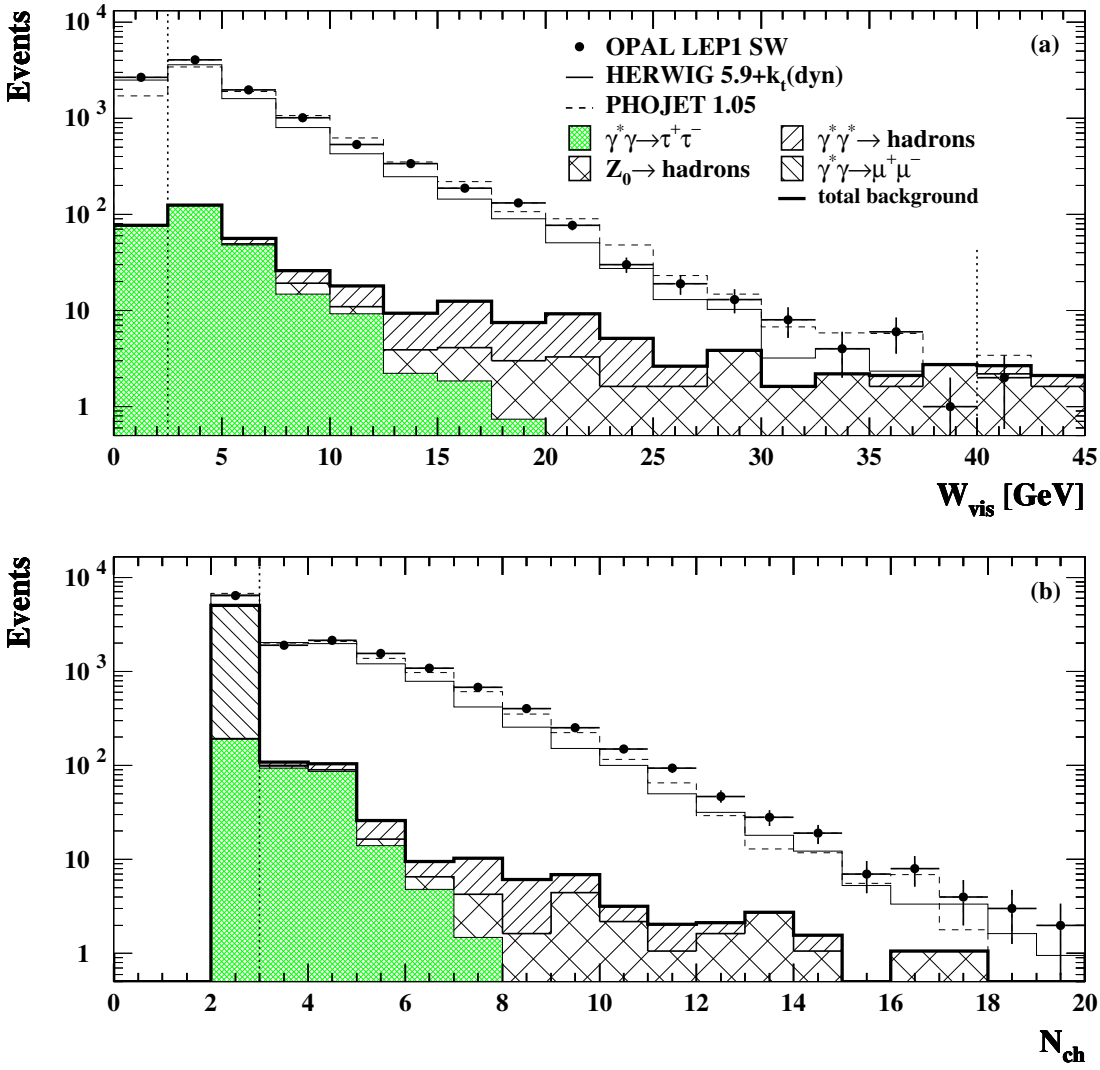

Figure 5.13: Comparison of data distributions with Monte Carlo predictions for the LEP1 SW sample. The dominant background sources, $\gamma^{\star}\gamma \rightarrow \tau^{+}\tau^{-}$, $Z^0 \rightarrow$ hadrons and $\gamma^{\star}\gamma^{\star} \rightarrow$ hadrons ($P^2 > 1.0$ GeV^2), the total background and the sum of the signal and the total background for HERWIG 5.9+k_t(dyn) and PHOJET 1.05 are shown. The Monte Carlo samples have been normalised to the data luminosity. All selection cuts have been applied, except for any cut on the variable in the plot. The cuts are shown as dotted lines. The errors are statistical only. The distributions shown are: a) $W_{\rm vis}$, the measured invariant mass of the hadronic final state, and b) $N_{\rm ch}$, the number of charged tracks in the event.

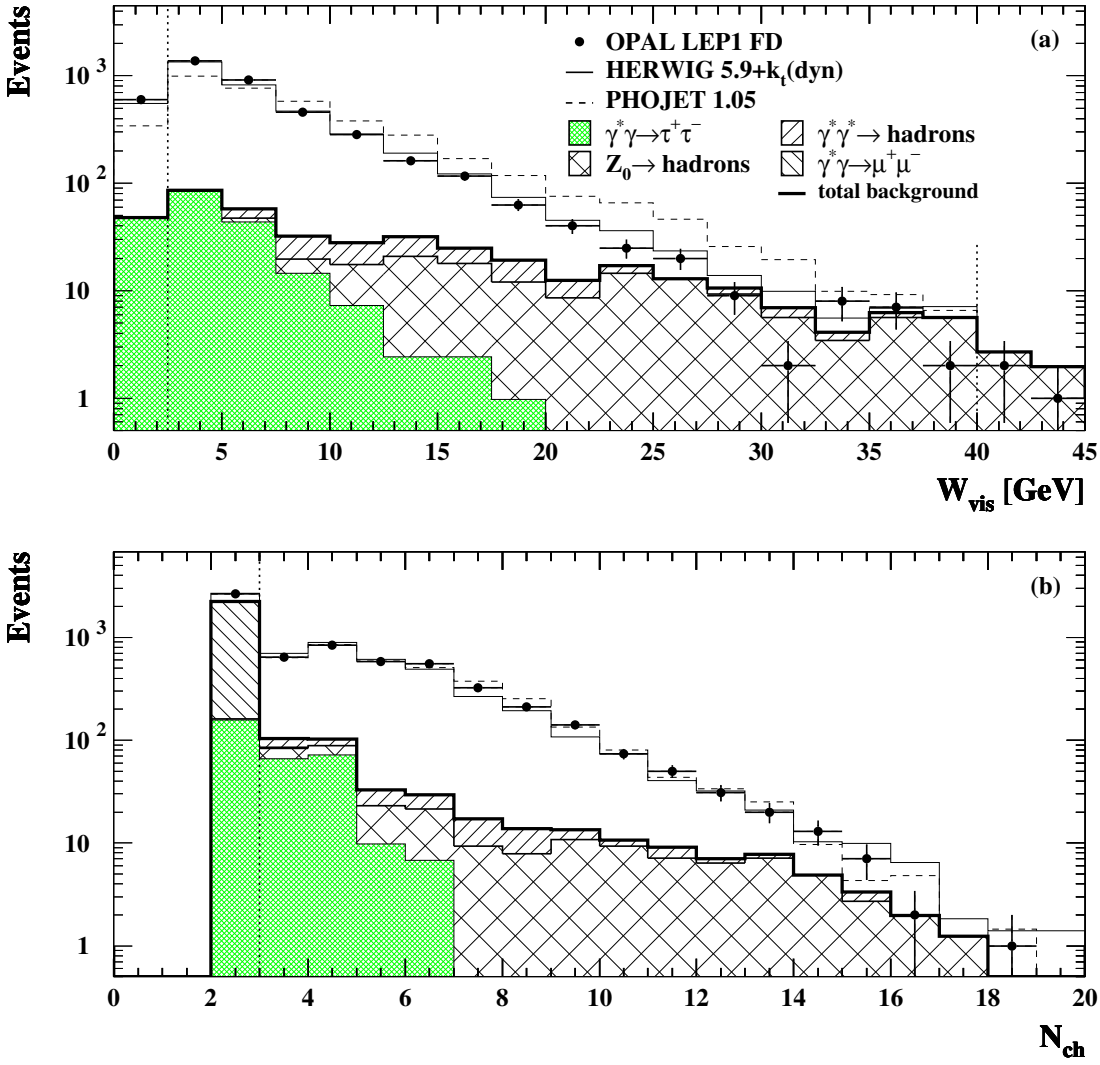

Figure 5.14: Comparison of data distributions with Monte Carlo predictions for the LEP1 FD sample. The dominant background sources, $\gamma^{\star}\gamma \rightarrow \tau^{+}\tau^{-}$, $Z^0 \rightarrow$ hadrons and $\gamma^{\star}\gamma^{\star} \rightarrow$ hadrons ($P^2 > 1.0$ GeV^2), the total background and the sum of the signal and the total background for HERWIG 5.9+k_t(dyn) and PHOJET 1.05 are shown. The Monte Carlo samples have been normalised to the data luminosity. All selection cuts have been applied, except for any cut on the variable in the plot. The cuts are shown as dotted lines. The errors are statistical only. The variables in the plots are as defined in Figure 5.13.

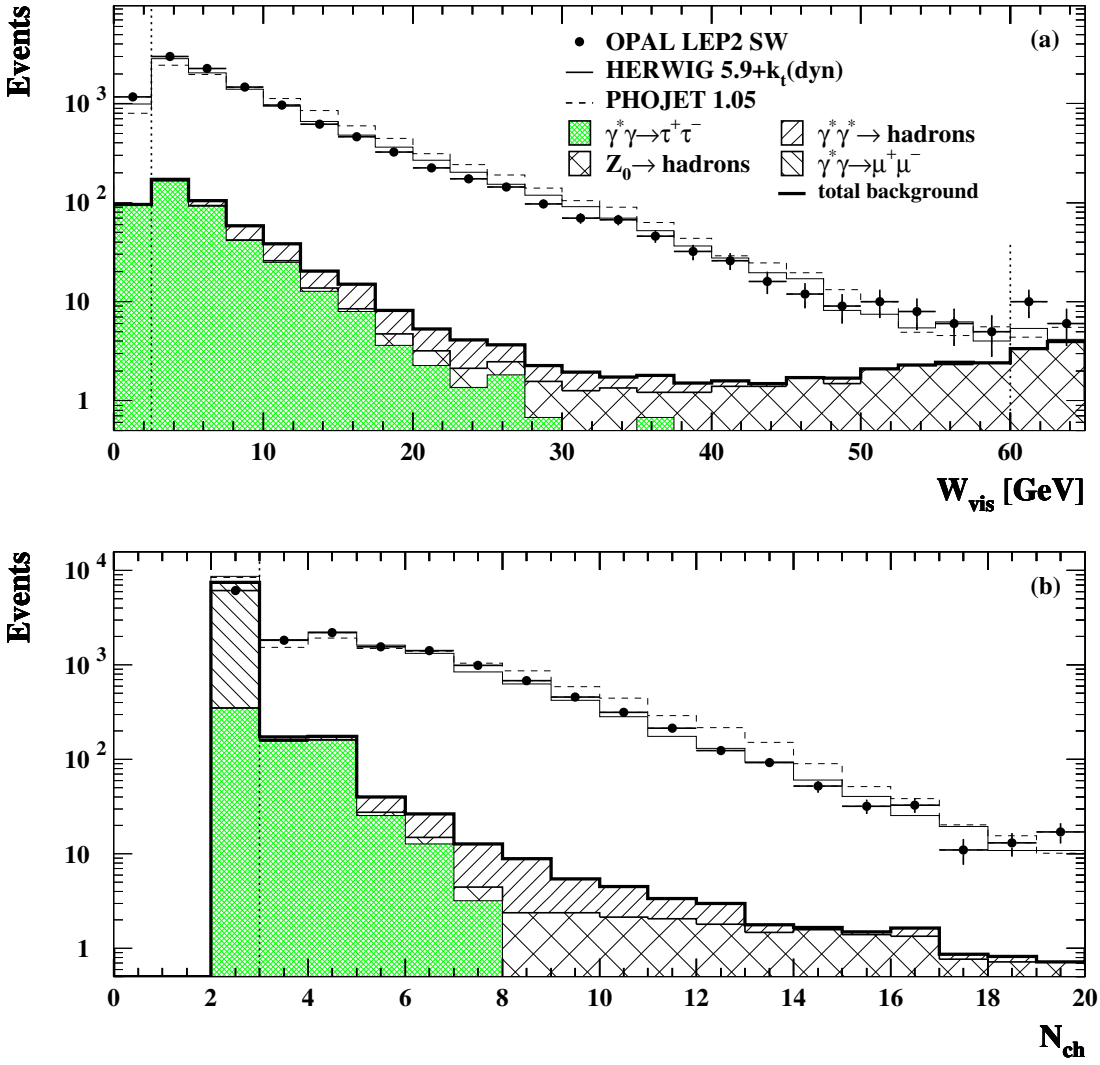

Figure 5.15: Comparison of data distributions with Monte Carlo predictions for the LEP2 SW sample. The dominant background sources, $\gamma^\star\gamma \to \tau^+\tau^-$, $Z^0 \to$ hadrons and $\gamma^\star\gamma^\star \to$ hadrons ($P^2 > 4.5$ GeV^2), the total background and the sum of the signal and the total background for HERWIG 5.9+k_t(dyn) and PHOJET 1.05 are shown. The Monte Carlo samples have been normalised to the data luminosity. All selection cuts have been applied, except for any cut on the variable in the plot. The cuts are shown as dotted lines. The errors are statistical only. The variables in the plots are as defined in Figure 5.13.

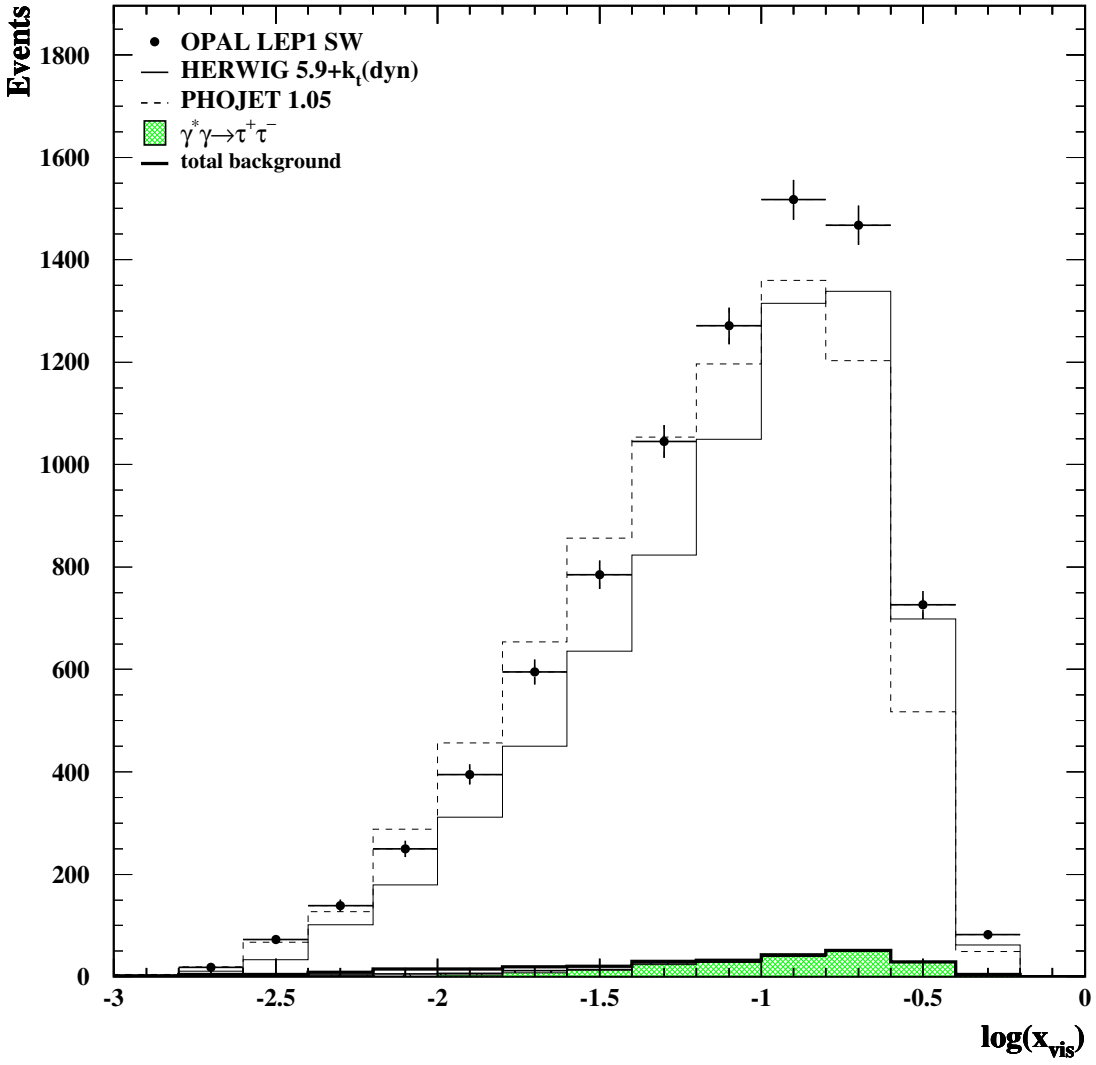

Figure 5.16: Comparison of the data $x_{\rm vis}$ distribution with Monte Carlo predictions for the LEP1 SW sample. The dominant background source, $\gamma^\star\gamma \to \tau^+\tau^-$, the total background and the sum of the signal and the total background for HERWIG 5.9+$k_{\rm t}$(dyn) and PHOJET 1.05 are shown. The Monte Carlo samples have been normalised to the data luminosity. All selection cuts have been applied, except for any cut on the variable in the plot. The cuts are shown as dotted lines. The errors are statistical only.

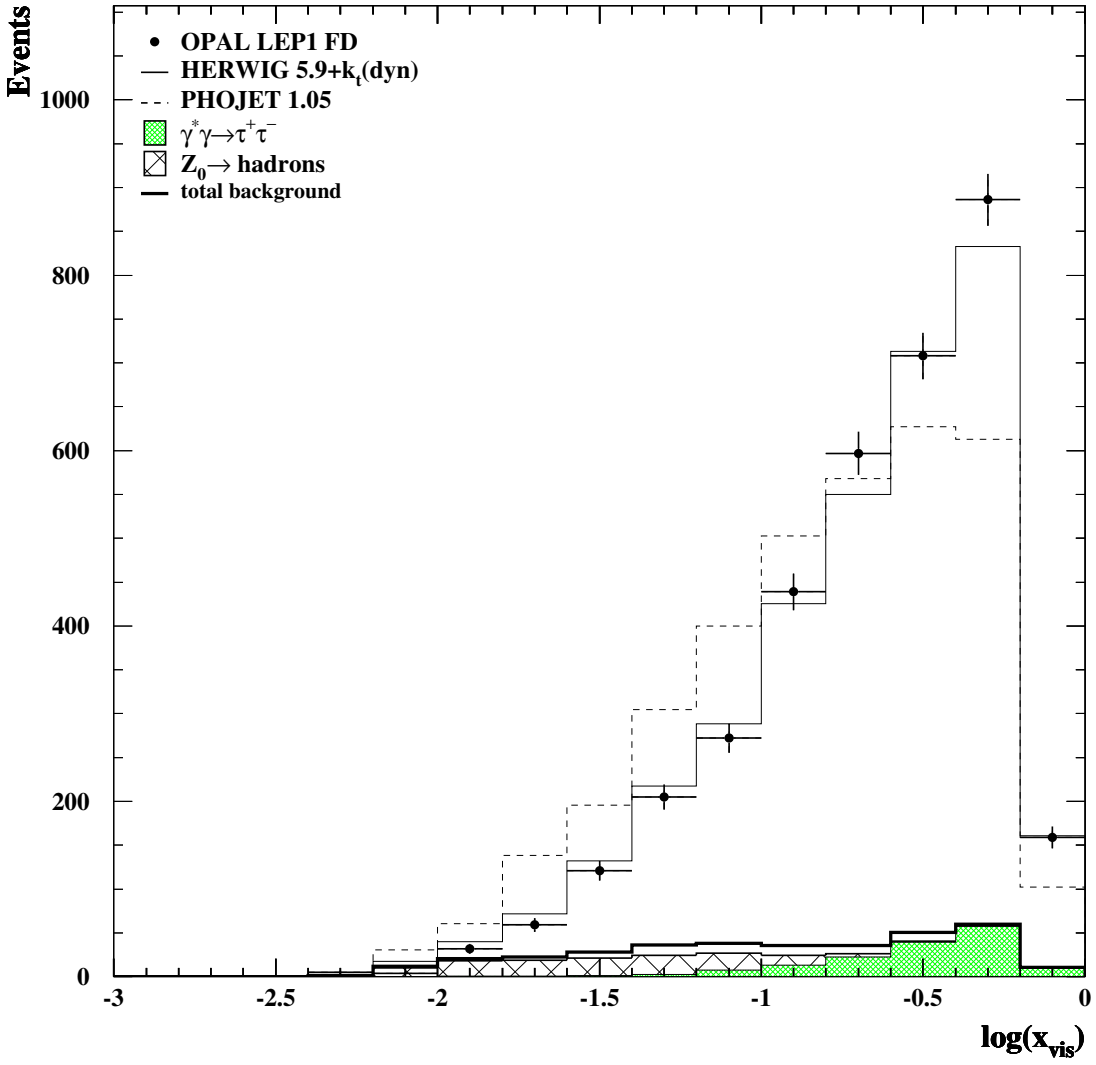

Figure 5.17: Comparison of the data $x_{\rm vis}$ distribution with Monte Carlo predictions for the LEP1 FD sample. The dominant background sources, $\gamma^\star\gamma \to \tau^+\tau^-$ and $\mathrm{Z}^0 \to$ hadrons, the total background and the sum of the signal and the total background for HERWIG 5.9+$k_{\rm t}$(dyn) and PHOJET 1.05 are shown. The Monte Carlo samples have been normalised to the data luminosity. All selection cuts have been applied, except for any cut on the variable in the plot. The cuts are shown as dotted lines. The errors are statistical only.

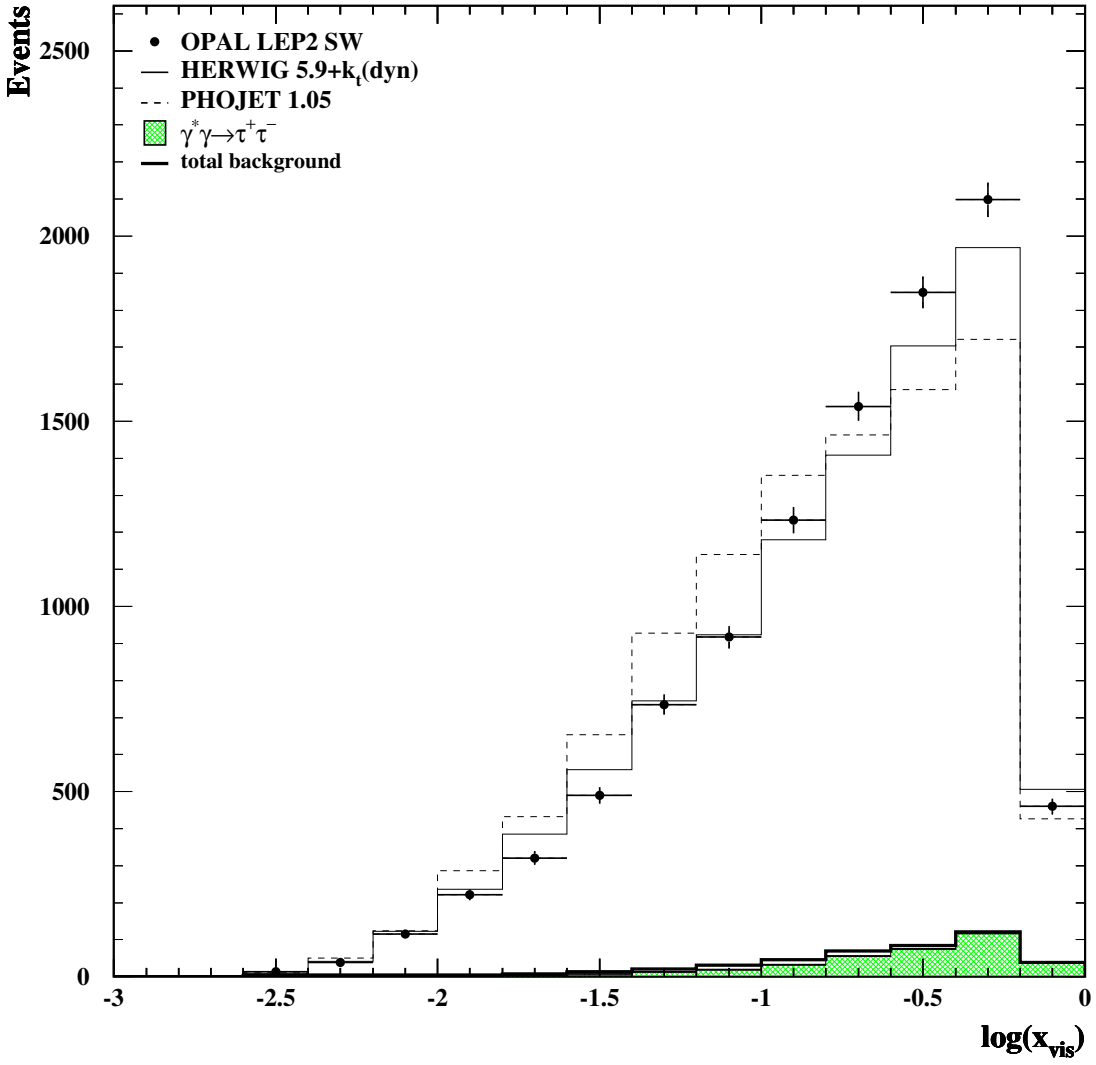

Figure 5.18: Comparison of the data $x_{\rm vis}$ distribution with Monte Carlo predictions for the LEP2 SW sample. The dominant background source, $\gamma^\star\gamma \to \tau^+\tau^-$, the total background and the sum of the signal and the total background for HERWIG 5.9+$k_{\rm t}$(dyn) and PHOJET 1.05 are shown. The Monte Carlo samples have been normalised to the data luminosity. All selection cuts have been applied, except for any cut on the variable in the plot. The cuts are shown as dotted lines. The errors are statistical only.

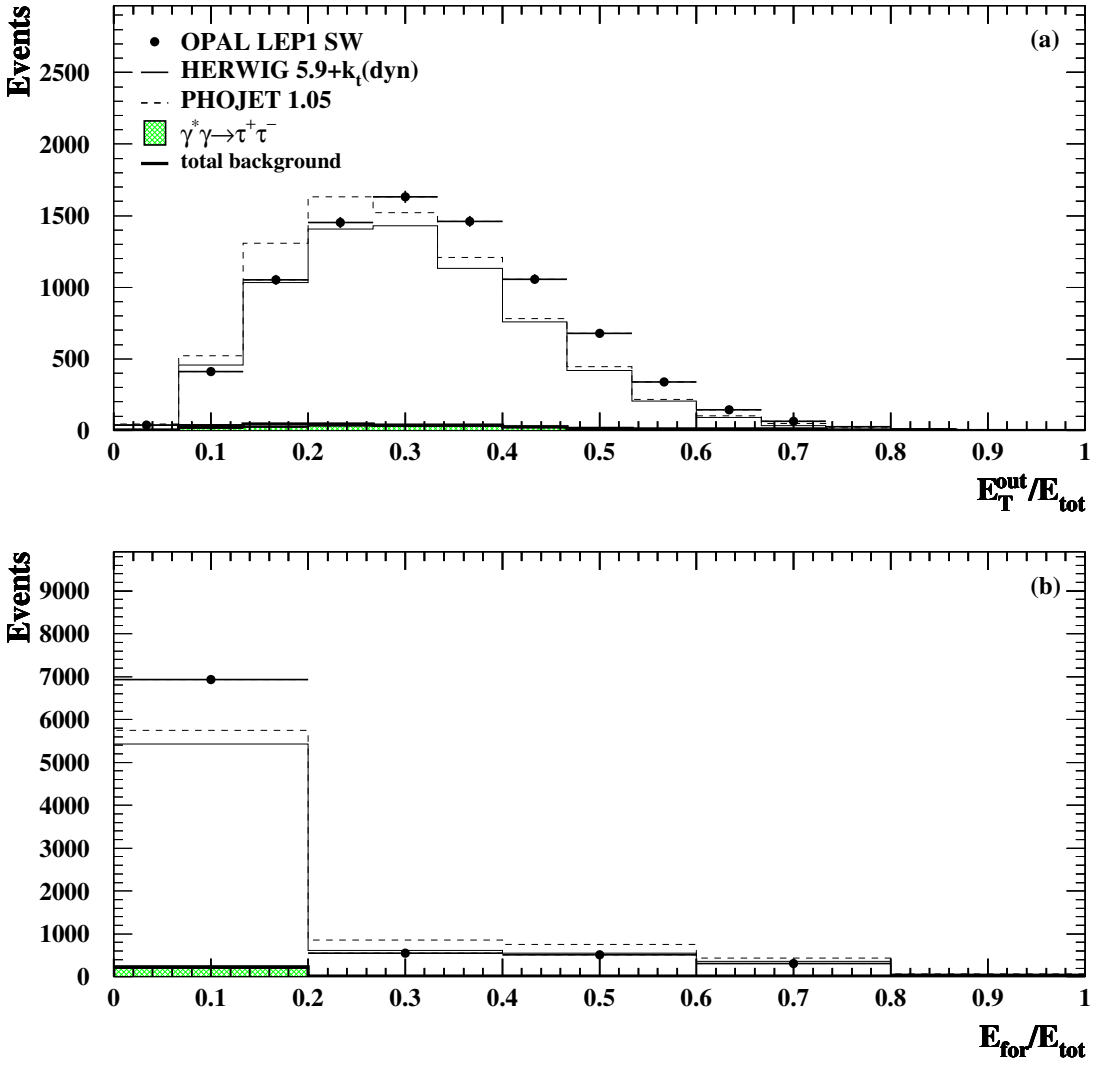

Figure 5.19: Comparison of data distributions with Monte Carlo predictions for the LEP1 SW sample. The dominant background source, $\gamma^{\star}\gamma \rightarrow \tau^{+}\tau^{-}$, the total background and the sum of the signal and the total background for HERWIG 5.9+k_{t}(dyn) and PHOJET 1.05 are shown. The Monte Carlo samples have been normalised to the data luminosity. All selection cuts have been applied, except for any cut on the variable in the plot. The cuts are shown as dotted lines. The errors are statistical only. The distributions shown are: (a) $E_{\mathrm{T}}^{\mathrm{out}}/E_{\mathrm{total}}$, the transverse hadronic energy out of the plane containing the beam line and the tagged electron, divided by the total observed energy, and (b) $E_{\mathrm{for}}/E_{\mathrm{total}}$, the observed energy in the forward regions divided by the total observed energy.

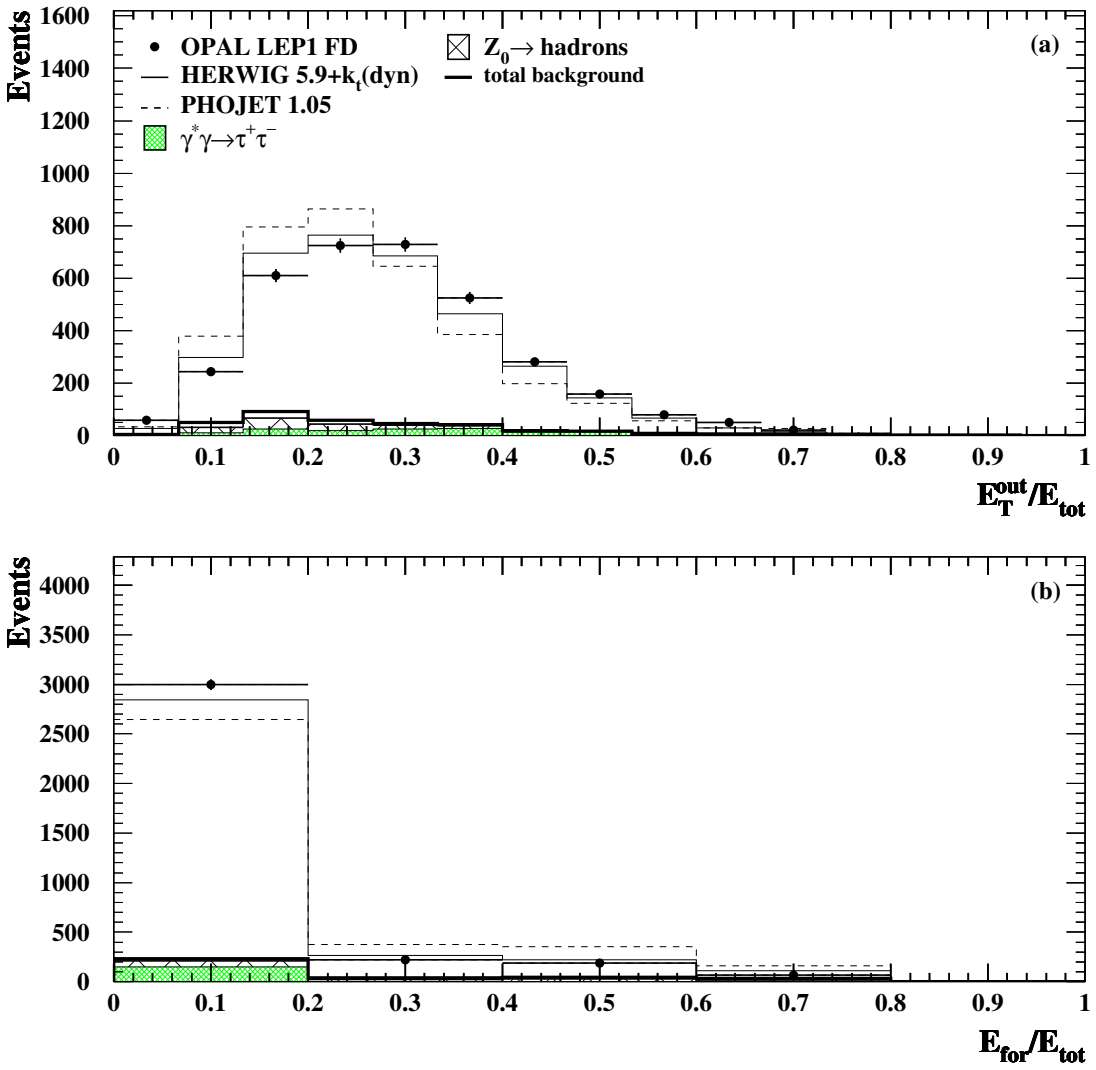

Figure 5.20: Comparison of data distributions with Monte Carlo predictions for the LEP1 FD sample. The dominant background sources, $\gamma^{\star}\gamma \rightarrow \tau^{+}\tau^{-}$ and $Z^{0} \rightarrow$ hadrons, the total background and the sum of the signal and the total background for HERWIG 5.9+k_{t}(dyn) and PHOJET 1.05 are shown. The Monte Carlo samples have been normalised to the data luminosity. All selection cuts have been applied, except for any cut on the variable in the plot. The cuts are shown as dotted lines. The errors are statistical only. The variables in the plots are as defined in Figure 5.19.

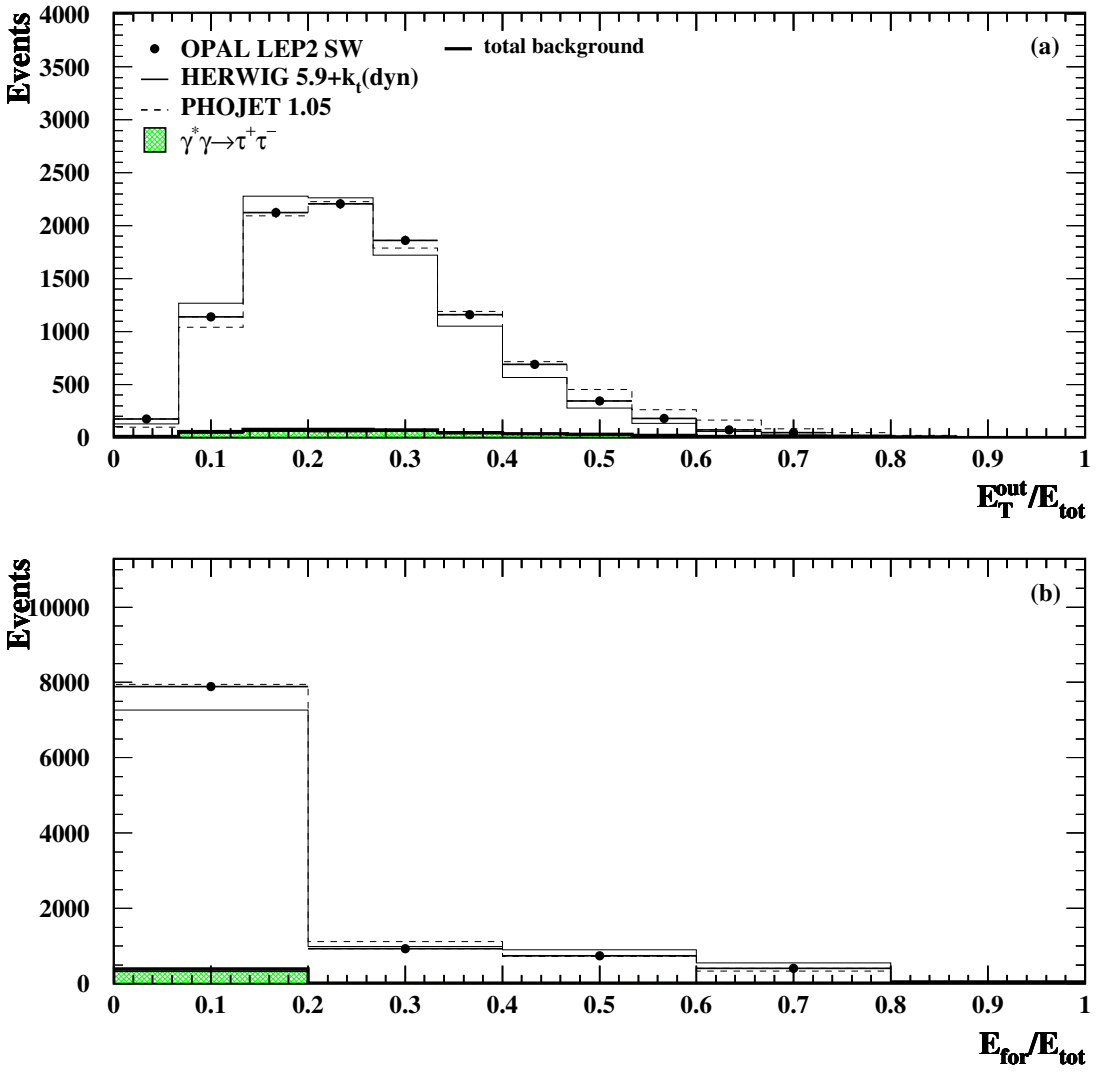

Figure 5.21: Comparison of data distributions with Monte Carlo predictions for the LEP2 SW sample. The dominant background source, $\gamma^{\star}\gamma \rightarrow \tau^{+}\tau^{-}$, the total background and the sum of the signal and the total background for HERWIG 5.9+k_{t}(dyn) and PHOJET 1.05 are shown. The Monte Carlo samples have been normalised to the data luminosity. All selection cuts have been applied, except for any cut on the variable in the plot. The cuts are shown as dotted lines. The errors are statistical only. The variables in the plots are as defined in Figure 5.19.

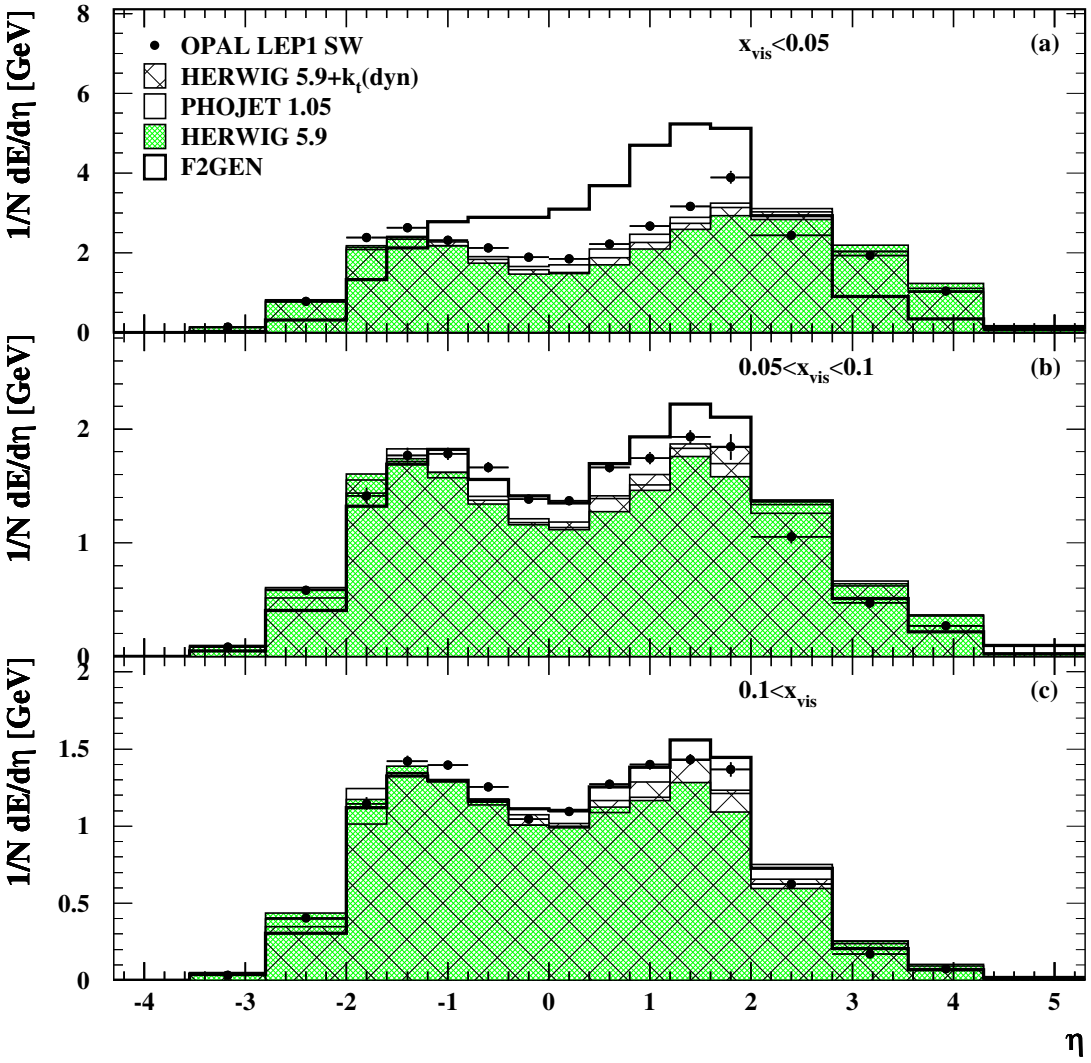

Figure 5.22: Comparison of hadronic energy flow per event as a function of the pseudorapidity, $\eta = -\log(\tan(\theta/2))$, where θ is measured with respect to the beam axis on the tag side, for the LEP1 SW sample. The samples are divided into three bins of $x_{\rm vis}$. The errors are statistical only.

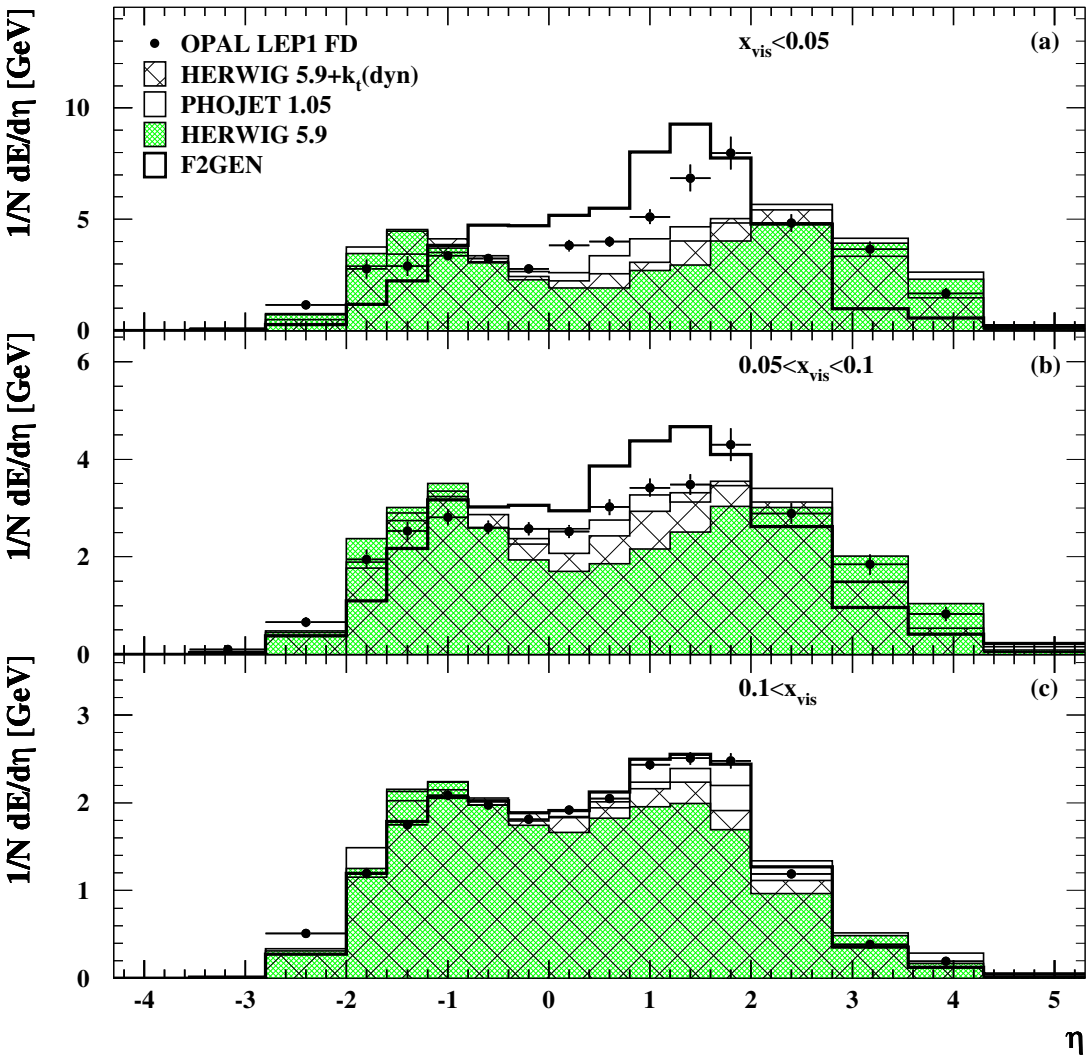

Figure 5.23: Comparison of hadronic energy flow per event as a function of the pseudorapidity, $\eta = -\log(\tan(\theta/2))$, where θ is measured with respect to the beam axis on the tag side, for the LEP1 FD sample. The samples are divided into three bins of $x_{\rm vis}$. The errors are statistical only.

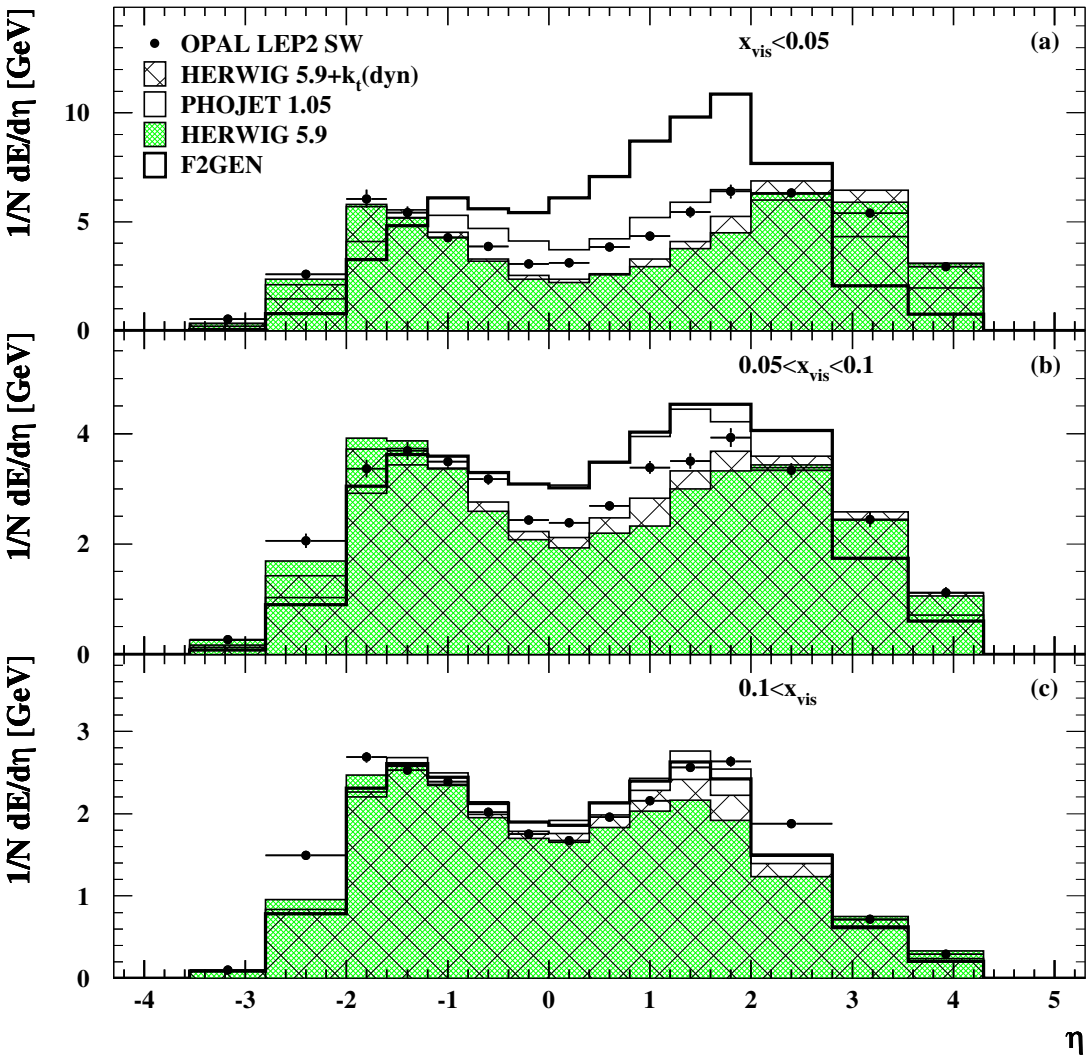

Figure 5.24: Comparison of hadronic energy flow per event as a function of the pseudorapidity, $\eta = -\log(\tan(\theta/2))$, where θ is measured with respect to the beam axis on the tag side, for the LEP2 SW sample. The samples are divided into three bins of $x_{\rm vis}$. The errors are statistical only.

Chapter 6

Unfolding

With a perfect detector, F_2^γ could be determined simply by measuring the distribution of events in x and Q^2. In practice this is not possible because

- not all events are observed, due to the finite efficiency of the detector,
- the measured value of x is smeared because of the limited resolution of the detector, and there are migrations from one region of x to another, and
- there is some contamination from background events.

Without correcting for detector effects it would be impossible to compare to the results of other experiments, and comparisons with theoretical predictions would be difficult. The correction involves using Monte Carlo events that have been passed through a simulation of the detector.

Background from physics processes is simulated and subtracted from the measured distributions. Non-physics background such as caused by off-momentum electrons cannot be easily simulated, but is excluded by the selection cuts.

The most difficult detector effects to correct are limited resolution and migration. This is because the problem is ill-defined: it is unstable against

small changes in the initial system, and a given measured distribution could have arisen (within statistical errors) from a wide range of different true distributions. To avoid this problem, it is usually necessary to assume something about the answer, typically that it is a smooth distribution, which is a reasonable assumption in the case of structure functions.

Resolution, migration and detection efficiency can be corrected simultaneously by unfolding. There are several unfolding programs available. For this analysis, GURU [60] was used as the main unfolding program. The results from GURU were compared to those from RUN [61] and a Bayesian unfolding program [62] (referred to in this thesis as BAYES).

6.1 The unfolding problem

In general, the effect of an imperfect detector can be described by a response function A, defined by

$$g(y) = \int A(x,y) f(x)\, dx + b(y). \tag{6.1}$$

The function $f(x)$ is the true distribution to be measured. The function $g(y)$ is the 'expected' measured distribution, and $b(y)$ is the total background. Because the true and measured variables can be different, they are called x and y respectively. The function $g(y)$ differs from the actual measured distribution $d(y)$, because of statistical errors $e(y)$;

$$d(y) = \int A(x,y) f(x)\, dx + e(y). \tag{6.2}$$

For simplicity in subsequent formulae, $d(y)$ is defined to be the background-subtracted distribution.

To solve the problem numerically, the distributions must be discretised. Equation 6.1 becomes

$$g_j = \sum_{i=1}^{n} A_{ij} f_i + b_j. \tag{6.3}$$

A_{ij} is the probability for an event in bin i of the true distribution (with n bins) to be detected in bin j of the measured distribution (with m bins), Equation 6.3 can also be expressed as a matrix equation,

$$g = Af + b \tag{6.4}$$

where A is an $n \times m$ matrix and g, b and f are vectors corresponding to the distributions.

If A^{-1} exists, and in the absence of statistical errors, this equation can be solved very easily;

$$\hat{f} = A^{-1}d. \tag{6.5}$$

The matrix A is determined from Monte Carlo simulation. (The vector $\hat{f}$ means an estimate for f derived from the data. This notation will be used again for different estimates).

The problem with Equation 6.5 is that the errors e have been neglected. Error propagation typically gives very large errors for $\hat{f}$, even if e is small compared to d. An intuitive way to understand why this happens is to consider the nature of the matrix A. In most problems it is a smoothing matrix, which means that events in a certain x bin will be smeared out into several y bins, because of the limited resolution of the detector. High frequency components in f will be reduced by the smearing. This means that the inverse of A must amplify the high-frequency components in d. But these components are small, and impossible to measure because of the statistical errors, which are also a high-frequency component. Thus the errors receive a large weight from the direct inversion method.

To reduce statistical fluctuations, the solution needs to be regularised. This procedure is described in the next section.

6.2 Unfolding programs

6.2.1 Regularised unfolding using singular value decomposition (GURU)

The singular value decomposition (SVD) of a matrix A is the factorisation

$$A = USV^T \tag{6.6}$$

with $U^T = U^{-1}, V^T = V^{-1}$ and $S_{ij} = 0$ for $i \neq j, S_{ii} \geq 0$.

It is useful in many problems involving matrices, including unfolding.

GURU uses a least squares fit of the form

$$\sum_{j=1}^{m} \left(\frac{(\sum_{i=1}^{n} \hat{f}_i A_{ij}) - d_j}{\hat{e}_j} \right)^2 = \min \tag{6.7}$$

where $\hat{e}_j$ is the error on the jth measurement and $\hat{f}_i$ is the estimate of the true distribution[1]. The general case with correlated errors can be written in matrix form as

$$(Af - d)^T E^{-1} (Af - d) = \min \tag{6.8}$$

where E is the covariance matrix of the data d. The matrix E can be decomposed using SVD to rewrite this equation in a form that is easier to work with:

$$\begin{aligned} E &= Q^T R Q, \\ R_{jj'} = r_j^2 \text{ for } j' &= j, \qquad R_{jj'} = 0 \text{ for } j' \neq j \end{aligned} \tag{6.9}$$

Then, defining $A'_{ij} = \frac{1}{r_j} \sum_{j'=1}^{m} Q_{jj'} A_{ij'}$ and $d'_j = \frac{1}{r_j} \sum_{j'=1}^{m} Q_{jj'} d_{j'}$ leads to

$$(A'\hat{f} - d')^T (A'\hat{f} - d') = \min. \tag{6.10}$$

[1] In GURU, the unfolded distribution is actually the ratio of the Monte Carlo and data true distributions. This makes little practical difference to the procedure.

A regularisation term can now be introduced:

$$(A'\hat{f} - d')^T(A'\hat{f} - d') + \tau(C\hat{f})^T(C\hat{f}) = \min. \tag{6.11}$$

τ is the regularisation parameter as described in the previous section and C is a matrix giving the degree of curvature of $\hat{f}$.

In one dimension a possible definition of curvature is

$$r = \sum_i^n [(\hat{f}_{i+1} - \hat{f}_i) - (\hat{f}_i - \hat{f}_{i-1})]^2 \tag{6.12}$$

and the corresponding form of C is

$$C = \begin{pmatrix} -1 & 1 & 0 & 0 & \dots & \\ 1 & -2 & 1 & 0 & \dots & \\ 0 & 1 & -2 & 1 & \dots & \\ & \dots & & & & \\ & \dots & & 1 & -2 & 1 \\ & \dots & & & 1 & -1 \end{pmatrix}. \tag{6.13}$$

This is the default form of C in GURU. It is possible to change C, which allows the possibility of multi-dimensional unfolding.

The unfolding proceeds with the following stages:

1. The curvature matrix is made equal to the identity matrix by defining $\hat{f} \to C\hat{f}$ as the solution vector, and $A' \to A'C^{-1}$ as the response matrix.

2. The new response matrix is decomposed using SVD to give

$$A'C^{-1} = USV^T \tag{6.14}$$

with $S_{ij} = s_i$ for $i = j, S_{ij} = 0$ for $i \neq j$, and the rows are ordered so that s_i is a non-increasing vector.

3. The system is first solved for $\tau = 0$:

$$USV^T C\hat{f} = d'. \tag{6.15}$$

A rotated vector is defined:

$$\hat{f}_{rot} = V^T C\hat{f} \tag{6.16}$$

and the unregularised solution for $\hat{f}_{rot}$ is

$$\hat{f}_{rot,i} = \frac{(U^T d')_i}{s_i}. \tag{6.17}$$

4. The regularised solution can now be found by weighting the rotated solution;

$$\hat{f}_{rot,i} \rightarrow \hat{f}_{rot,i}\left(\frac{s_i^2}{s_i^2 + \tau}\right). \tag{6.18}$$

Weighting the rotated solution in this way is equivalent to introducing non-zero τ in Equation 6.11 [63].

5. Finally, the unrotated solution is found using

$$\hat{f} = C^{-1}V\hat{f}_{rot}. \tag{6.19}$$

The weighting procedure relates the regularisation parameter to the Number of Degrees of Freedom (NDF) by

$$\text{NDF} = \sum_i \left(\frac{s^2{}_i}{s^2{}_i + \tau}\right). \tag{6.20}$$

This is the sum of the weights applied to the rotated function.

An example of unfolding using GURU is shown in Figures 6.3 and 6.4. In this example, the number of degrees of freedom to be used is determined from the statistical significance of the values of d_i. Because of the way that the input covariance matrix E is transformed using SVD, the vector d_i has

a unit covariance matrix. For large enough values of i, d_i is expected to be consistent with zero. This can be seen in Figure 6.3c, where d_i falls exponentially to a constant of about 1. The GURU program uses statistical tests to find the number of significant values of d_i, which gives the number of degrees of freedom and hence τ from Equation 6.20.

6.2.2 Regularised unfolding using B-splines (RUN)

RUN is a regularised unfolding program by V. Blobel.

Distributions in RUN are parameterised as B-splines, rather than given as simple histograms. This means that the output is a continuous function which can be re-binned if desired.

It is easiest to begin by describing the unregularised solution. A maximum likelihood fit is performed to the function

$$S(\hat{f}) = -\sum_{j=1}^{m} \ln P(d_j|\hat{g}_j) \tag{6.21}$$

where $P(d_j|\hat{g}_j)$ is the initial probability of observing d_j events in the jth bin given an expectation of $\hat{g}_j = \sum_{i=1}^{m} A_{ij}\hat{f}_i$. It is given by the Poisson distribution, in which

$$P(A|B) = \frac{e^{-B}B^A}{A!}. \tag{6.22}$$

Disregarding constant terms which are irrelevant to the minimisation, Equation 6.21 becomes

$$S(\hat{f}) = -\sum_{j=1}^{m}(\hat{g}_j - d_j \log(\hat{g}_j)). \tag{6.23}$$

Assuming a quadratic form for S,

$$\Delta S(\hat{f}) = -(\Delta\hat{f})^T h + \frac{1}{2}(\Delta\hat{f})^T H(\Delta\hat{f}) \tag{6.24}$$

where ΔS= the change in S arising from change $\Delta\hat{f}$, and

$$h_i = -\frac{\mathrm{d}S}{\mathrm{d}\hat{f}_i} = -\sum_{j=1}^{m} A_{ij}\left(1 - \frac{d_j}{\hat{g}_j}\right), \text{ and} \tag{6.25}$$

$$H_{ik} = -\frac{\mathrm{d}^2 S}{\mathrm{d}\hat{f}_i \mathrm{d}\hat{f}_k} = -\sum_{j=1}^{m} \left(\frac{d_j A_{ij} A_{kj}}{\hat{g}_j^2} \right). \tag{6.26}$$

The minimum condition is $\Delta S = 0$. This suggests using $\Delta \hat{f} = H^{-1} h$ as an iteration step. Convergence is usually reached after a few iterations.

Without regularisation, the solution is identical to that obtained by direct inversion, with the same large fluctuations. To regularise the solution, a new term is added to the function to be minimised:

$$r(f) = \int [\hat{f}''(x)]^2 \, dx \tag{6.27}$$

where $\hat{f}''$ is the second derivative of $\hat{f}$. This term measures the smoothness of the solution. It is multiplied by a regularisation parameter τ. The new function to be minimised is

$$R(\hat{f}) = S(\hat{f}) + \tau r(\hat{f}). \tag{6.28}$$

If τ is zero, there is no regularisation. If τ is large, the solution will be biased towards a smooth solution. In discrete form, the second derivative $\hat{f}''(x)$ is found using a regularisation matrix C, which follows a similar principle to the GURU regularisation matrix, but has a different form due to the use of spline functions in RUN. In matrix form, the regularisation term is

$$r(\hat{f}) = \tau \hat{f}^T C \hat{f}. \tag{6.29}$$

A similar method to the one described above for the unregularised solution is used to solve the regularised system. Full details are in the RUN documentation.

6.2.3 Bayesian unfolding (BAYES)

Bayes' theorem can be stated as

$$P(\text{cause}|\text{effect}) \propto P(\text{effect}|\text{cause}) \times P_0(\text{cause}). \tag{6.30}$$

In the context of unfolding, a 'cause' is an event in a certain bin of the true distribution, and an 'effect' is a event in another bin of the measured distribution. The probabilities $P(\text{effect}|\text{cause})$ are equivalent to the response matrix in regularised unfolding. $P_0(\text{cause})$ is the initial probability of the cause, which can be estimated from Monte Carlo simulation. Although the output is independent of $P_0(\text{cause})$, if the initial estimate is far from the true distribution, the convergence is slower.

The normalised form of Bayes' theorem is

$$P(C_i|E_j) = \frac{P(E_j|C_i)P_0(C_i)}{\sum_{k=1}^{n} P(E_j|C_k)P_0(C_k)} \tag{6.31}$$

with the normalisation condition $\sum_{i=1}^{n} P(C_i|E_j) = 1$.

After N experimental observations one has a distribution of events, with the number of events in the jth bin $n(E_j)$. Events can then be assigned to causes, according to

$$n'(C_i) = \frac{1}{\epsilon_i} \sum_{j=1}^{m} n(E_j)P(C_i|E_j) \tag{6.32}$$

where E_i is the detector efficiency in the ith bin, obtained from Monte Carlo simulation. The total number of events is

$$N' = \sum_{i=1}^{n} n'(C_i). \tag{6.33}$$

And the updated probabilities are given by

$$P'(C_i) = \frac{n'(C_i)}{N'}. \tag{6.34}$$

The probabilities $P'(C_i)$ can then be put into Equation 6.31 as an improved guess, and the procedure repeated until some criterion is satisfied, for example, that χ^2 between two iterations is less than a certain value.

No smoothing is performed by the BAYES program, but it is recommended that the user smoothes the distribution before each iteration. This can be done, for example, with a fit to a simple function.

6.2.4 Comparison of unfolding programs

GURU and RUN are both regularised unfolding programs and are very similar in principle. They differ mostly in numerical implementation. RUN parameterises the distributions using spline functions, while GURU uses histograms. RUN performs a maximum likelihood fit while GURU uses a least squares fit. These factors are not very important for the result. What may have some influence are the different treatments of the response matrix and the regularisation. RUN uses a probability matrix, and regularises the actual unfolded distribution, while GURU uses a number-of-events matrix, and regularises the ratio of the Monte Carlo distribution and the unfolded distribution. This means that if the Monte Carlo distribution is reasonably close to the unfolded distribution, the regularisation in GURU will not bias the result as much as RUN.

The most important difference from the point of view of the user is the design philosophy. GURU is intended to be simple and transparent. The user fills the arrays directly, and can modify the code, for example, changing the curvature matrix for different treatment of the endpoints or multidimensional unfolding. RUN works more as a black box. It has more adjustable parameters than GURU; a necessity because it is not easy to change the code directly. This makes RUN easier to use than GURU, but harder to understand.

The BAYES unfolding program works in a rather different way to the other two programs. Without regularisation it is equivalent to them (there is only one exact solution to the problem) but unlike RUN and GURU it will not do any regularisation itself; this is left to the user. While there are some advantages to this approach, such as the ability to fit to any desired function while unfolding, it is impossible to balance smoothness against bias through the use of a regularisation parameter. Also, as the smoothing is not an integral part of the unfolding process, the errors cannot take it into

account.

Error calculation is a problem with the BAYES program. Figure 6.2a shows a test of unfolding with GURU, RUN and BAYES. GURU and RUN give results consistent with the input distribution, while BAYES does not. It is not simply that the errors from BAYES are too small. It is possible to reduce the errors from GURU and RUN by reducing the number of degrees of freedom, but this has no effect on the size of the errors from BAYES (Figure 6.2b).

A related problem with BAYES is that if smoothing is not performed, the convergence is very slow, and while the oscillations become as large as in any unregularised method, the errors given by the program remain small. In contrast, RUN and SVD give errors consistent with the size of the statistical fluctuations, whatever the value of τ.

On the other hand, the errors from BAYES include the statistical errors on the response matrix, which is neglected in GURU and RUN. This makes it safe to use BAYES if the Monte Carlo statistics are limited. The main advantage of the BAYES program is that it can be used for two dimensional unfolding with no alterations, although then it is necessary to smooth in two dimensions also.

6.3 Two-dimensional unfolding using GURU

The two-dimensional (2D) unfolding problem differs from the one-dimensional case only in the regularisation matrix. This is because an unregularised method does not depend on which bin is adjacent to which, so 2D unfolding can be performed just by placing all of the bins in a single 1D vector, as shown in Figure 6.1.

However, for regularisation, the curvature matrix needs to contain information about adjacent bins. The 2D curvature matrix is actually very similar

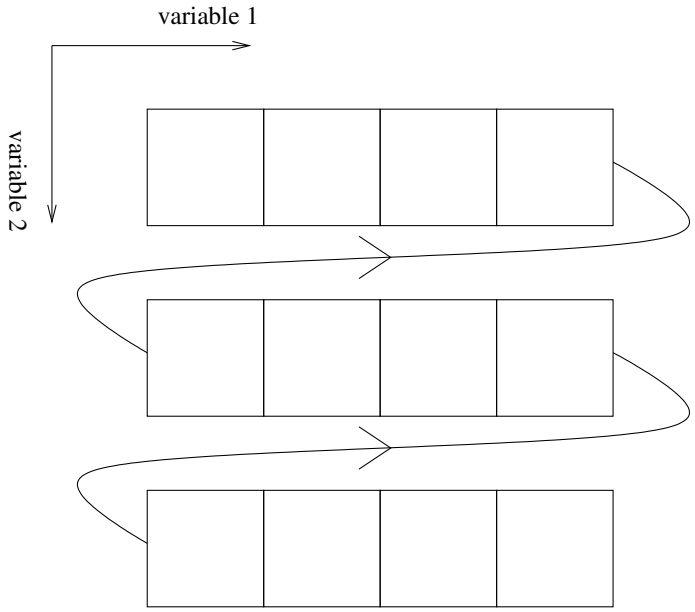

Figure 6.1: Two-dimensional unfolding can be reduced to one-dimensional unfolding.

to the 1D case. It is simply necessary to remove the smoothing between the end of one row and the beginning of the next.

The result of 2D unfolding is a distribution in two variables. To find the distribution in just the first variable, all of the columns are added together. For the errors, entries in the 2D covariance matrix are added together according to the usual rules of statistics.

$$\sigma^2_{A+B} = \sigma^2_A + \sigma^2_B + 2\mathrm{cov}(A,B) \quad (6.35)$$

$$\mathrm{cov}(A+B,C) = \mathrm{cov}(A,C) + \mathrm{cov}(B,C). \quad (6.36)$$

6.4 Unfolding F_2^γ

The methods described so far unfold the number of events in each bin of the distribution. From this we need to obtain a measurement of F_2^γ. At any value of x, the expected number of events is proportional to the structure function, therefore the measured structure function is

$$F^\gamma_{2,\mathrm{measured}}(x) = \frac{F^\gamma_{2,\mathrm{MC}}(x) f(x)}{f_{MC}(x)}. \tag{6.37}$$

The function $f(x)$ can be obtained from a spline fit to the unfolded points. $f_{MC}(x)$ is the corresponding distribution in the Monte Carlo sample and $F^\gamma_{2,\mathrm{MC}}(x)$ is the input structure function of the Monte Carlo sample. The final measurement is actually an average over each bin. One possibility is to calculate the simple average over x:

$$\langle F^\gamma_{2,\mathrm{measured}} \rangle_x = \langle \frac{F^\gamma_{2,\mathrm{MC}}(x) f(x)}{f_{MC}(x)} \rangle. \tag{6.38}$$

But $f(x)$ and $f_{MC}(x)$ have approximately the same shape, and in any case $f(x)$ is fitted to only one point in each bin. Therefore it makes sense to replace $f(x)/f_{MC}(x)$ with $\langle f(x) \rangle / \langle f_{MC}(x) \rangle$, which is no longer a function of x and is just the ratio of the bin contents, i.e.

$$\langle F^\gamma_{2,\mathrm{measured}} \rangle_x = \langle F^\gamma_{2,\mathrm{MC}}(x) \rangle \frac{f_i}{f_{MC,i}}. \tag{6.39}$$

However, the error is *not*

$$\langle F^\gamma_{2,\mathrm{measured}} \rangle_x = \langle F^\gamma_{2,\mathrm{MC}}(x) \rangle \frac{e_i}{f_{MC,i}}. \tag{6.40}$$

unless the function $f(x)$ is nearly flat across the bin, and if $f(x)$ falls to zero, as it does in the lowest x bin, the relative error can become very large. It would be necessary to evaluate $e(x)$ to find the error, as the unfolding programs only give e_i. This means that this form of the average is not very

useful for low-x measurements. An alternative is the average over the events in the bin. This is given by

$$\langle F^{\gamma}_{2,\mathrm{measured}} \rangle_x = \langle \frac{F^{\gamma}_{2,\mathrm{MC}}(x) f^2(x)}{f_{MC}(x)} \rangle \langle \frac{1}{f(x)} \rangle. \tag{6.41}$$

This reduces in the same way as the first formula, to

$$\langle F^{\gamma}_{2,\mathrm{measured}} \rangle_x = \frac{\langle F^{\gamma}_{2,\mathrm{MC}}(x) f(x) \rangle}{f_{MC,i}}. \tag{6.42}$$

Now the error (neglecting the error on the weighting function, which has little effect) is

$$\begin{aligned} \sigma &= \langle \frac{F^{\gamma}_{2,\mathrm{MC}}(x) e(x) f(x)}{f_{MC}(x)} \rangle \frac{1}{f_i} \\ &= \frac{\langle F^{\gamma}_{2,\mathrm{MC}}(x) e(x) \rangle}{f_{MC,i}}. \end{aligned} \tag{6.43}$$

But $F^{\gamma}_{2,\mathrm{MC}}$ can be treated as a constant for the purposes of the error, so

$$\sigma = \frac{\langle F^{\gamma}_{2,\mathrm{MC}}(x) \rangle e_i}{f_{MC,i}}. \tag{6.44}$$

Thus the error can be found from e_i, with no need to calculate $e(x)$.

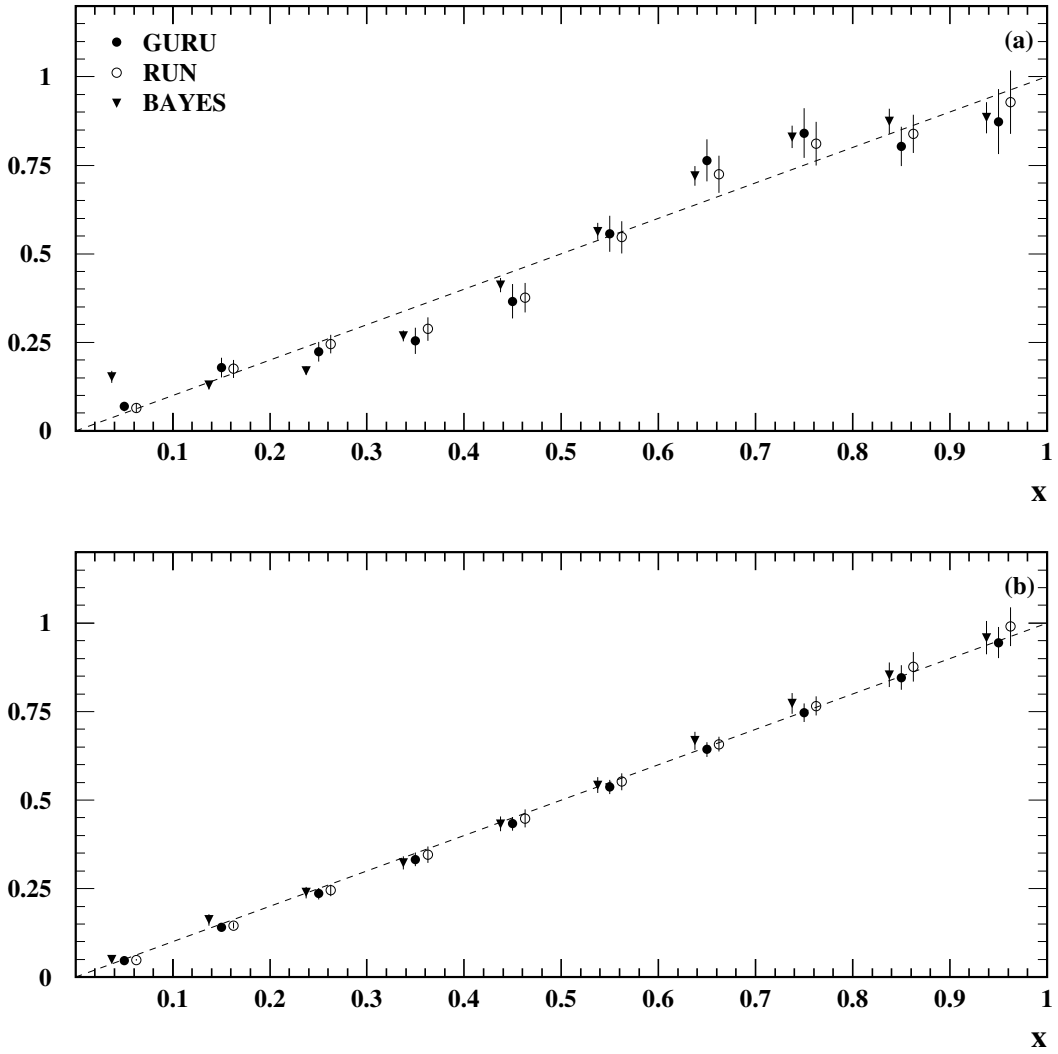

Figure 6.2: A test of the unfolding programs RUN, GURU and BAYES. The same true and measured distributions were used for all three programs, including the effects of statistics and smearing of the measured distributions. The number of degrees of freedom were (a) four, and (b) two. The dashed line indicates the input true distribution.

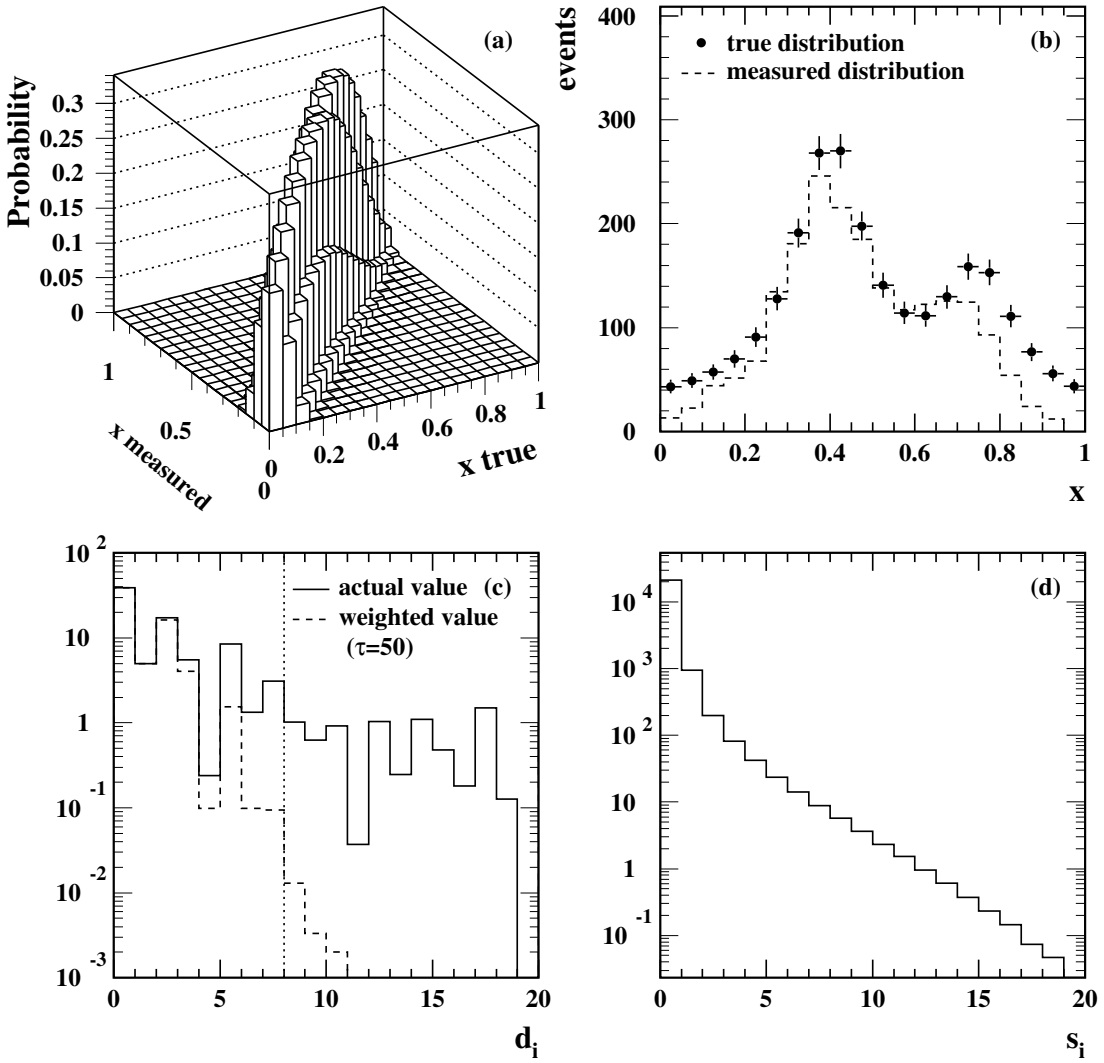

Figure 6.3: An example of unfolding using GURU (originally from the RUN program) (a) The response matrix, (b) the true and smeared distributions, (c) the values of d_i, compared to the regularised values. (the dotted line indicates the point above which the values of d_i become consistent with zero), (d) the values of s_i.

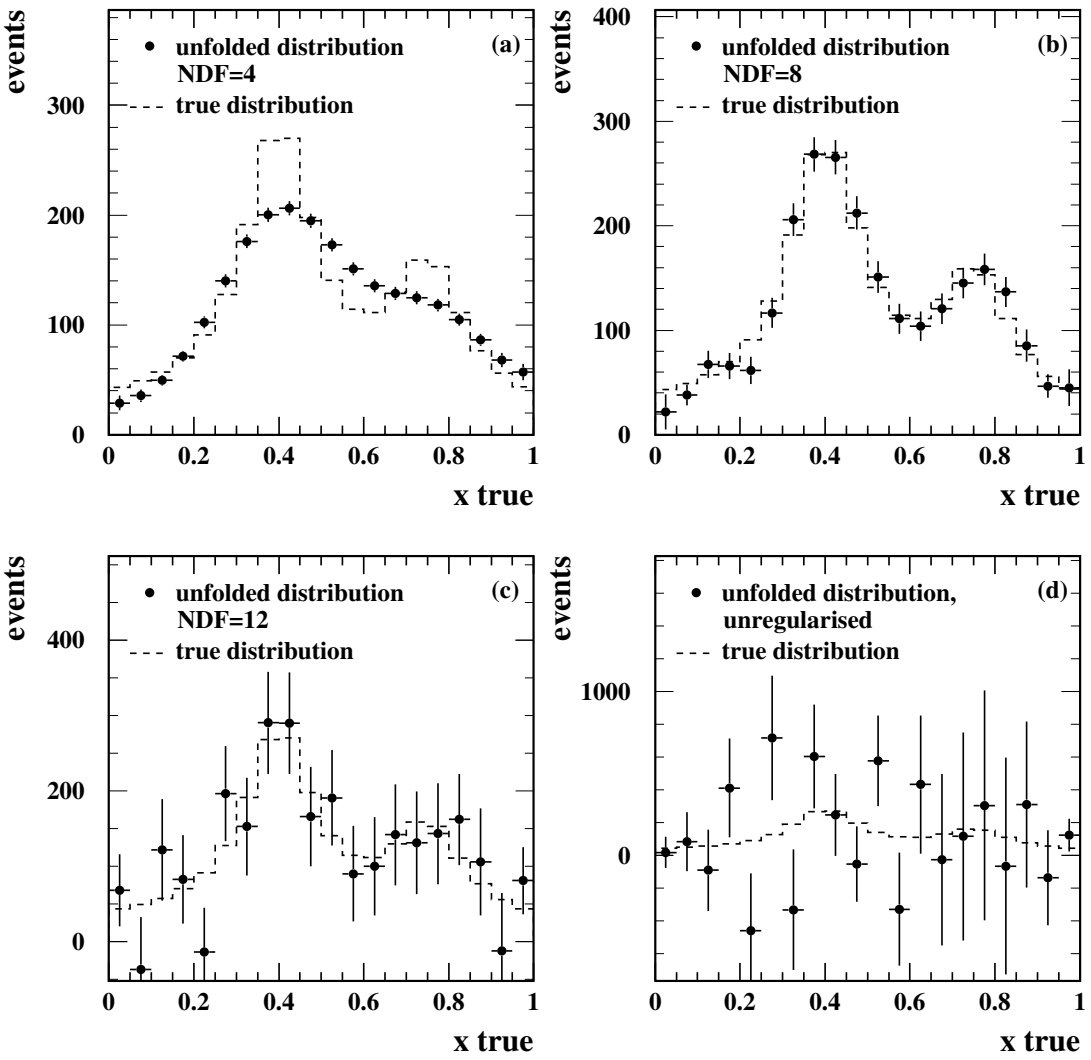

Figure 6.4: The results of unfolding the distributions shown in Figure 6.3 with various numbers of degrees of freedom. The true distribution is the same in each case. (a) NDF=4, (b) NDF=8 (recommended by GURU), (c) NDF=12, (d) unregularised.

Chapter 7

Measurement of F_2^γ

7.1 Correction for detector effects

The technique of unfolding, described in Chapter 6, is needed to correct for detector effects when measuring F_2^γ. GURU is used as the main unfolding program rather than RUN or BAYES, so that two-dimensional, regularised unfolding can be performed.

Some parameters need to be chosen before unfolding:

- The binning of the true variable(s),
- The binning of the measured variable(s) and
- The regularisation parameter, τ.

As the main goal of the analysis is to measure the structure function at low x, the binning is optimised for the low-x data. Equal-sized bins in $\log(x)$ were chosen because this gives more resolution at low x than a linear scale would. The lower and upper limits for x were chosen so that all accepted Monte Carlo events fitted within the range, without leaving empty regions that could lead to under-populated bins. The measured variable limits were

set in the same way, with equal-sized bins on a log scale. The bin limits for both true and measured variables are different for each data sample, due to the different kinematic ranges.

The regularisation parameter is set according to the effective number of degrees of freedom, which is estimated by GURU as described in Section 6.2.1.

7.2 Reconstruction of W

The true variable to be unfolded is the DIS variable x, but there is some freedom in the choice of the measured variable. Equation 3.5 suggests

$$x_{\rm vis} = \frac{Q^2}{Q^2 + W^2_{\rm vis}} \tag{7.1}$$

where $W_{\rm vis}$ is the observed invariant mass of the final hadronic state, evaluated by summing over all tracks and calorimeter clusters, and including objects from the forward region of the detector (SW and FD). Hadronic energy is not well measured by the electromagnetic calorimeters in the forward region, and some energy is lost in the beam pipe. At higher W, a higher proportion of energy is deposited in the forward region. Unfolding corrects the energy losses using Monte Carlo events. But the distribution of hadronic energy in the final state is dependent on the Monte Carlo model. This is potentially a large source of systematic error.

It would be preferable not to rely so heavily on Monte Carlo simulation, and instead use more information from the data to provide a better measurement of x.

It is possible to improve the reconstruction of W by including kinematic information from the tagged electron [64]. $W^2_{\rm vis}$ is defined by

$$W^2_{\rm vis} = (\sum_i E_i)^2 - (\sum_i p_{i,x})^2 - (\sum_i p_{i,y})^2 - (\sum_i p_{i,z})^2 \tag{7.2}$$

where i runs over all tracks and clusters in the hadronic final state, with energy E_i and momentum vector $(p_{i,x}, p_{i,y}, p_{i,z})$. This can also be written as

$$W^2_{\rm vis} = (\sum_i p_{i+})(\sum_i p_{i-}) - (p_{i,\rm t})^2 \tag{7.3}$$

where $p_{i\pm} = E_i \pm p_{i,z}$ and $p_{i,\rm t} = \sqrt{{p_{i,x}}^2 + {p_{i,y}}^2}$. Using conservation of energy and momentum, and assuming that the untagged electron travels along the beam direction, p_+ and p_t can be replaced by variables related to the tagged electron, leading to

$$W^2_{\rm rec} = (p_{\rm beam+} - p_{\rm tag+})(\sum_i p_{i-}) - (p_{\rm tag,t})^2 \tag{7.4}$$

where $p_{\rm beam+}$ and $p_{\rm tag+}$ are calculated for the tagged electron before and after scattering, respectively, and $p_{\rm tag,t}$ is calculated according to the definition of $p_{i,\rm t}$, above, for the tagged electron. When using Equation 7.4 instead of Equation 7.3 to evaluate the measured W of each event, the hadronic energy resolution enters only through the p_{i-} term. This is an advantage because the leptonic energy resolution is usually better than the hadronic energy resolution. The (reconstructed) variable formed in this way is called $W_{\rm rec}$ and the corresponding measurement of x is called $x_{\rm rec}$.

Even after the above technique has been applied, the value of $W_{\rm rec}$ is still generally smaller than the true value of W. This is mainly due to energy losses in the forward region of the detector; only about half of the hadronic energy deposited in that region is observed. In an attempt to make the energy response of the detector more uniform and to reduce the systematic error due to the uncertainty in the Monte Carlo modelling, a new (corrected) variable is formed: $W_{\rm cor}$ (with the corresponding x measurement $x_{\rm cor}$), in which the contribution of energy from the forward region is increased by a factor of 2.5. This factor was obtained by comparing the generated and measured energy in the forward region in Monte Carlo events.

$$W^2_{\rm cor} = (p_{\rm beam+} - p_{\rm tag+})(\sum_i p'_{i-}) - (p_{\rm tag,t})^2 \tag{7.5}$$

$$p'_{i-} = \begin{cases} 2.5p_{i-} & \text{For particles in SW or FD} \\ p_{i-} & \text{otherwise.} \end{cases}$$

Figure 7.1a shows the correlation of W and the three measured quantities $W_{\rm vis}$, $W_{\rm rec}$ and $W_{\rm cor}$ for the LEP2 SW sample generated with HERWIG 5.9+$k_{\rm t}$(dyn). The spread of $W_{\rm cor}$ in W is larger than that of the other two variables, because in $W_{\rm cor}$ more weight is given to the forward region, where the energy resolution is worse than in the central region. The larger spread could lead to slightly larger statistical errors in the unfolding. However, if the systematic error is significantly reduced by the use of $W_{\rm cor}$, the total error may be lower. Figure 7.1b shows the correlation between the generated energy in the forward region and the scaled observed energy in that region, $E_{\rm cor}$.

The improvement when using $W_{\rm cor}$ or $W_{\rm rec}$ compared to $W_{\rm vis}$ is largest when the most energy is deposited in regions where the measurement is poor. It is therefore both detector and model dependent.

7.3 Two-dimensional unfolding

The GURU program can be modified to perform unfolding in two dimensions as described in Section 6.3. As with the W reconstruction methods described above, the motivation is to reduce the dependence of the unfolding on a particular Monte Carlo model. There is information in every event about the angular distribution of energy in the detector, but it is lost if only x is used in the unfolding procedure. Including another variable in a second unfolding dimension allows the unfolding program to make use of this information. Two-dimensional unfolding of F_2^γ has previously been found to give lower systematic errors than one-dimensional unfolding [65].

Two variables were considered as possible second unfolding variables:

- $E_{\rm T}^{\rm out}/E_{\rm total}$, the transverse hadronic energy out of the plane containing

the beam line and the tagged electron (Equation 4.3), divided by the total observed energy, and

- $E_{\rm for}/E_{\rm total}$, the observed energy in the forward region divided by the total observed energy.

These variables are shown in Figures 7.3, 7.4 and 7.5. They were chosen because they are very sensitive to the angular distribution of the hadrons in the final state. Dividing them by the total observed energy serves two purposes: it normalises them on a scale of zero to one, which is useful for binning, and it reduces their correlation with x, leading to more evenly populated bins.

7.4 Unfolding tests

Varying the number of degrees of freedom affects the amount of smoothing between the unfolded points. Figure 7.2a shows the same sample unfolded using three different NDF values. As expected, a lower value of NDF decreases the errors while increasing the correlations. The value of NDF used for the final results is the one recommended by GURU, in this case, three.

The results using the three unfolding programs GURU, RUN and BAYES were compared. The results for one sample are shown in Figure 7.2b. The three programs give generally consistent results, though the errors given by BAYES tend to be smaller than those given by the other two programs.

To test the two-dimensional (2D) unfolding procedure, a random number was used as the second variable. This is shown in Figure 7.2c. The results are consistent with one-dimensional (1D) unfolding, which is as expected since there is no extra information in a random number. The number of degrees of freedom in 2D unfolding needs to be larger to allow for the extra variable, and was chosen according to the recommendation of the unfolding program from statistical analysis of the data. The statistical errors are comparable to those given by 1D unfolding.

The results when using various different unfolding variables ($x_{\rm vis}$, $x_{\rm rec}$ and $x_{\rm cor}$) are compared in Figure 7.2d. The difference between them is about the size of the statistical error.

7.5 Comparison of unfolding methods

To find which of the unfolding variables were the most useful, OPAL data was unfolded with four Monte Carlo programs HERWIG 5.9, HERWIG 5.9+$k_{\rm t}$(dyn) PHOJET 1.05 and F2GEN. Despite not giving good descriptions of the data, HERWIG 5.9 and F2GEN were included in this study to investigate the effectiveness of the new techniques using extreme models. The best methods are considered to be those which give the smallest difference between the unfolded results with the four Monte Carlo models. The quantity compared is ${\chi^2}_{\rm models}$, defined by

$$ {\chi^2}_{\rm models} = \frac{1}{4} \sum_{\rm models} \sum_i \left(\frac{F_{2\,i}^\gamma - \langle F_{2\,i}^\gamma \rangle}{\sigma_i} \right)^2 \qquad (7.6) $$

where $F_{2\,i}^\gamma$ is the value of the unfolded result in the ith bin, $\langle F_{2\,i}^\gamma \rangle$ is the average of the results from all four Monte Carlo models and σ_i is the statistical error for the ith bin. The values of ${\chi^2}_{\rm models}$ are shown in Table 7.1 and the results of the unfolding are shown in Figures 7.6 and 7.7. The ${\chi^2}_{\rm models}$ values show how large the differences between the models are, compared to the statistical error. Due to the different statistics in each sample, the numbers can only be compared meaningfully for different unfolding methods for the same data sample. For the 1D unfolding, using $x_{\rm cor}$ as the measured variable gives the lowest ${\chi^2}_{\rm models}$ in all samples. Using $x_{\rm rec}$ as the unfolding variable gives only a small improvement over unfolding with $x_{\rm vis}$. For the 2D unfolding, $E_{\rm T}^{\rm out}/E_{\rm total}$ is the best second variable overall, and using $x_{\rm cor}$ instead of $x_{\rm rec}$ generally gives some improvement, though not as much as in the 1D case. The χ^2 values are smaller for the LEP1 FD sample than the other two,

partly due to the the smaller number of bins. Also the LEP1 FD sample has the lowest statistics, which means that any difference between the Monte Carlo programs would be less significant. For the 1D unfolding results using

		χ^2_{models}					
		1D		2D, $E_{\text{T}}^{\text{out}}/E_{\text{total}}$		2D, $E_{\text{for}}/E_{\text{total}}$	
$\langle Q^2 \rangle$ [GeV^2]	sample	x_{vis}	x_{cor}	x_{rec}	x_{cor}	x_{rec}	x_{cor}
1.9	LEP1 SW	66.8	29.1	22.1	9.6	24.7	26.9
3.7		53.1	26.1	13.5	8.1	19.5	16.8
8.9	LEP1 FD	15.4	6.8	7.1	3.4	10.7	8.7
17.5		8.5	4.5	8.8	12.4	4	4.1
10.7	LEP2 SW	62.5	22.4	18.7	6.8	20.6	16.8
17.8		57.2	18.3	13	8.4	57.7	15.4

Table 7.1: χ^2_{models}, as defined in Equation 7.6, for different unfolding methods. The number of bins in x was 4 for the LEP1 SW and LEP2 SW samples, and 3 for the LEP1 FD samples.

x_{vis} as the unfolding variable, the HERWIG 5.9 sample tends to give higher unfolded points at low x than the other three Monte Carlo samples, and unfolding with the F2GEN sample gives the lowest result at low x. With both 2D unfolding and 1D unfolding using x_{cor}, the results using HERWIG 5.9 and F2GEN became closer to the other two. Using different unfolding methods with the HERWIG 5.9+k_{t}(dyn) and PHOJET 1.05 samples makes less difference than with the other two Monte Carlo samples, which is as expected for models which give a better description of the data.

Overall, the best unfolding method was 2D unfolding, with $E_{\text{T}}^{\text{out}}/E_{\text{total}}$ as the second variable, which is consequently used as the standard unfolding method for the results.

As a final test of the method, samples of events generated using HERWIG 5.9 with the SaS1D structure function were unfolded using HERWIG 5.9 with the GRV structure function (Figure 7.13). The results agree with the input

structure function, within the statistical errors.

7.6 Bin-centre corrections

For convenience in making fits to the data, the measured points are corrected to represent F_2^γ at a specific value of x, rather than the average F_2^γ over each bin. The x value chosen is the log centre of each bin, except for the highest x bins where this would be close to the charm threshold, which could lead to large errors due to uncertainty in the charm mass. In those bins, F_2^γ is corrected to the log centre of the portion of the bin below the charm threshold for $m_c = 1.5$.

The corrections are calculated as the average of the corrections obtained using the GRV and SaS1D structure functions, and are given in Table 7.5.

7.7 Systematic errors

The systematic error should include all uncertain factors that could significantly bias the result. It is estimated by varying different aspects of the analysis one at a time while keeping everything else the same, finding the difference in the result, and adding all of the differences in quadrature. In general, the systematic errors may be asymmetric. For this reason, positive and negative errors are added separately.

To avoid overestimating the systematic errors, it is important not to introduce additional statistical errors. For example, changing the event selection may remove a significant portion of events in one x bin, which can lead to a change in the result for purely statistical reasons. This is a particular problem when a number of systematic effects have to be combined, because they all contain a statistical component, so the size of the total error would depend on the number of separate systematic checks, which can be made arbitrarily

large. To study the effect of statistical fluctuations on the size of the systematic errors, Monte Carlo is used as mock data. The statistical components are then subtracted from the errors. This is described in Section 7.7.13.

Because the Monte Carlo samples used for unfolding are only 3–6 times the size of the data sample, sometimes there are unfolding instabilities due to limited Monte Carlo statistics. This is more likely to happen when bins are under-populated. To avoid this, the bin boundaries of the true and measured variables are carefully positioned so that there are no empty or nearly empty bins at the edges of the ranges.

Another possible problem when changing the event selection is that the average Q^2 of the sample may be shifted. As the structure function evolves with Q^2, the result will change due to this alone, quite apart from any systematic effect. However, for most changes the Q^2 shift is small.

The possible sources of systematic errors that have been considered and the means of estimating them are explained in the following sections.

7.7.1 Monte Carlo modelling

The angular distribution of the hadrons in the final state is not well understood and not well measured outside the central region of the detector. Therefore, a selection of Monte Carlo models must be considered. It was demonstrated in Chapter 5 that the default version of HERWIG 5.9 and F2GEN are not in agreement with the data even in the central region, so the models used to estimate the systematic error are HERWIG 5.9+k_t(dyn) and PHOJET 1.05, which give a better description of the data. While previous studies [14, 13] did use HERWIG and F2GEN, they were made before the other Monte Carlo programs became available.

There is no compelling reason to prefer one over the other, so the central value for F_2^γ is taken as the average of the unfolding results with HERWIG 5.9 +k_t(dyn) and PHOJET 1.05, and the systematic modelling error is taken

to be plus or minus half the difference.

7.7.2 Choice of second variable

Two second variables were considered: $E_{\mathrm{T}}^{\mathrm{out}}/E_{\mathrm{total}}$ and $E_{\mathrm{for}}/E_{\mathrm{total}}$. The central value is the result with $E_{\mathrm{T}}^{\mathrm{out}}/E_{\mathrm{total}}$, and the difference when using $E_{\mathrm{for}}/E_{\mathrm{total}}$ is considered as a systematic error.

7.7.3 Unfolding parameters

The number of bins used for the measured x distribution is independent of the true-x binning, and was varied from the same as the number of bins in the true variable, to twice as many. The standard value is 6 bins, compared to 4 bins in the true variable.

7.7.4 W reconstruction

The amount of extra weight to be given to the forward energy is not precisely determined because of the poor energy measurement in this region. Any systematic effect due to this ought to be smaller than the modelling error, which the forward energy treatment is intended to reduce.

To investigate the systematic effect of the W reconstruction procedure, the weighting of E_{for} was varied from 2.0–3.0. The value was changed at the same time in both data and Monte Carlo.

7.7.5 Cut variations

Various systematic effects can be studied by changing the cuts. These include the effect of background contamination near the cut boundaries, poor reconstruction of event quantities and uncertainties in the acceptance. Generally the cuts are varied by an amount at least as much as the resolution of

cut	LEP1 SW	LEP1 FD	LEP2 SW
$E_{\rm tag}/E_{\rm b}$ min	$\pm$0.025 (0.75)		$\pm$0.025 (0.775)
$\theta_{\rm tag}$ min [mrad]	+2 (27)	+2 (60)	+2 (33.25)
$\theta_{\rm tag}$ max [mrad]	$-$2 (55)	$-$2 (120)	$-$2 (55)
$E_{\rm a}/E_{\rm b}$ max	$\pm$0.05 (0.25)		
$W_{\rm vis}$ min [GeV]	+1.0 (2.5)		
$W_{\rm vis}$ max [GeV]	$\pm$5 (40)		$\pm$5 (60)

Table 7.2: Systematic variations in the cuts. The standard cuts are given in brackets after the variations.

the variable to which the cut is applied, on the principle that it is impossible to determine the best position for the cut to a greater precision than this.

Because the event selection is changed when a cut is varied, there will be some difference due to statistics. It is important to keep this to a minimum by not moving the cut more than necessary.

The cut variations are listed in Table 7.2 and described in the following sections.

- $E_{\rm tag}$

  The minimum $E_{\rm tag}$ cut is varied to study the effect of off-momentum background contamination. Care is required when varying this cut, however, because low $E_{\rm tag}$ events are concentrated at low x. Moving the cut too much would introduce statistical fluctuations in the lowest x bin. Consequently, this cut is varied only by the resolution of $E_{\rm tag}$, which is about 4%, in both directions.

- $\theta_{\rm tag}$

  Changing the $\theta_{\rm tag}$ cuts varies the acceptance region and allows for the possibility that reconstruction of position and energy of particles is not perfect at the edges of the detectors. $\theta_{\rm tag}$ is more correlated with Q^2

than any other variable with a cut, so this variation could affect the average Q^2. However, there is no need for the variation to be so large as the resolution of $\theta_{\rm tag}$ is very good. The cuts are varied only inwards, away from the edges of the detector, because the whole region of good acceptance is already used when finding the central value.

- $N_{\rm ch}$

  The minimum number of charged tracks can only be changed by a whole integer, but raising it by a single unit already removes too many events - around one quarter of the total sample, and these events are concentrated in the high x region. This means that systematic uncertainties in the track reconstruction procedure cannot be studied by varying the minimum number of charged tracks, Instead, the tracking parameters in the Monte Carlo simulation are studied (see Section 7.7.8).

- $W_{\rm vis}$

  The high-W region is the least well modelled by the Monte Carlo programs, and background from hadronic $\rm Z^0$ decays is significant in the 91 GeV data, and also present in the 189 GeV data. To investigate systematic effects in this region, the maximum $W_{\rm vis}$ cut is varied. Too loose a cut will let through more background events than necessary. Too tight a cut risks affecting the low-x acceptance in a model dependent way, because the number of events removed by the cut will depend on the final state modelling. Also, a low maximum $W_{\rm vis}$ cut will deplete the lowest x bin, causing statistical fluctuations.

  There is also a cut on low $W_{\rm vis}$. This is because of low-mass effects such as resonances which are not accurately simulated in the Monte Carlo programs. The minimum is raised by 1 GeV as a systematic check.

- $E_{\rm a}$

Since real double-tagged events have a low cross-section, the highest energy particle opposite the tag usually comes from the hadronic final state. Therefore, the anti-tag distribution in Monte Carlo depends on the final state model. HERWIG, PHOJET and F2GEN differ in the shape of the anti-tag distribution. Setting the cut too low will remove mostly events with high W, because those events are more likely to have an energetic particle. Setting the cut too high will leave some events with a scattered beam electron in the final state. To study these effects the anti-tag cut is varied.

It would make little sense to move the anti-tag cut higher than 30% of the beam energy, as above that point the double-tagged events dominate. On the other hand, moving the cut below 20% of the beam energy eliminates very few extra double-tagged events while depleting the low x bin considerably. The range of variation of the cut is from 20% to 30%.

7.7.6 Off-momentum electrons

There are signs of some contamination from off-momentum background in the 184 GeV data. It is apparent in one ϕ region only, at low $E_{\rm tag}$. The region in question is cut out of the main analysis, but included as one of the systematic checks.

7.7.7 Calibration of the tagging detectors

The energy of the tagged electron in the Monte Carlo was varied to allow for uncertainty in the calibration of the tagging detectors. The variation was $\pm 1\%$, motivated by a comparison of the data and Monte Carlo $E_{\rm tag}$ distributions.

As this only affects Monte Carlo, and not data, it should not introduce large statistical fluctuations.

7.7.8 Measurement of hadronic energy

To allow for uncertainty in the simulation of the detector, the energy scale of the electromagnetic calorimeters is varied by $\pm 3\%$. This does not include the forward region, which is dealt with separately.

The different $N_{\rm ch}$ distributions in data and Monte Carlo indicate that it may be necessary to systematically vary the tracking parameters. The variations are listed in Table 7.3. The parameters were varied all at the same time, to a set of tighter cuts and a set of looser cuts. The effect of these variations on the observed number of tracks is shown in Figure 7.12. The change in the $N_{\rm ch}$ distribution with these variations is of comparable size to the difference between the data and Monte Carlo $N_{\rm ch}$ distributions. Changing the tracking parameters in data and Monte Carlo at the same time produces effects that very nearly cancel. Smearing the tracking resolution in Monte Carlo only also had a very small effect on the result. Therfore, the systematic error from variation of the tracking parameters is taken to be negligible.

parameter	standard	tight	loose
CJ hits	20	25	15
d_0 max [cm]	2.5	2.0	3.0
z_0 max [cm]	30	20	50
$p_{\rm t}$ min [GeV]	0.125	0.15	0.1

Table 7.3: Variation of quality requirements for tracks.

7.7.9 Simulation of background

The largest background source, from τ pair production in two-photon events, is purely QED and well modelled. The largest uncertainty in the background modelling comes from the hadronic events at LEP1, which involve the production of light mesons with a high fraction of the beam energy. The cross-section for these events was measured by OPAL [66] with an accuracy of about 50%, and found to be consistent with the JETSET prediction. The normalisation of the simulated background was therefore varied by $\pm 50\%$.

7.7.10 Bin-centre correction

The corrections depend on the shape of F_2^γ in each bin. The average of the corrections based on GRV LO and SaS1D was used, as these parameterisations are the closest to the data. The error is half the difference between the GRV LO and SaS1D corrections, and is symmetric.

7.7.11 MC structure function

Simply changing the x distribution of the Monte Carlo sample should have no systematic effect on the unfolding result. However, if the structure function is used by the Monte Carlo program in other ways than for setting the x distribution, there will be a dependence on the parameterisation of F_2^γ used when generating the events.

This was studied by generating an additional Monte Carlo sample using HERWIG with the SaS1D parameterisation, unfolding the data with that sample, and comparing the results to those from HERWIG with the GRV parameterisation.

The two samples give consistent results, within statistical errors. This suggests that there is no systematic effect from using different structure functions in HERWIG.

7.7.12 Other systematic errors

The lower estimates for the trigger efficiencies are close to 100% (see Section 5.5), with a 1% systematic error. No correction to the results is made for the trigger efficiency, but the 1% error is included. The variation of the trigger efficiency with x is small and therefore neglected.

The uncertainty in the luminosity measurement gives a small overall normalisation error, which is neglected.

7.7.13 Estimation of the statistical component of the systematic errors

Checking a systematic effect by unfolding the data with one parameter or cut varied will lead to a result different from the central value. Some of the difference may be systematic, but some will be statistical. It is important to have an idea of how large the statistical component is, in order to avoid including statistical effects in the systematic errors.

The statistical effect of changing a cut will be less than the full statistical error, because only a subset of events are affected by the change. In principle the statistical errors on the systematic errors could be calculated, but in practise it is easier to repeat the unfolding several times with different data samples and take the spread of the different results. There is not enough real data to do this, so Monte Carlo events are used instead. The statistical errors on a Monte Carlo sample the same size as the data ought to be about the same as the statistical errors on the data itself.

The change in the result in bin i when changing parameter or cut k is $\Delta f_{i,k}$. The error on this value (found from Monte Carlo) is $\sigma_{\Delta f,i,k}$. The total systematic error, resulting from adding all of the individual errors in

quadrature, is

$$\Delta f_{i+} = \sqrt{\sum_{k:\Delta f_{i,k}>0} (\Delta f_{i,k})^2}$$
$$\Delta f_{i-} = \sqrt{\sum_{k:\Delta f_{i,k}<0} (\Delta f_{i,k})^2}. \quad (7.7)$$

However, many of the individual errors are not statistically significant, and should not be included in the total error. A better estimate of the real systematic error is given by

$$\begin{aligned} \Delta f_{i+} &= \sqrt{\sum_{k:\Delta' f_{i,k}>0} (\Delta' f_{i,k})^2} \\ \Delta f_{i-} &= \sqrt{\sum_{k:\Delta' f_{i,k}<0} (\Delta' f_{i,k})^2} \quad (7.8) \\ (\Delta' f_{i,k})^2 &= (\Delta f_{i,k})^2 - \sigma^2_{\Delta f,i,k} \text{ for } \Delta f_{i,k} > \sigma_{\Delta f,i,k} \\ \Delta' f_{i,k} &= 0 \text{ for } \Delta f_{i,k} < \sigma_{\Delta f,i,k} \end{aligned}$$

7.8 Results

The photon structure function F_2^γ is measured by unfolding each data sample in bins of $\log(x)$. The results are listed in Table 7.4. The quoted values were measured as the average F_2^γ/α in each bin of x weighted by the unfolded x distribution, according to Equation 6.42, then corrected to the log centre of each bin, except for the highest x bins where the log centre of that portion of the bin below the charm threshold for $m_c = 1.5$ GeV was used. The bin-centre corrections are the average of the GRV LO and SaS1D predictions for the correction from the average F_2^γ over the bin to the value of F_2^γ at the nominal x position.

The results are corrected for radiative effects. The radiative corrections were calculated using the RADEG [49] program and are listed in Table 7.5. The statistical correlations between bins are shown in Table 7.6. Each OPAL

data sample is divided into two ranges of Q^2 containing approximately equal numbers of events. The ranges correspond to to $\langle Q^2 \rangle$ values of 1.9 and 3.8 GeV^2 for the LEP1 SW sample, and 8.9 (10.7) and 17.5 (17.8) GeV^2 for the LEP1 FD (LEP2 SW) sample. and 10.6 and 17.7 GeV^2 for the LEP2 SW sample.

The results are compared with previous OPAL measurements of F_2^γ [13]–[15] in Figures 7.14 and 7.15. The measurements of F_2^γ using LEP1 data in bins with $\langle Q^2 \rangle = 1.9$ GeV^2 and $\langle Q^2 \rangle = 3.8$ GeV^2 are lower than the previous OPAL LEP1 results, which were unfolded using HERWIG 5.8d. Repeating the unfolding with HERWIG 5.8d gives results which are consistent with the old analysis, but with better precision. The HERWIG 5.8d Monte Carlo model has now been replaced by HERWIG 5.9+k_t(dyn), which gives a better description of the data. The LEP1 FD and LEP2 SW are generally consistent with each other and with previous OPAL results in the same Q^2 regions.

In Figures 7.16 and 7.17 the results are compared to measurements of F_2^γ from other experiments: TPC/2γ [7], PLUTO [3], TOPAZ [11], ALEPH [19], DELPHI [16] and L3 [17], [18]. At high x the new results are consistent with previous measurements. At lower x the L3 results are higher then the OPAL results, however as the L3 points are strongly correlated, the discrepancy looks larger in the plots than it actually is.

Also shown in Figures 7.16 and 7.17 are the GRV LO, SaS1D and WHIT1 parameterisations of F_2^γ, along with the QED quark parton model (QPM), for four active flavours with masses of 0.2 GeV for the light quarks and 1.5 GeV for the charm quark. The GRV LO and SaS1D parameterisations are consistent with the data in all accessible x and Q^2 regions except in the lowest Q^2 region where they are too low. The WHIT1 prediction is significantly higher than the data. The QPM model is not able to describe the data, falling too low at low x.

$\langle Q^2 \rangle$ [GeV^2]	sample	bin	x range	x	F_2^γ/α
1.9	LEP1 SW	I	$0.0006 < x < 0.0028$	0.0012	$0.269 \pm 0.027 \,^{+0.018}_{-0.034}$
		II	$0.0028 < x < 0.0143$	0.0063	$0.177 \pm 0.009 \,^{+0.017}_{-0.014}$
		III	$0.0143 < x < 0.0724$	0.0322	$0.179 \pm 0.007 \,^{+0.007}_{-0.006}$
		IV	$0.0724 < x < 0.3679$	0.1124	$0.227 \pm 0.010 \,^{+0.012}_{-0.012}$
3.7	LEP1 SW	I	$0.0015 < x < 0.0067$	0.0032	$0.269 \pm 0.033 \,^{+0.047}_{-0.033}$
		II	$0.0067 < x < 0.0302$	0.0143	$0.232 \pm 0.013 \,^{+0.023}_{-0.021}$
		III	$0.0302 < x < 0.1353$	0.0639	$0.259 \pm 0.010 \,^{+0.006}_{-0.013}$
		IV	$0.1353 < x < 0.6065$	0.1986	$0.296 \pm 0.014 \,^{+0.029}_{-0.022}$
8.9	LEP1 FD	I	$0.0111 < x < 0.0498$	0.0235	$0.221 \pm 0.017 \,^{+0.030}_{-0.026}$
		II	$0.0498 < x < 0.2231$	0.1054	$0.308 \pm 0.014 \,^{+0.011}_{-0.012}$
		III	$0.2231 < x < 0.8187$	0.3331	$0.379 \pm 0.022 \,^{+0.017}_{-0.015}$
10.7	LEP2 SW	I	$0.0009 < x < 0.0050$	0.0021	$0.362 \pm 0.045 \,^{+0.058}_{-0.039}$
		II	$0.0050 < x < 0.0273$	0.0117	$0.263 \pm 0.015 \,^{+0.032}_{-0.030}$
		III	$0.0273 < x < 0.1496$	0.0639	$0.275 \pm 0.011 \,^{+0.029}_{-0.030}$
		IV	$0.1496 < x < 0.8187$	0.3143	$0.351 \pm 0.012 \,^{+0.025}_{-0.016}$
17.5	LEP1 FD	I	$0.0235 < x < 0.0821$	0.0439	$0.273 \pm 0.028 \,^{+0.032}_{-0.039}$
		II	$0.0821 < x < 0.2865$	0.1534	$0.375 \pm 0.023 \,^{+0.020}_{-0.013}$
		III	$0.2865 < x < 0.9048$	0.3945	$0.501 \pm 0.027 \,^{+0.027}_{-0.019}$
17.8	LEP2 SW	I	$0.0015 < x < 0.0074$	0.0033	$0.428 \pm 0.061 \,^{+0.055}_{-0.071}$
		II	$0.0074 < x < 0.0369$	0.0166	$0.295 \pm 0.019 \,^{+0.033}_{-0.020}$
		III	$0.0369 < x < 0.1827$	0.0821	$0.336 \pm 0.013 \,^{+0.041}_{-0.042}$
		IV	$0.1827 < x < 0.9048$	0.3483	$0.430 \pm 0.013 \,^{+0.032}_{-0.025}$

Table 7.4: Results for F_2^γ/α as a function of x for four active flavours in six Q^2 regions. The first errors are statistical and the second systematic. The structure function was unfolded in bins defined by the x ranges and corrected to the x values given.

$\langle Q^2 \rangle$ [GeV^2]	sample	bin	x range	x	radiative correction	bin-centre correction
1.9	LEP1 SW	I	$0.0006 < x < 0.0028$	0.0012	-12.7	-4.2
		II	$0.0028 < x < 0.0143$	0.0063	-9.0	0.4
		III	$0.0143 < x < 0.0724$	0.0321	-7.1	1.8
		IV	$0.0724 < x < 0.3679$	0.1124	-6.0	4.7
3.7	LEP1 SW	I	$0.0015 < x < 0.0067$	0.0032	-11.8	-5.0
		II	$0.0067 < x < 0.0302$	0.0143	-8.9	0.6
		III	$0.0302 < x < 0.1353$	0.0639	-7.3	1.9
		IV	$0.1353 < x < 0.6065$	0.1986	-6.5	1.6
8.9	LEP1 FD	I	$0.0111 < x < 0.0498$	0.0235	-7.7	0.9
		II	$0.0498 < x < 0.2231$	0.1054	-6.3	2.4
		III	$0.2231 < x < 0.8187$	0.3331	-4.1	-0.9
10.7	LEP2 SW	I	$0.0009 < x < 0.0050$	0.0021	-12.5	-8.7
		II	$0.0050 < x < 0.0273$	0.0117	-7.3	-0.5
		III	$0.0273 < x < 0.1496$	0.0639	-4.4	3.2
		IV	$0.1496 < x < 0.8187$	0.3143	-2.2	-1.0
17.5	LEP1 FD	I	$0.0235 < x < 0.0821$	0.0439	-9.4	2.1
		II	$0.0821 < x < 0.2865$	0.1534	-7.9	2.5
		III	$0.2865 < x < 0.9048$	0.3945	-6.5	0.0
17.8	LEP2 SW	I	$0.0015 < x < 0.0074$	0.0033	-13.6	-8.2
		II	$0.0074 < x < 0.0369$	0.0166	-9.9	-0.5
		III	$0.0369 < x < 0.1827$	0.0821	-8.4	3.7
		IV	$0.1827 < x < 0.9048$	0.3483	-7.3	-0.4

Table 7.5: Corrections to the result as a function of x in bins of Q^2, as a percentage of the non-corrected F_2^γ. The radiative corrections were predicted by RADEG [49]. The bin-centre corrections are the average of the GRV LO and SaS1D predictions for the correction from the average F_2^γ over the bin to the value of F_2^γ at the nominal x position. The x positions are at the log centre of the bins, except for the highest x bins, where they are at the the log centre of that portion of the bin below the charm threshold for $m_c = 1.5$ GeV.

$\langle Q^2 \rangle$=1.9 GeV^2 (LEP1 SW)

	I	II	III	IV
I	1.00			
II	-0.28	1.00		
III	0.03	-0.35	1.00	
IV	0.01	0.10	-0.48	1.00

$\langle Q^2 \rangle$=3.7 GeV^2 (LEP1 SW)

	I	II	III	IV
I	1.00			
II	-0.27	1.00		
III	0.02	-0.34	1.00	
IV	0.01	0.10	-0.52	1.00

$\langle Q^2 \rangle$=8.9 GeV^2 (LEP1 FD)

	I	II	III
I	1.00		
II	-0.02	1.00	
III	-0.12	-0.31	1.00

$\langle Q^2 \rangle$=10.7 GeV^2 (LEP2 SW)

	I	II	III	IV
I	1.00			
II	-0.32	1.00		
III	0.04	-0.29	1.00	
IV	0.00	0.06	-0.36	1.00

$\langle Q^2 \rangle$=17.5 GeV^2 (LEP1 FD)

	I	II	III
I	1.00		
II	-0.09	1.00	
III	-0.09	-0.35	1.00

$\langle Q^2 \rangle$=17.8 GeV^2 (LEP2 SW)

	I	II	III	IV
I	1.00			
II	-0.35	1.00		
III	0.05	-0.33	1.00	
IV	-0.01	0.09	-0.41	1.00

Table 7.6: Statistical correlations between the x bins for each sample. The numerals refer to the bins listed in Table 7.4.

Q^2 [GeV^2]	x	F_2/α	statistical error	total systematic +	total systematic -	MC modelling	unfolding method	unfolding bias	W factor +	W factor -	E_{tag}min +	E_{tag}min -	θ_{tag}min	θ_{tag}max	W_{vis}min	W_{vis}max -	W_{vis}max +	$E_a$max -	$E_a$max +	phi region	calibration +	calibration -	ECAL scale +	ECAL scale -	background +	background -	bin centre
1.9	0.0012	0.269	10	6.6	12.8	0.18	0	-2.01	4.37	-9.08	0	0	-4.83	0	0	1.42	0.81	-3.03	0	0	-5.61	3.36	-3.26	2.1	1.33	-1.72	1.54
	0.0063	0.177	5.1	9.6	8	-7.11	1.73	0	-1.51	1.01	-2.78	5.94	0	0	0	-0.19	-0.17	-1.54	0	0	0.03	-0.19	-1.08	1.28	-0.03	0.01	0.05
	0.0321	0.179	3.8	4.1	3.6	-3.49	0	0	1.19	0	0	0.12	0	0	0	0.05	0.04	0.3	0.05	0	-0.25	0.65	-0.78	1.66	0.04	-0.03	0.02
	0.1124	0.227	4.2	5.4	5.3	3.39	-2.36	0	-2.06	0	0.48	-0.56	0	0	3.62	-0.02	-0.01	-0.19	-0.04	0	1.8	-1.71	0.65	-1.73	-0.02	0.02	0.45
3.7	0.0032	0.269	12.2	17.3	12.4	-4.23	0	11.9	8.31	-1.62	0	0	0	0	0	-9.83	-1.42	4.7	0	0	-3.18	4.06	-3.51	4.53	2.77	-3.55	1.36
	0.0143	0.232	5.6	10	9.2	-8.29	4.28	0	0	-0.61	0	0	0	-2.43	0.98	1.58	0.22	-1.47	0.1	0	-2.18	2.69	-1.41	1.22	0.12	-0.27	0.35
	0.0639	0.259	3.9	2.4	4.9	-0.5	-0.84	-3.35	0	0	0	-0.92	0	0.15	0	-0.36	-0.07	0.6	-0.16	0	-2.35	1.94	-2.37	1.25	-0.01	0.04	0.1
	0.1986	0.296	4.6	9.9	7.3	6.59	-1.68	6.01	-1.01	0	0	0.32	0	0	0	0.17	0.01	-0.26	0	0	-1.67	2.21	3.71	-1.71	-0.01	-0.02	0.54
8.9	0.0235	0.221	7.6	13.5	11.6	-10.5	0	3.85	6.41	1.95	-1.65	0	0	0	-0.96	0	0.01	-1.02	0	0	-2.12	1.29	-2.68	2.31	2.14	-2.76	0.84
	0.1054	0.308	4.6	3.6	3.9	0.64	-2.68	0	0	-2.05	0	0	2.47	0	0.53	0	0	0	0	0	-0.42	0.62	-1.75	2.29	-0.36	0.46	0.06
	0.3331	0.379	5.8	4.5	4	-2.63	1.67	0	0	1.04	0	0	0	0	0	0	0	0	0.08	0	-0.24	-0.74	3.04	-2.91	0.13	-0.22	0.37
10.7	0.0021	0.362	12.3	16.1	10.7	-1.21	0	0	4.23	-3.94	-5.05	9.62	3.5	0	0	0	3.45	0	4.08	7.41	-8.11	6.85	-2.34	0.27	0	0	1.54
	0.0117	0.263	5.8	12.3	11.6	-9.85	5.28	3.68	0	0	0	0	-5.96	0	0.35	0	-0.4	0	0	3.27	0.67	-0.22	-0.86	1.3	0	0	0.5
	0.0639	0.275	4	10.4	10.8	-9.14	0	-4.5	0	0	-2.17	0.64	4.44	0	-2.32	0	0.09	0	0	1.14	0.83	-0.45	-1.5	1.64	0	0	0.41
	0.3143	0.351	3.5	7	4.5	-3.68	0	0	0	0	0	0	2.74	0	3.87	0	-0.05	0.02	0	2.57	1.74	-1.83	1.76	-1.87	0	0	0.17
17.5	0.0439	0.273	10.4	11.8	14.4	-8.93	0	0	0	-1.21	-3.38	0	0	2.55	0.95	-0.32	-0.03	0	-6.56	0	-3.43	2.75	-2.29	3.87	5.23	-7.45	0.96
	0.1534	0.375	6.1	5.4	3.6	-1.34	0	3.25	0	0	0.52	1.26	0	0.66	0	0.23	-0.02	-0.92	1.25	0	-2.48	3.06	-1.99	1.75	-0.14	-0.27	0.03
	0.3945	0.501	5.4	5.3	3.8	-0.78	-1.33	-1.54	0	0	0	0	0	0	3.71	-0.11	-0.02	0	0	0	-2.72	2.76	1.53	-1.61	-0.05	0.25	1.42
17.8	0.0033	0.428	14.2	12.8	16.7	-2.22	-2.88	-2.91	0	0	-15.1	2.33	0	0	-0.57	0	0	2.89	0	0.68	-5.28	11.84	-1.03	1.26	0	0	1.33
	0.0166	0.295	6.4	11.2	6.8	-5.79	6.79	0	2.84	0	2.04	1.95	0	-0.78	1.03	0	0.52	0	0	4.49	-3.41	2.63	-0.99	0.99	0	0	0.81
	0.0821	0.336	3.9	12.3	12.6	-11.6	-1.87	0	-0.19	0	-1.68	0	0	0	-2.66	0	-0.08	-0.48	0.43	-1.05	-2.41	3.32	-2.25	2.46	0	0	0.52
	0.3483	0.43	2.9	7.5	5.9	-3.7	0	0	0	0	-0.19	0.18	0	-3.29	5.65	0	0.02	0.18	-0.12	0.85	-2.47	2.46	1.86	-2.04	0	0	0.7

Table 7.7: Systematic errors for F_2^γ/α as a function of x in bins of Q^2. The statistical error and the contributions to the systematic error from each of the sources are listed as percentages of F_2^γ/α. The systematic errors are corrected for the expected statistical component as described in the text. They are summed in quadrature separately for positive and negative deviations, except for 'MC modelling' and 'bin centre' which are symmetric.

experiment	E_{cm} [GeV]	$\langle Q^2 \rangle$ [GeV^2]	x range	reference
OPAL	91	1.9	0.0044–0.07	[14]
L3	91	1.9	0.0035–0.075	[17]
PLUTO	34.6	2.4	0.063–0.535	[3]
TPC/2γ	29	2.8	0.04–0.4515	[7]
OPAL	91	3.8	0.01315–0.15	[14]
PLUTO	34.6	4.3	0.1–0.62	[3]
L3	91	5.0	0.0075–0.15	[17]
TPC/2γ	29	5.1	0.11–0.5495	[7]
TOPAZ	58	5.1	0.043–0.138	[11]
PLUTO	34.6	5.3	0.0535–0.745	[3]
OPAL	91	7.5	0.046–0.466	[13]
OPAL	161/172	9.0	0.06–0.425	[15]
PLUTO	34.6	9.2	0.145–0.72	[3]
ALEPH	91	9.9	0.0425–0.6	[19]
L3	183	10.8	0.055–0.25	[18]
DELPHI	91	12.0	0.0235–0.2335	[16]
OPAL	161/172	14.5	0.06–0.425	[15]
OPAL	91	14.7	0.0715–0.679	[13]
L3	183	15.3	0.055–0.4	[18]
TOPAZ	58	16.0	0.085–0.555	[11]
ALEPH	91	20.7	0.0645–0.695	[19]
DELPHI	91	22.0	0.03–0.5	[16]
TASSO	34	23.0	0.1–0.9	[6]
L3	183	23.1	0.055–0.4	[18]
JADE	33.6	24.0	0.05–0.75	[5]

Table 7.8: Measurements of F_2^γ at $Q^2 < 30$ GeV^2. The x ranges refer to the centres of the extreme bins.

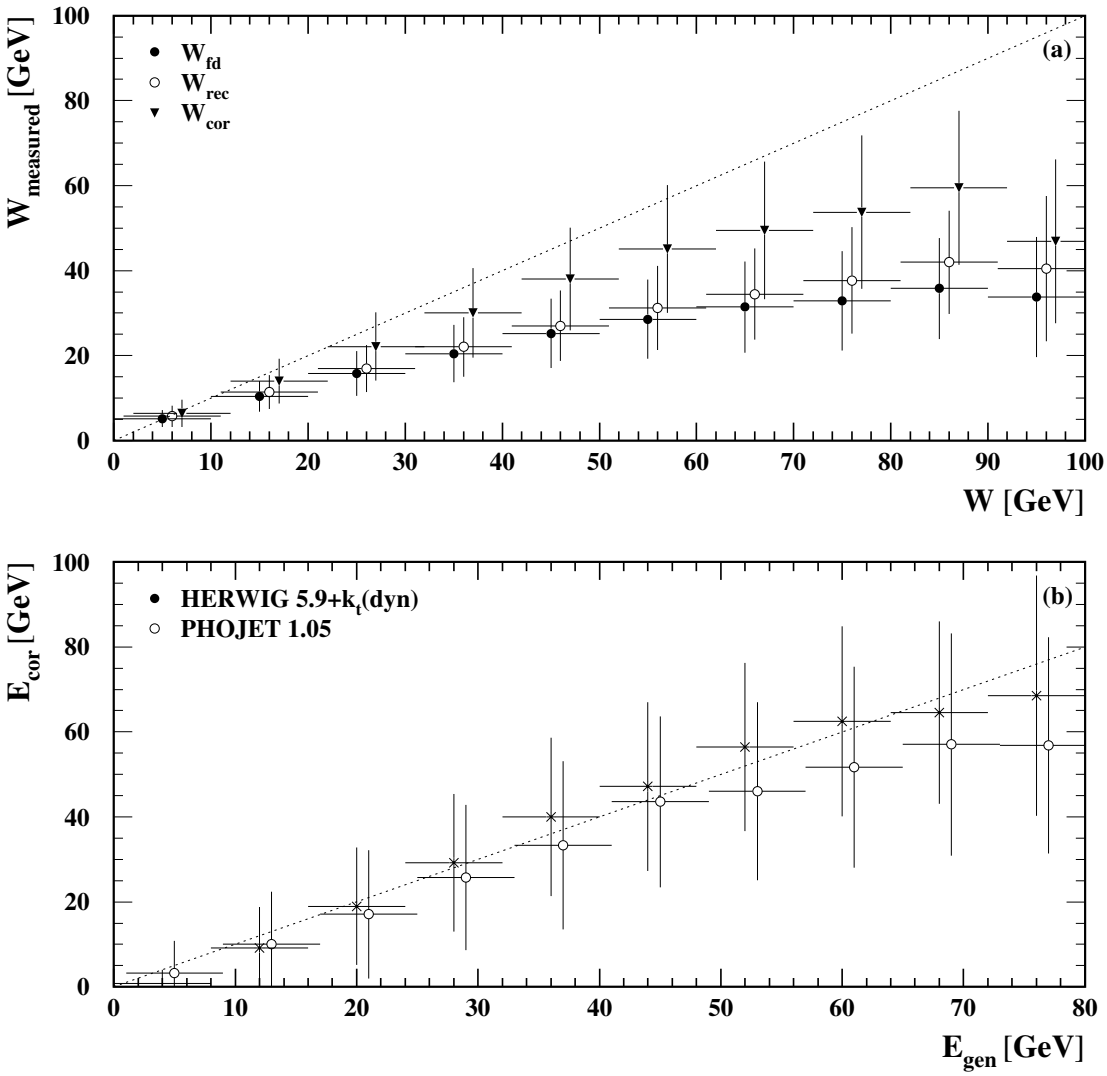

Figure 7.1: (a) The correlation between the generated and measured invariant mass, W, for the HERWIG 5.9+k_t(dyn) LEP2 SW Monte Carlo sample, using, $W_{\rm fd}$, $W_{\rm rec}$ and $W_{\rm cor}$. (b) The corrected energy, $E_{\rm cor}$, (2.5 times the visible energy) in the forward region against the total generated energy, $E_{\rm gen}$, deposited in that region, for the same sample as in plot a).

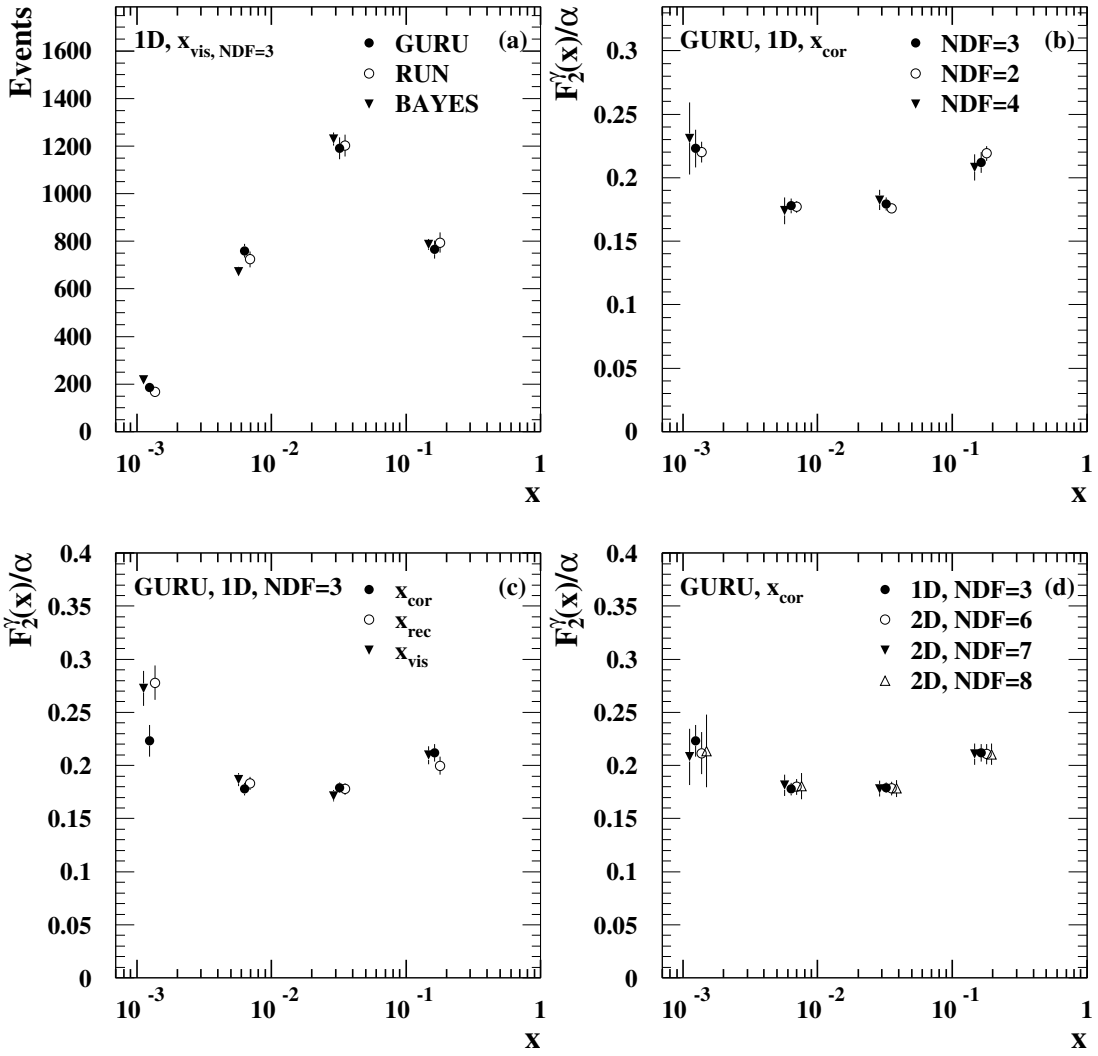

Figure 7.2: Tests of the unfolding procedure. The errors are statistical only. (a) Changing degrees of freedom with one dimensional unfolding. (b) RUN compared to GURU, for LEP1 SW data unfolded with the HERWIG 5.9+k_t(dyn) Monte Carlo sample. (c) Degrees of freedom with two-dimensional unfolding using a random number as the second variable. (d) Different measured x variables with one dimensional unfolding.

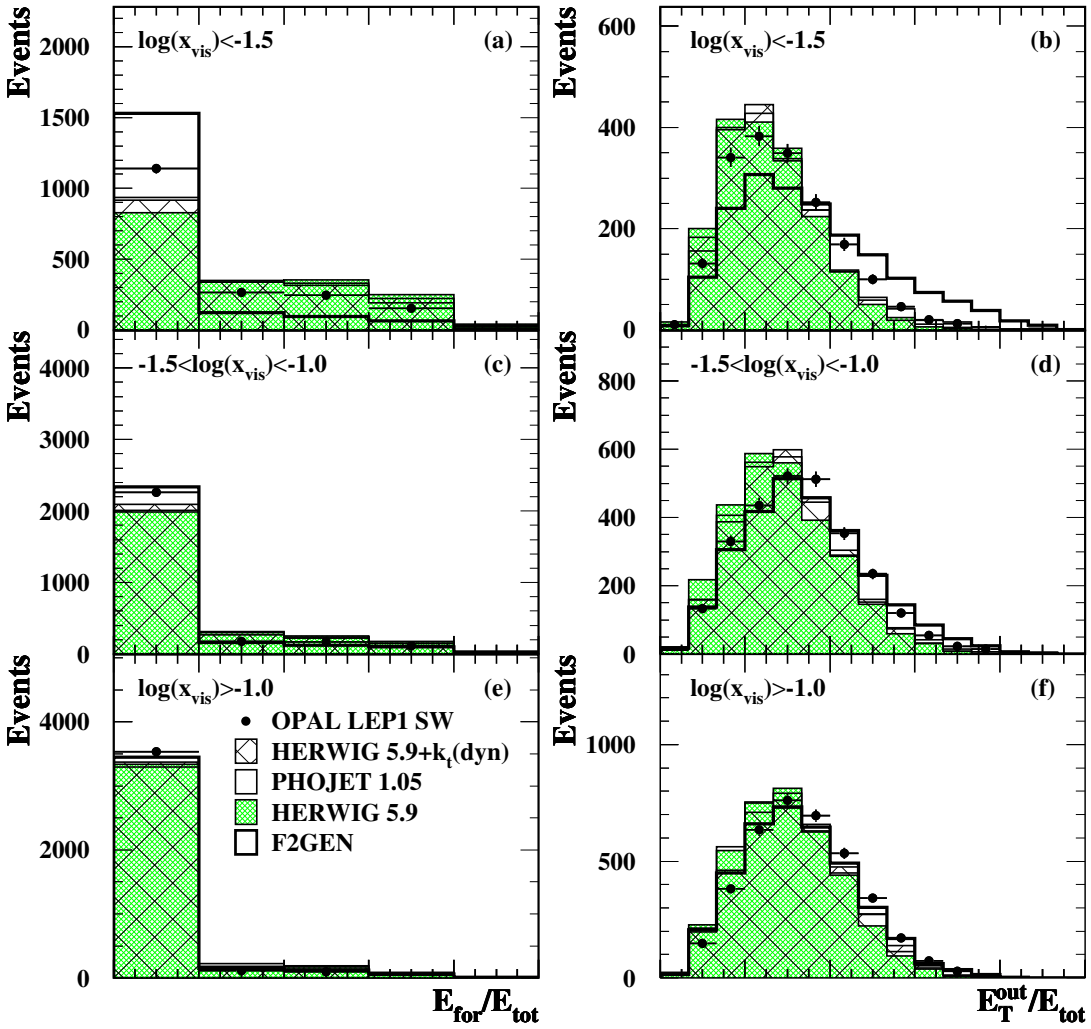

Figure 7.3: Data and Monte Carlo distributions for the variables used for two-dimensional unfolding, for the LEP1 SW sample divided into three bins of $x_{\rm vis}$. Plots a) c) and e) show $E_{\rm for}/E_{\rm total}$, the observed energy in the forward regions divided by the total observed energy. Plots b) d) and f) show $E_{\rm T}^{\rm out}/E_{\rm total}$, defined as the component of hadronic energy out of the plane of the tagged electron, divided by the total observed energy.

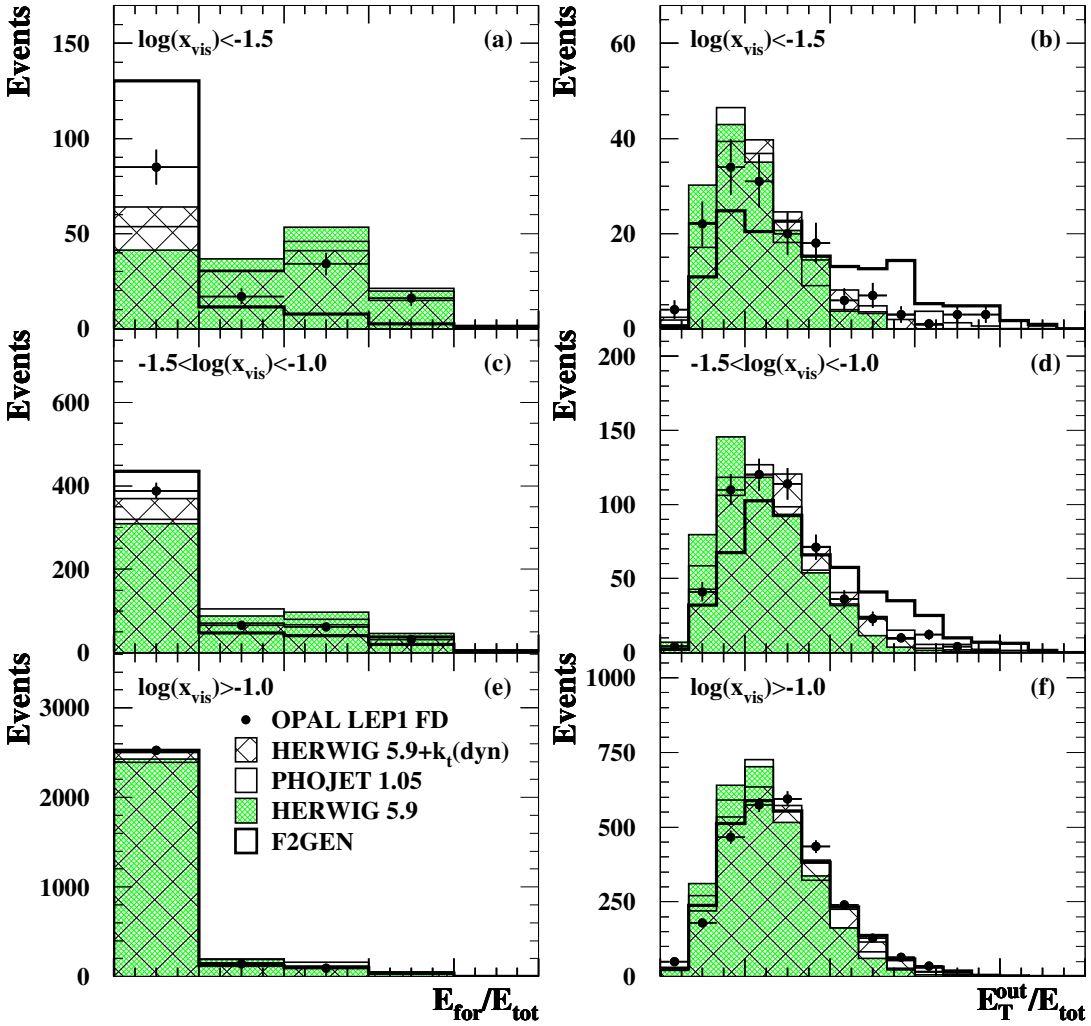

Figure 7.4: Data and Monte Carlo distributions for the variables used for two-dimensional unfolding, for the LEP1 FD sample divided into three bins of $x_{\rm vis}$. The variables are as defined in Figure 7.3.

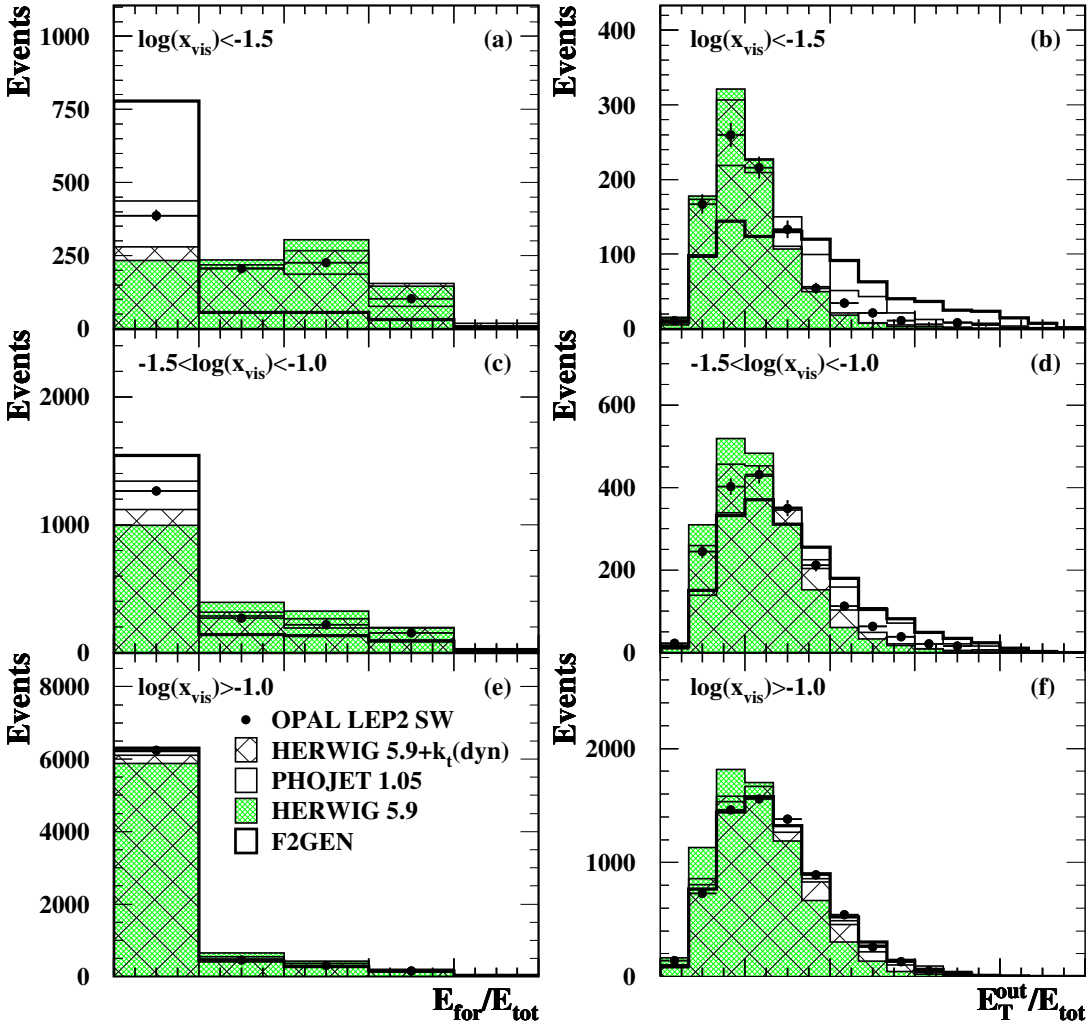

Figure 7.5: Data and Monte Carlo distributions for the variables used for two-dimensional unfolding, for the LEP2 SW sample divided into three bins of $x_{\rm vis}$. The variables are as defined in Figure 7.3.

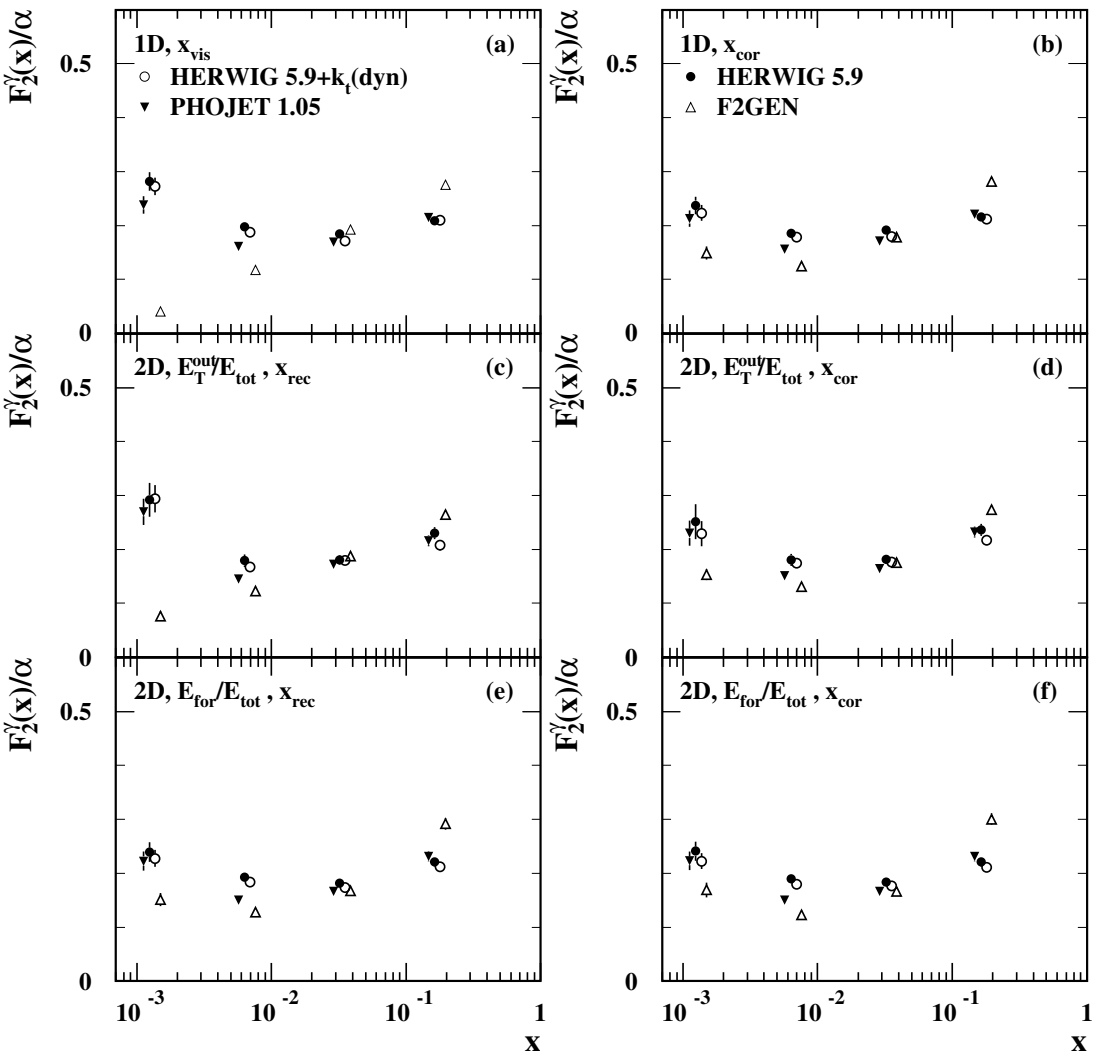

Figure 7.6: Unfolding of the LEP1 SW low Q^2 sample with 4 Monte Carlo models and different unfolding variables. The errors are statistical only. a) $x_{\rm vis}$, b) $x_{\rm cor}$, c) $x_{\rm rec}$ and $E_{\rm T}^{\rm out}$, d) $x_{\rm cor}$ and $E_{\rm T}^{\rm out}$, e) $x_{\rm rec}$ and $E_{\rm for}/E_{\rm total}$, f) $x_{\rm cor}$ and $E_{\rm for}/E_{\rm total}$.

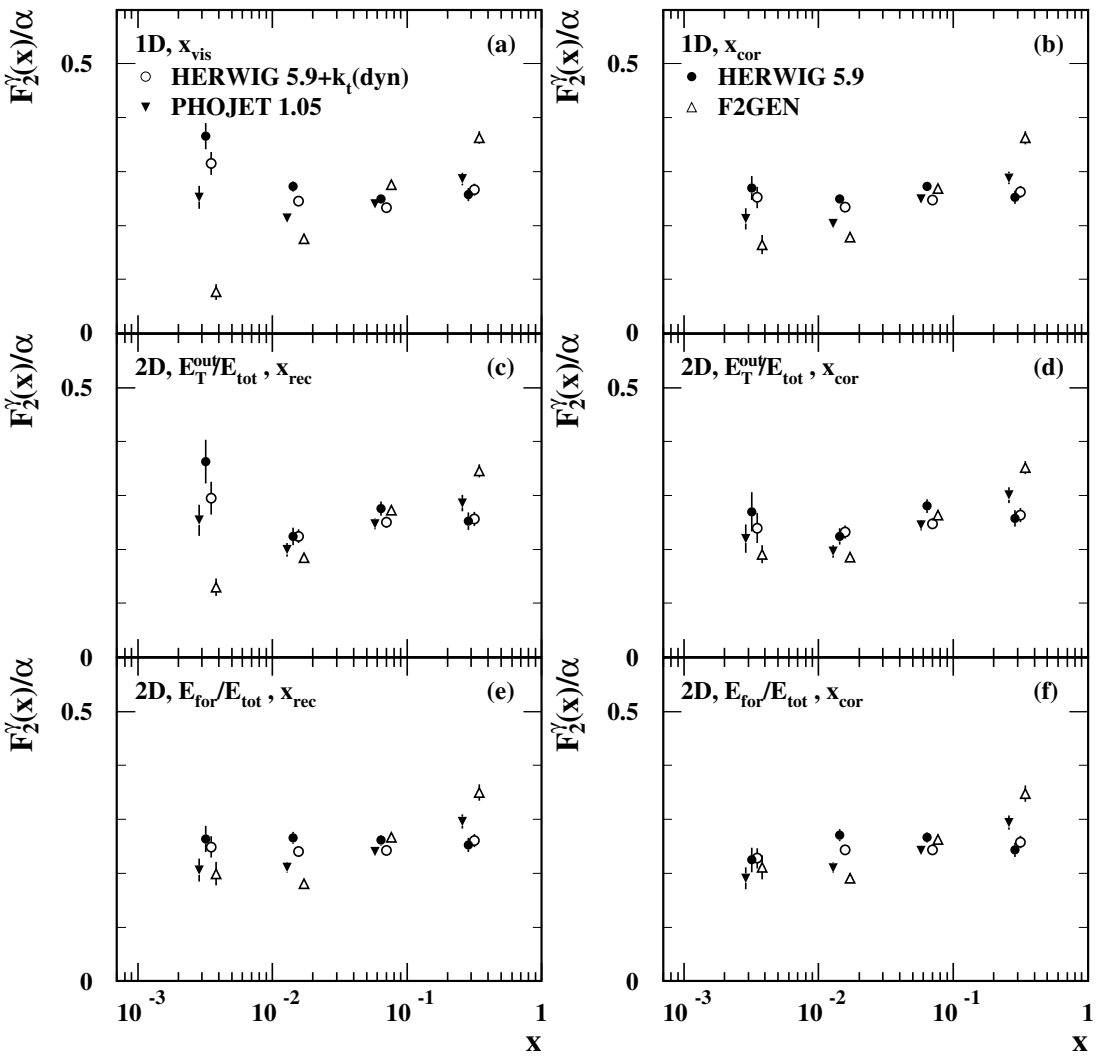

Figure 7.7: Unfolding of the LEP1 SW high Q^2 sample with 4 Monte Carlo models and different unfolding variables. The errors are statistical only. a) $x_{\rm vis}$, b) $x_{\rm cor}$, c) $x_{\rm rec}$ and $E_{\rm T}^{\rm out}$, d) $x_{\rm cor}$ and $E_{\rm T}^{\rm out}$, e) $x_{\rm rec}$ and $E_{\rm for}/E_{\rm total}$, f) $x_{\rm cor}$ and $E_{\rm for}/E_{\rm total}$.

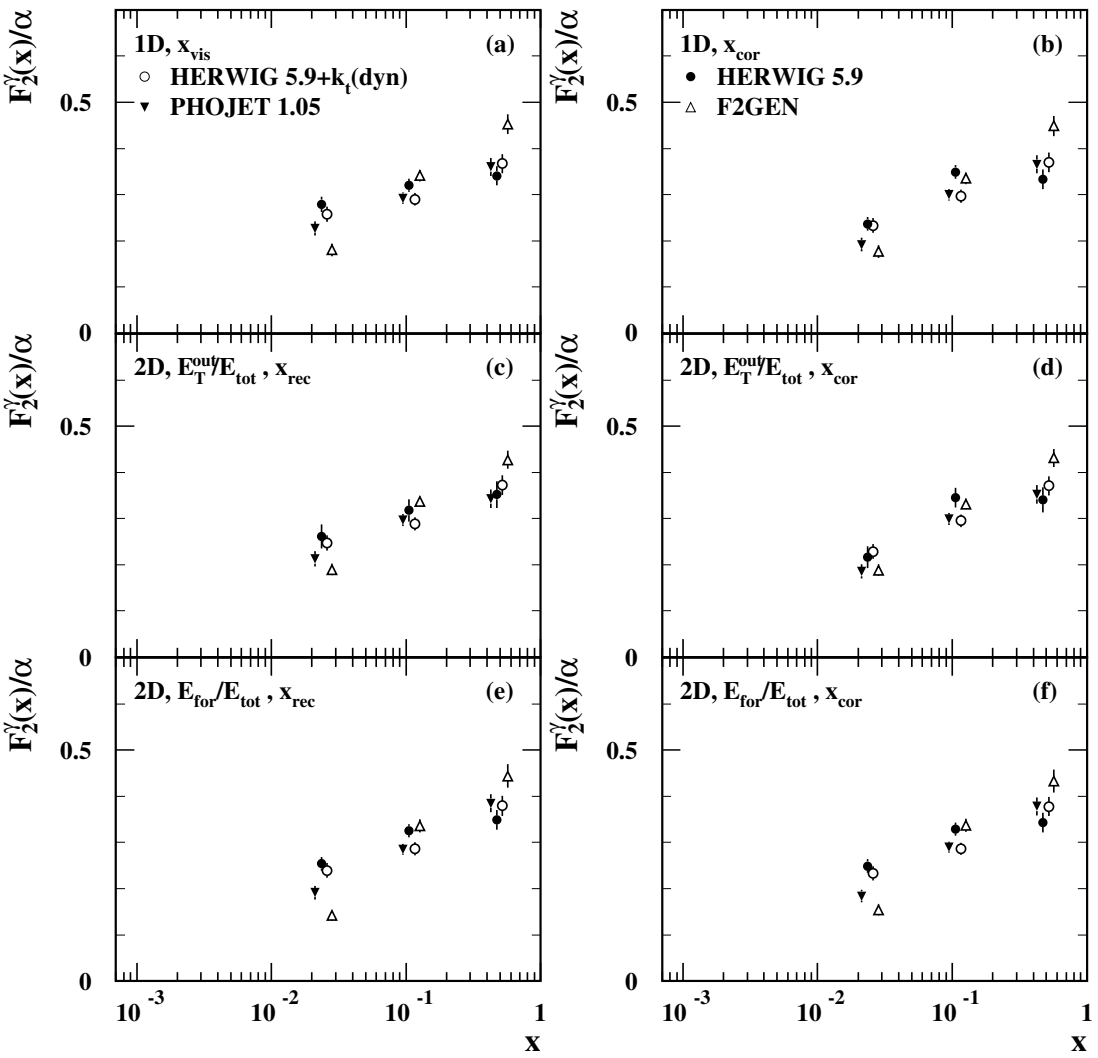

Figure 7.8: Unfolding of the LEP1 FD low Q^2 sample with 4 Monte Carlo models and different unfolding variables. The errors are statistical only. a) $x_{\rm vis}$, b) $x_{\rm cor}$, c) $x_{\rm rec}$ and $E_{\rm T}^{\rm out}$, d) $x_{\rm cor}$ and $E_{\rm T}^{\rm out}$, e) $x_{\rm rec}$ and $E_{\rm for}/E_{\rm total}$, f) $x_{\rm cor}$ and $E_{\rm for}/E_{\rm total}$.

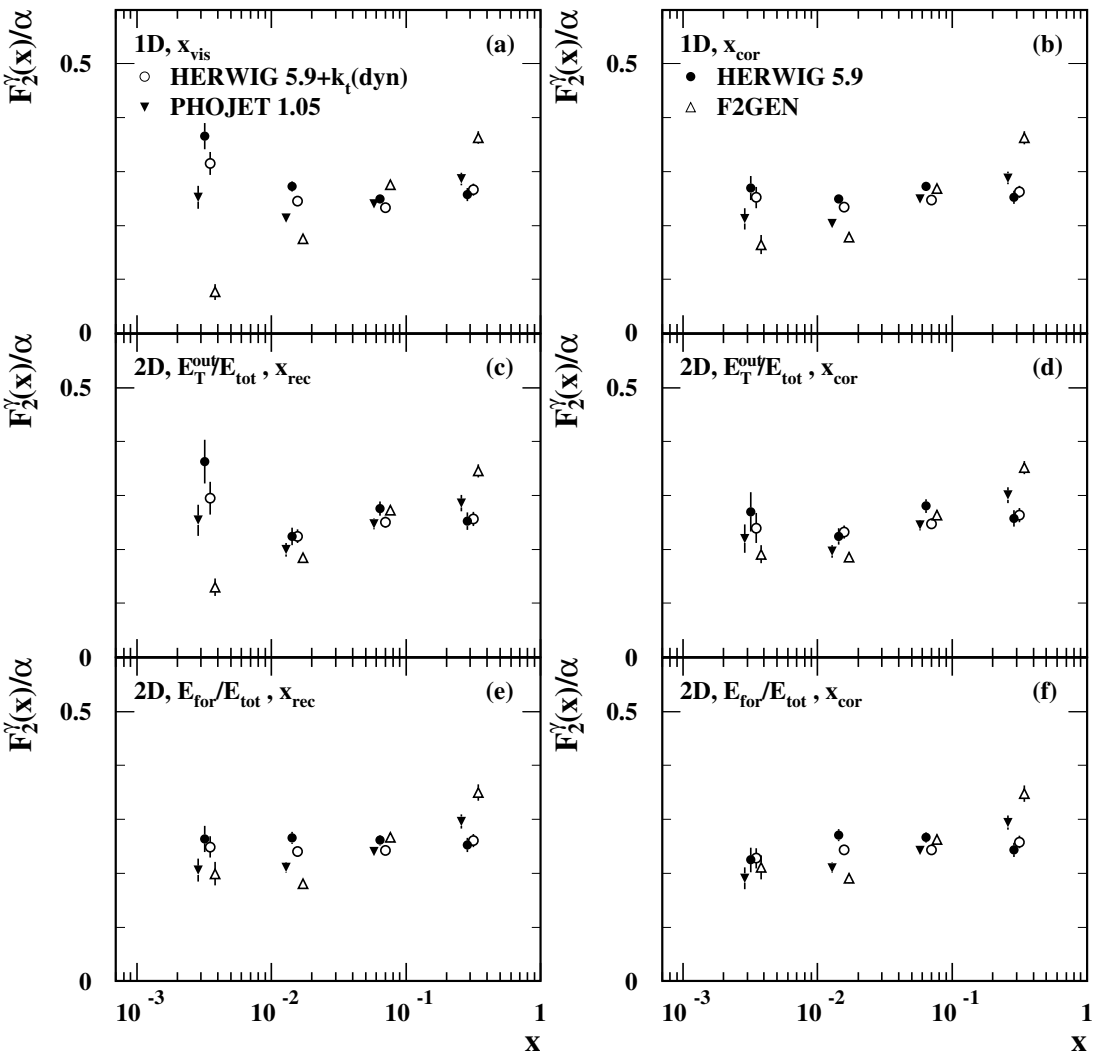

Figure 7.9: Unfolding of the LEP1 fd high Q^2 sample with 4 Monte Carlo models and different unfolding variables. The errors are statistical only. a) $x_{\rm vis}$, b) $x_{\rm cor}$, c) $x_{\rm rec}$ and $E_{\rm T}^{\rm out}$, d) $x_{\rm cor}$ and $E_{\rm T}^{\rm out}$, e) $x_{\rm rec}$ and $E_{\rm for}/E_{\rm total}$, f) $x_{\rm cor}$ and $E_{\rm for}/E_{\rm total}$.

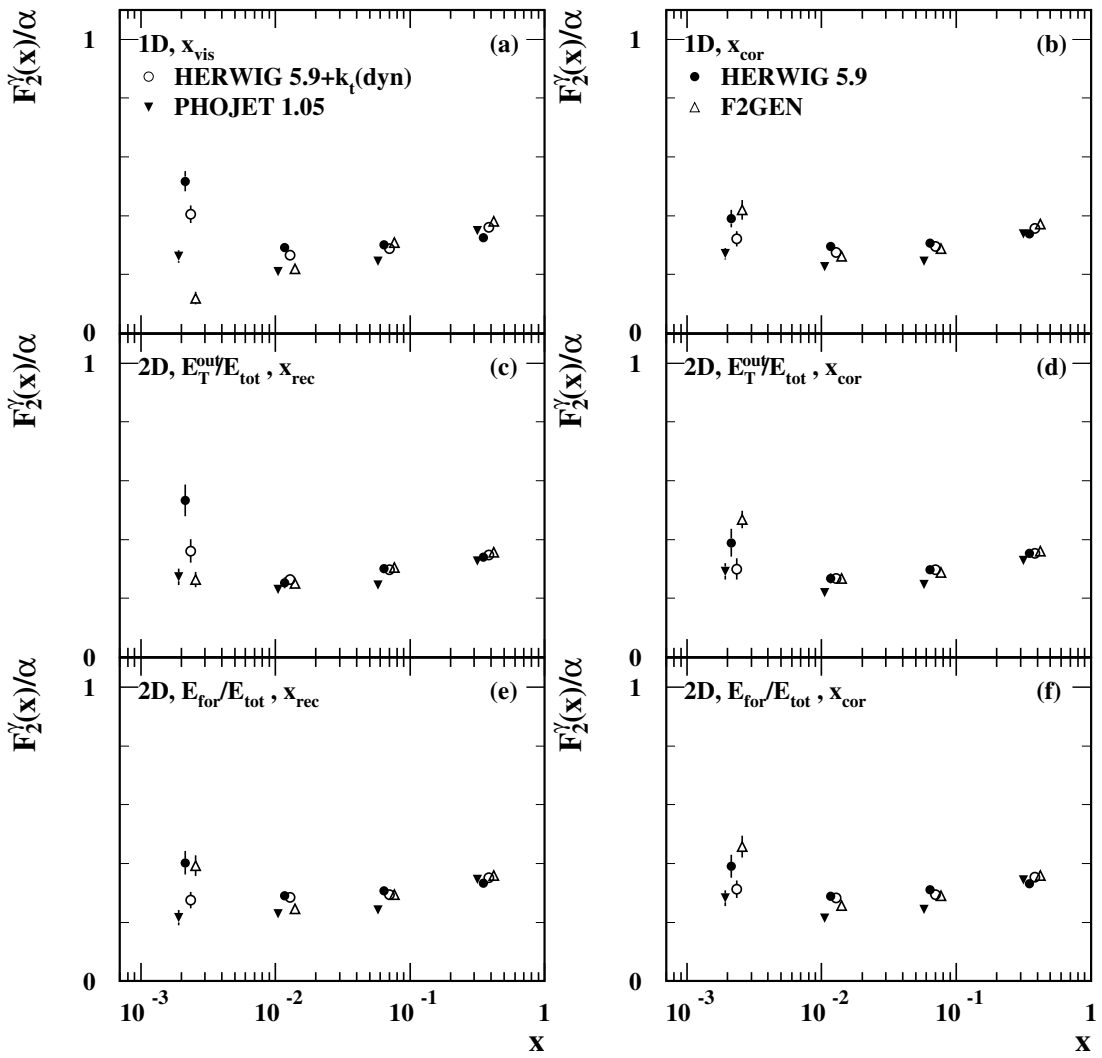

Figure 7.10: Unfolding of the LEP2 SW low Q^2 sample with 4 Monte Carlo models and different unfolding variables. The errors are statistical only. a) $x_{\rm vis}$, b) $x_{\rm cor}$, c) $x_{\rm rec}$ and $E_{\rm T}^{\rm out}$, d) $x_{\rm cor}$ and $E_{\rm T}^{\rm out}$, e) $x_{\rm rec}$ and $E_{\rm for}/E_{\rm total}$, f) $x_{\rm cor}$ and $E_{\rm for}/E_{\rm total}$.

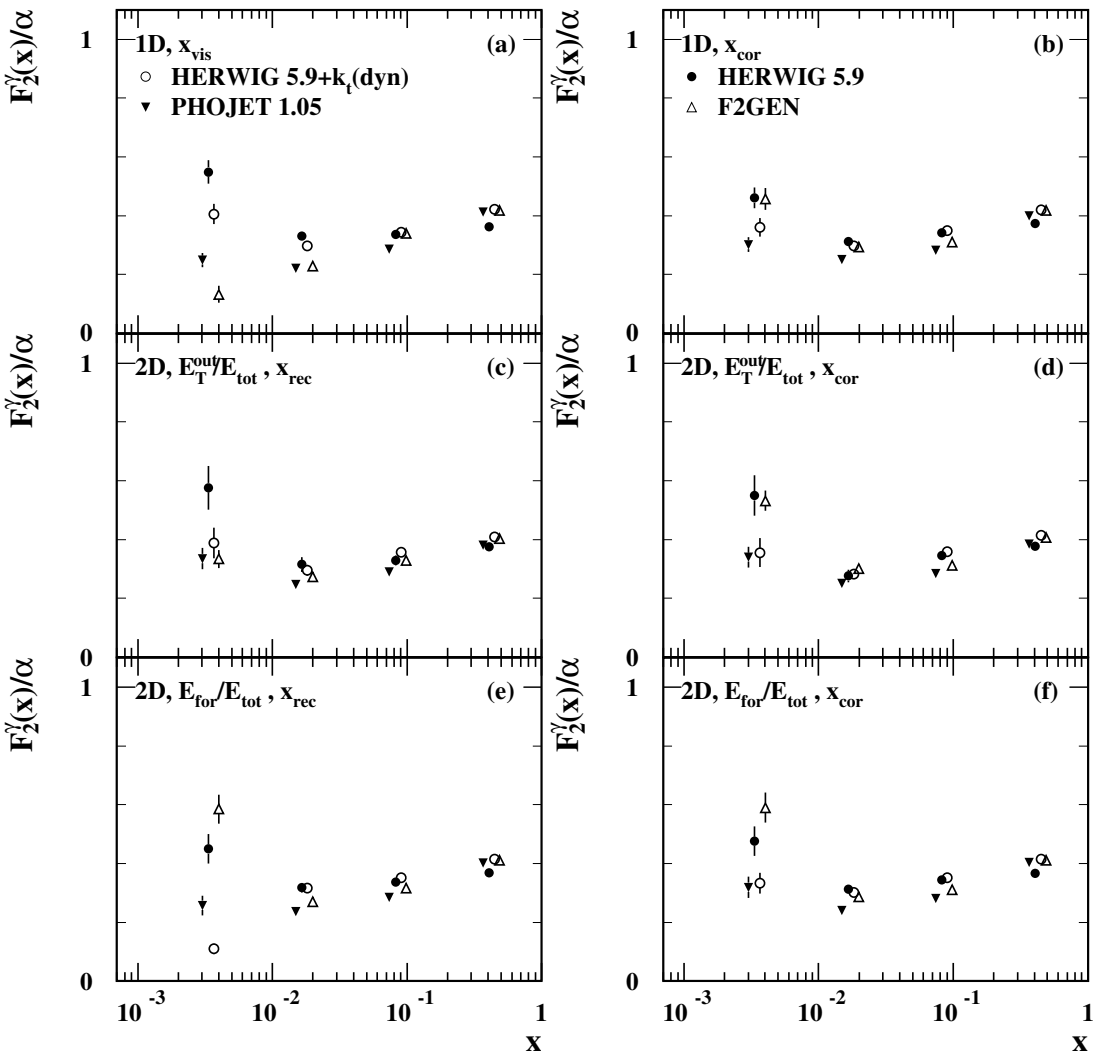

Figure 7.11: Unfolding of the LEP2 SW high Q^2 sample with 4 Monte Carlo models and different unfolding variables. The errors are statistical only. a) $x_{\rm vis}$, b) $x_{\rm cor}$, c) $x_{\rm rec}$ and $E_{\rm T}^{\rm out}$, d) $x_{\rm cor}$ and $E_{\rm T}^{\rm out}$, e) $x_{\rm rec}$ and $E_{\rm for}/E_{\rm total}$, f) $x_{\rm cor}$ and $E_{\rm for}/E_{\rm total}$.

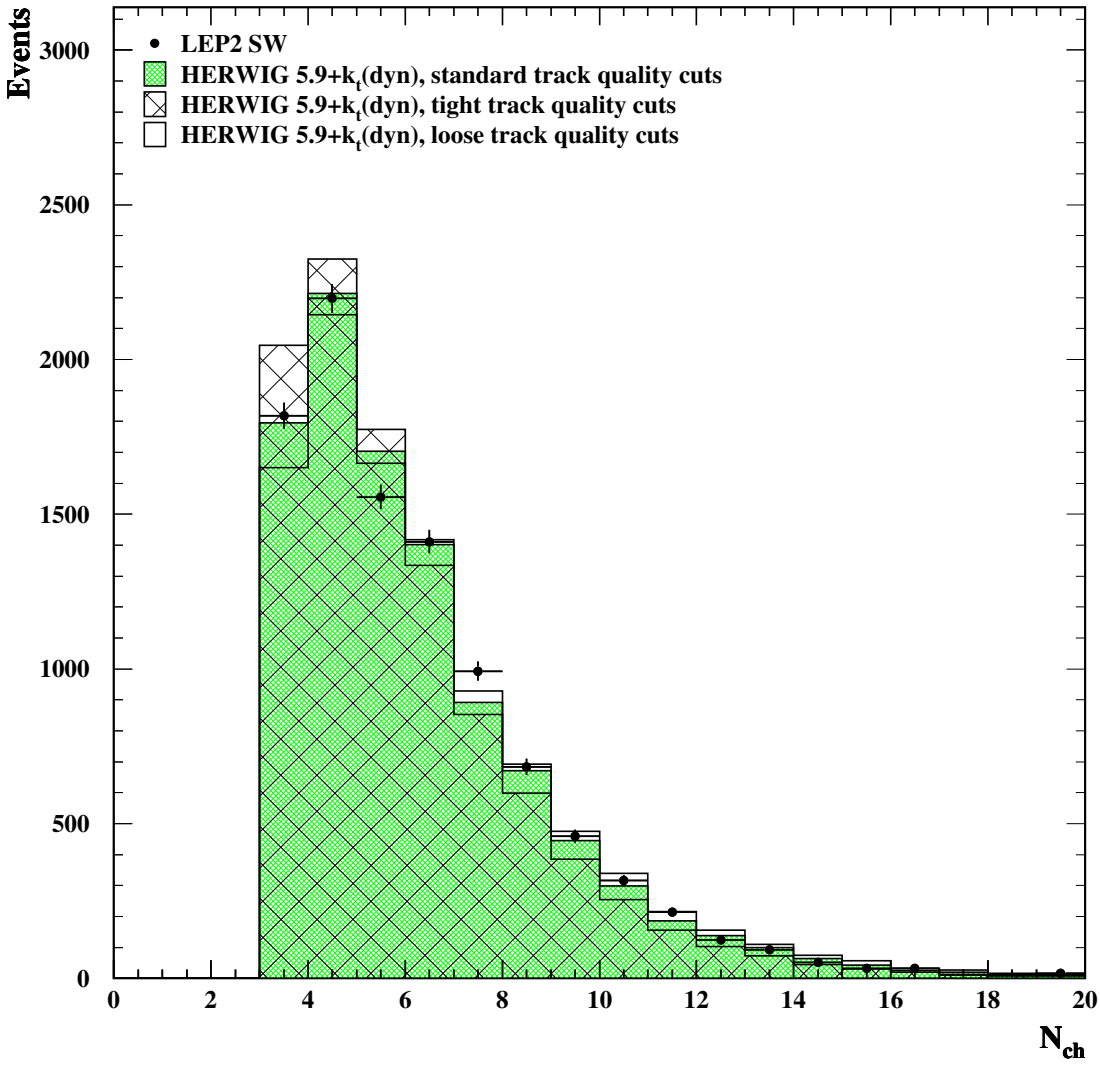

Figure 7.12: The effect of varying the track quality cuts on the $N_{\rm ch}$ distribution. To illustrate the change in shape, the Monte Carlo distributions are normalised to the same number of events as the data, rather than to the same luminosity.

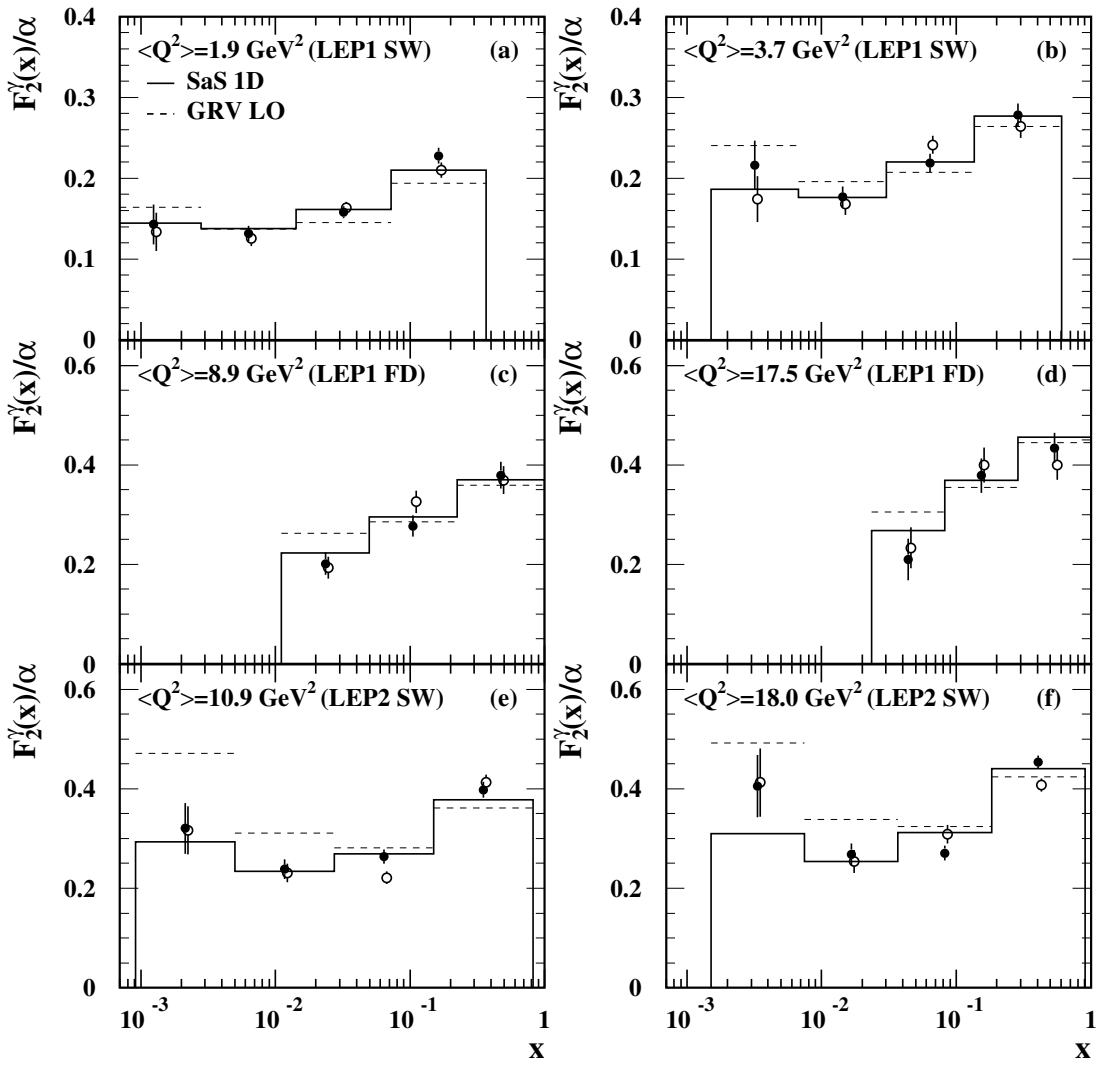

Figure 7.13: Two independent samples of Monte Carlo events generated using HERWIG 5.9 with the SaS1D structure function unfolded with HERWIG 5.9 with the GRV LO structure function, in six Q^2 ranges. The solid histogram shows the SaS1D structure function at the same average Q^2 as the sample in each plot, weighted by the x distribution in the HERWIG SaS1D sample (this is the quantity measured by Equation 6.42). The dotted lines show the GRV LO structure function weighted by the unfolded x distribution. The unfolded SaS1D samples were about the same size as the data samples in each Q^2 region. The errors are statistical only.

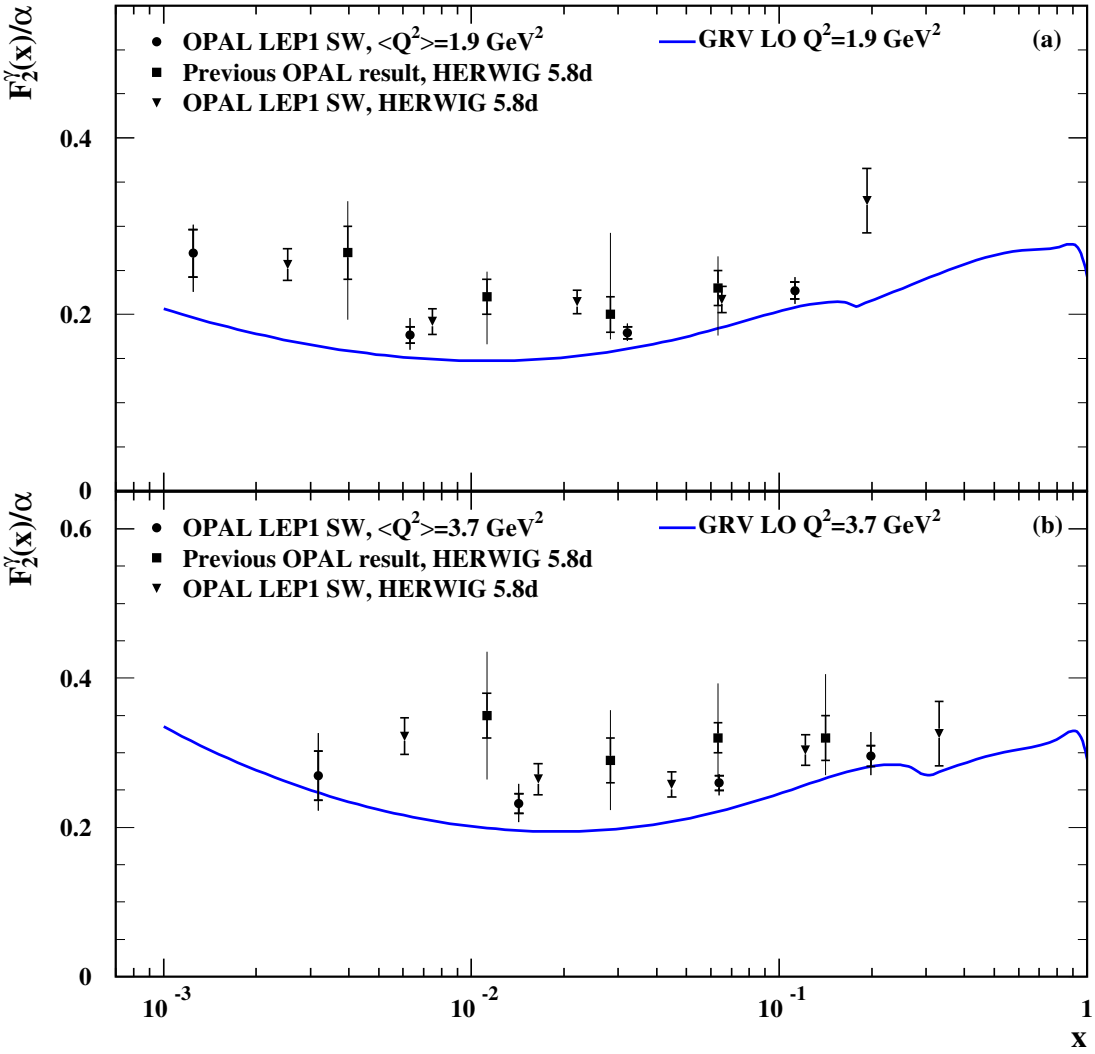

Figure 7.14: The measurement of F_2^γ/α using the LEP1 SW sample, for $\langle Q^2 \rangle$ values of (a) 1.9 and (b) 3.7 GeV^2. Also shown are the previous OPAL results in these Q^2 ranges, which were unfolded using HERWIG 5.8d, and the result of unfolding the LEP1 SW data using HERWIG 5.8d. For each point, the inner error bars show the statistical error and the full error bars show the total error, except for the new result with HERWIG 5.8d, for which only statistical errors are shown. The positions of the new OPAL points are as given in Table 7.4. The other points are shown at the centre of the $\log(x)$ bin. The curves show the GRV LO structure function.

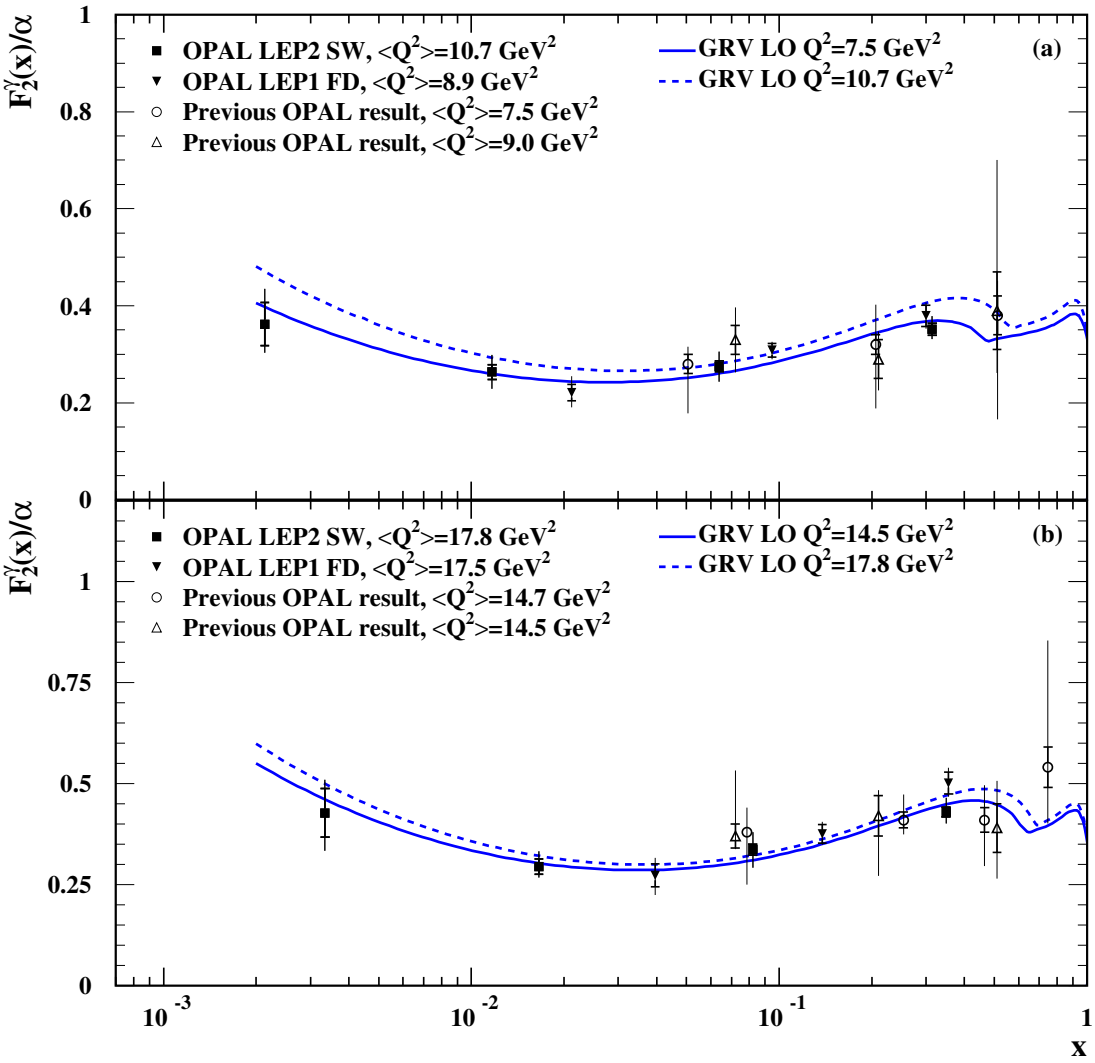

Figure 7.15: The measurement of F_2^γ/α using the LEP1 FD and LEP2 SW samples for $\langle Q^2 \rangle$ values of (a) 8.9 (10.7) and (b) 17.5 (17.8) GeV^2 for LEP1 (LEP2). Also shown are the previous OPAL results in these Q^2 ranges, which were unfolded with HERWIG 5.8d ($\langle Q^2 \rangle$=7.5 GeV^2 and $\langle Q^2 \rangle$=14.7 GeV^2) and HERWIG 5.9 ($\langle Q^2 \rangle$=9.0 GeV^2 and $\langle Q^2 \rangle$=14.5 GeV^2) using a linear x scale. For each point, the inner error bars show the statistical error and the full error bars show the total error. The positions of the new OPAL points are as given in Table 7.4. The other points with closed symbols are shown at the centre of the log(x) bin, and those with open symbols are shown at the average x value of the bin. The curves show the GRV LO structure function.

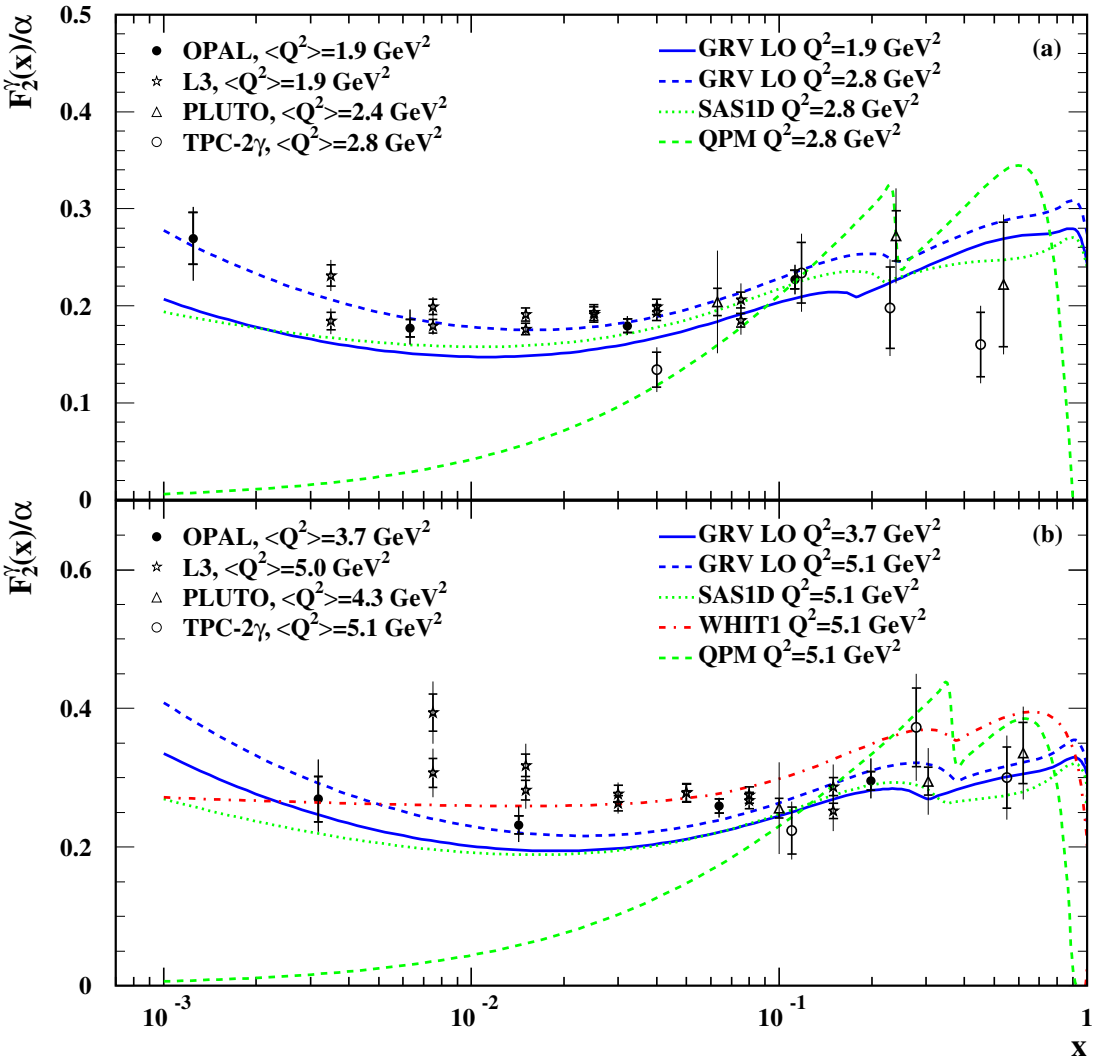

Figure 7.16: The measurement of F_2^γ/α using the LEP1 SW sample, for $\langle Q^2 \rangle$ values of (a) 1.9 and (b) 3.7 GeV^2. Also shown are the results from L3 [17], [18]. PLUTO [3], and TPC/2γ [7]. For L3 the two sets of points were unfolded using different Monte Carlo programs. The lower / upper points correspond to PHOJET 1.05 / TWOGAM. For each point, the inner error bars show the statistical error and the full error bars show the total error. The positions of the new OPAL points are as given in Table 7.4. The other points with closed symbols are shown at the centre of the log(x) bin, and those with open symbols are shown at the average x value of the bin. The curves show the GRV LO, SaS1D, WHIT1 and QPM structure functions.

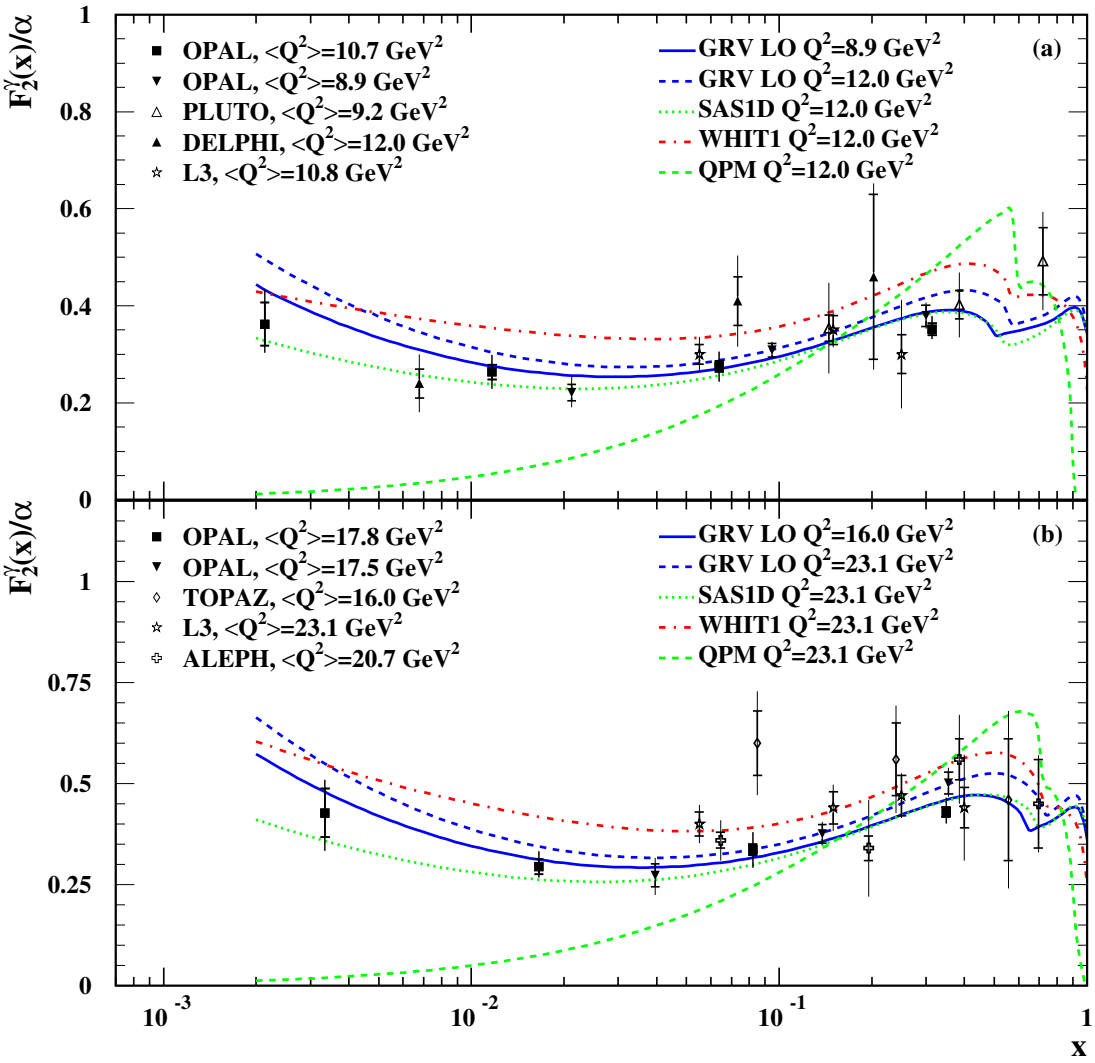

Figure 7.17: The measurement of F_2^γ/α using the LEP1 FD and LEP2 SW samples for $\langle Q^2 \rangle$ values of (a) 8.9 (10.7) and (b) 17.5 (17.8) GeV^2 for LEP1 (LEP2). Also shown is a selection of results from other experiments: ALEPH [19], DELPHI [16], L3 [17], [18], PLUTO [3], and TOPAZ [11]. For each point, the inner error bars show the statistical error and the full error bars show the total error. The positions of the new OPAL points are as given in Table 7.4. The other points with closed symbols are shown at the centre of the $\log(x)$ bin, and those with open symbols are shown at the average x value of the bin. The curves show the GRV LO, SaS1D, WHIT1 and QPM structure functions.

Chapter 8

Conclusions

The photon structure function F_2^γ has been measured using deep inelastic electron-photon scattering events recorded by the OPAL detector in the years 1993–1995 (LEP1) and 1998–1999 (LEP2), with centre-of-mass energies of 91 GeV, 183 GeV and 189 GeV. The data samples are separated into six ranges of Q^2, including two pairs of overlapping regions. The average Q^2 values of the samples are 1.9 and 3.8 GeV^2 for LEP1 SW, and 8.9 (10.7) and 17.5 (17.8) GeV^2 for LEP1 FD (LEP2 SW).

In previous OPAL studies of the photon structure function, it became clear that a large source of uncertainty in the measurement came from the Monte Carlo modelling of the hadronic final state of deep inelastic electron-photon scattering events. This is because it is necessary to correct for detector effects using Monte Carlo samples, by unfolding the true distribution of x. The modelling uncertainty was especially large at low values of x, where a large proportion of the hadronic energy is directed into the forward region, where it can be measured only by electromagnetic calorimeters, and some is lost in the beam pipe.

This is the first OPAL analysis to use the Monte Carlo programs PHOJET 1.05 and HERWIG 5.9+k_t(dyn). It was demonstrated in Chapter 4 that these

models give a better description of the hadronic final state than the programs which were used previously, HERWIG 5.9 and F2GEN.

The reconstruction of the invariant mass of the hadronic final state has been improved by including information from the deeply inelastically scattered electron, and by scaling the energy from the forward region to partially compensate for energy losses. Two-dimensional unfolding was introduced as a way to reduce the modelling error further. The ratio $E_{\mathrm{T}}^{\mathrm{out}}/E_{\mathrm{total}}$ was used as a second unfolding variable.

Three unfolding programs have been compared and shown to give consistent results for the central values, although the errors from one program (BAYES) are not always consistent with the other two. The method was tested by unfolding a Monte Carlo sample with another sample using a different input structure function. The correct structure function was recovered, within statistical errors.

The method for determining the systematic errors includes subtraction of the statistical component of each source of error, to avoid overestimating the error.

Monte Carlo modelling is still a large source of error, but no longer dominates all other sources as was the case in previous OPAL measurements of F_2^γ. The statistical and systematic errors are of similar size; therefore future analyses will have to reduce both in order to see substantial reductions in the total errors.

The GRV LO and SaS1D parameterisations are generally consistent with the OPAL data in all the accessible x and Q^2 regions. In the lowest Q^2 region, $\langle Q^2 \rangle = 1.9$ GeV^2, they are significantly lower than the data, though similar in shape. Although the results are not sufficiently precise to show a rise in the photon structure function at low x, they are consistent at low x with parameterisations which do have a rise.

In contrast, the naive quark-parton model is not able to describe the data for $x < 0.1$. These results show that the photon must contain a significant

hadron-like component at low x.

Bibliography

[1] SLAC-MIT Collaboration, G. Miller *et al.*, Phys. Rev. **D5** (1972) 528.

[2] PLUTO Collaboration, C. Berger *et al.*, Phys. Lett. **B107** (1981) 168.

[3] PLUTO Collaboration, C. Berger *et al.*, Phys. Lett. **B142** (1984) 111.

[4] PLUTO Collaboration, C. Berger *et al.*, Nucl. Phys. **B281** (1987) 365.

[5] JADE Collaboration, W. Bartel *et al.*, Phys. Lett. **B121** (1983) 203;
JADE Collaboration, W. Bartel *et al.*, Z. Phys. **C24** (1984) 231.

[6] TASSO Collaboration, M. Althoff *et al.*, Z. Phys. **C31** (1986) 527.

[7] TPC/2γ Collaboration, H. Aihara *et al.*, Z. Phys. **C34** (1987) 1;
TPC/2γ Collaboration, H. Aihara *et al.*, Phys. Rev. Lett. **58** (1987) 97.

[8] AMY Collaboration, T. Sasaki *et al.*, Phys. Lett. **B252** (1990) 491.

[9] AMY Collaboration, S.K. Sahu *et al.*, Phys. Lett. **B346** (1995) 208.

[10] AMY Collaboration, T. Kojima *et al.*, Phys. Lett. **B400** (1997) 395.

[11] TOPAZ Collaboration, K. Muramatsu *et al.*, Phys. Lett. **B332** (1994) 477.

[12] OPAL Collaboration, R. Akers *et al.*, Z. Phys. **C61** (1994) 199.

[13] OPAL Collaboration, K. Ackerstaff *et al.*, Z. Phys. **C74** (1997) 33.

[14] OPAL Collaboration, K. Ackerstaff *et al.*, Phys. Lett. **B412** (1997) 225.

[15] OPAL Collaboration, K. Ackerstaff *et al.*, Phys. Lett. **B411** (1997) 387.

[16] DELPHI Collaboration, P. Abreu *et al.*, Z. Phys. **C69** (1996) 223.

[17] L3 Collaboration, M. Acciarri *et al.*, Phys. Lett. **B436** (1998) 403.

[18] L3 Collaboration, M. Acciarri *et al.*, Phys. Lett. **B447** (1999) 147.

[19] ALEPH Collaboration, D. Barate *et al.*, Phys. Lett. **B458** (1999) 152.

[20] OPAL Collaboration, K. Ahmet *et al.*, Nucl. Instr. and Meth. **A305** (1991) 275;
P. P. Allport *et al.*, Nucl. Instr. and Meth. **A324** (1993) 34;
P. P. Allport *et al.*, Nucl. Instr. and Meth. **A346** (1994) 476;
B. E. Anderson *et al.*, IEEE Transactions on Nuclear Science **41** (1994) 845.

[21] G. Aguillion *et al.*, Nucl. Instr. and Meth. **417** (1998) 266.

[22] E. McKigney, *An Investigation of Singly and Doubly Tagged Photon-Photon Scattering Using the OPAL Detector at LEP*, PhD Thesis, University College London (1999).

[23] M. Arignon *et al.*, *The Trigger System of the OPAL Experiment at LEP*, OPAL Technical Note **TN036** (1991);
D. Robinson, *Computing in high energy physics: Proceedings*, Eds. C. Verkerk and W. Wojcik, CERN (1992).

[24] C. Berger and W. Wagner, Phys. Rep. **146** (1987) 1.

[25] R. Ellis, W. Stirling and B. Webber, *QCD and Collider Physics*, Cambridge (1996).

[26] E. Witten, Nucl. Phys. **B120** (1977) 189.

[27] OPAL Collaboration, G. Abbiendi *et al.*, Eur. Phys. J. **C11** (1999) 409.

[28] J. Badier *et al.*, Z. Phys **C18** (1983) 281.

[29] V. Gribov and L. Lipatov, Sov. J. Nucl. Phys. **15** (1972) 438;
L. Lipatov, Sov. J. Nucl. Phy. **20** (1975) 95;
Y. Dokshitzer, Sov. Phys. JETP **46** (1977) 641;
G. Altarelli, Phys. Rep. **81** (1982) 1.

[30] F. Halzen and A. Martin, *Quarks and Leptons*, Wiley (1984).

[31] H1 Collaboration, S. Aid *et al.*, Nucl. Phys. **B470** (1996) 3;
H1 Collaboration, C. Adloff *et al.*, Nucl. Phys. **B497** (1997) 3.

[32] ZEUS Collaboration, M. Derrick *et al.*, Z. Phys. **C72** (1996) 399;
ZEUS Collaboration, J. Breitweg *et al.*, Eur. Phys. J. **C7** (1999) 609.

[33] K. Hagiwara *et al.*, Phys. Rev. **D51** (1995) 3197.

[34] J.H. Field *et al.*, Z. Phys. **C36** (1987) 121.

[35] AMY Collaboration, S.K. Sahu *et al.*, Phys. Lett. **B346** (1995) 208.

[36] G.A. Schuler and T. Sjöstrand, Z. Phys. **C68** (1995) 607.

[37] H. Abramowicz *et al.*, Phys. Lett. **B269** (1991) 458.

[38] A. Vogt, *Proceedings of the workshop on Two-Photon Physics at LEP and HERA*, Eds. G. Jarlskog and L. Jönsson, Lund University (1994) 141.

[39] L.E. Gordon and J.K. Storrow. Z. Phys. **C56** (1992) 307.

[40] M. Glück, E. Reya and A. Vogt, Phys. Rev. **D46** (1992) 1973;
M. Glück, E. Reya and A. Vogt, Phys. Rev. **D45** (1992) 3986.

[41] V. Budnev *et al.*, Phys. Rep. **C15** (1995) 182.

[42] M. Glück, E. Reya and M. Stratmann, Phys. Rev. **D51** (1995) 3220;
M. Glück, E. Reya and M. Stratmann, Phys. Rev. **D54** (1996) 5515.

[43] G. Marchesini *et al.*, Comp. Phys. Comm. **67** (1992) 465.

[44] R. Engel, Z. Phys. **C66** (1995) 203;
R. Engel, J. Ranft, and S. Roesler, Phys. Rev. **D52** (1995) 1459;
R. Engel and J. Ranft, Phys. Rev. **D54** (1996) 4244.

[45] A. Buijs, W. G. J. Langeveld, M. H. Lehto and D. J. Miller, Comp. Phys. Comm. **79** (1994) 523.

[46] T. Sjöstrand, Comp. Phys. Comm. **39** (1986) 347;
T. Sjöstrand and M. Bengtsson, Comp. Phys. Comm. **43** (1987) 367;
T. Sjöstrand, Comp. Phys. Comm. **82** (1994) 74.

[47] B. R. Webber, Nucl. Phys. **B238** (1984) 492.

[48] B. Andersson *et al.*, Phys. Rep. **97** (1993) 31.

[49] E. Laenen and G.A. Schuler, Phys. Lett. **B374** (1996) 217;
E. Laenen and G.A. Schuler, Model-independent QED corrections to photon structure-function measurements, in *Photon '97, Incorporating the XIth International Workshop on Gamma–Gamma Collisions, Egmond aan Zee, 10-15 May, 1997*, edited by A. Buijs and F.C. Erné, pages 57–62, World Scientific, 1998.

[50] M. Landrø, K.J. Mork, and H.A. Olsen, Phys. Rev. **D36** (1987) 44;
F.A. Berends, P.H. Daverveldt, and R. Kleiss, Nucl. Phys. **B253** (1985) 441;
F.A. Berends, P.H. Daverveldt, and R. Kleiss, Comp. Phys. Comm. **40** (1986) 285.

[51] J. A. Lauber, L. Lönnblad and M. H. Seymour, *Tuning MC Models to fit DIS eγ Scattering Events*, Proceedings of Photon '97, 10-15 May 1997, Eds A. Buijs, F. C. Erné, World Scientific, (1997) 52;
A. Finch, J. A. Lauber, M. Lehto, M. H. Seymour, Phenomenology Workshop on LEP2 Physics, Oxford, England, 14-18 Apr 1997. J. Phys. **G24**, (1998) 457.

[52] ZEUS Collaboration, M. Derrick *et al.*, Phys. Lett. **B354** (1995) 163.

[53] T. Omori *et al.*, *The MT Manual*, unpublished.

[54] S. Jadach, B. F. L. Ward and Z. Wąs, Comp. Phys. Comm. **79** (1994) 503.

[55] J. A. M. Vermaseren, Nucl. Phys. **B229** (1983) 347.

[56] J. Fujimoto, *et al.*, Comp .Phys. Comm. **100** (1997) 128.

[57] J. Hilgart, R. Kleiss and F. Le Diberder, Comp. Phys. Comm. **75** (1993) 191.

[58] T. Sjöstrand, Comp. Phys. Comm. **82** (1994) 74;
T. Sjöstrand, *PYTHIA 5.7 and JETSET 7.4: Physics and Manual*, CERN-TH/93-7112 (1993).

[59] D. Karlen, Nucl. Phys. B289 (1987) 23.

[60] A. Höcker, V. Kartvelishvili, Nucl. Instr. and Meth. **A372** (1996) 469.

[61] V. Blobel, *Unfolding Methods in High-Energy Physics Experiments*, DESY-84-118 (1984);
V. Blobel, *Proceedings of the 1984 CERN School of Computing*, Aiguablava, Spain, 9–22 Sept. 1984, CERN 85-09;
V. Blobel, RUN, *Regularized Unfolding for High-Energy Physics Experiments, Program manual* (1996) unpublished.

[62] G. D'Agostini, Nucl. Instr. and Meth. **A362** (1996) 489.

[63] C. E. Lawson and R. J. Hanson, *Solving Least Square Problems*, Prentice-Hall, Englewood Cliffs (1974) Chapter 25, Section 4.

[64] L. Lönnblad *et al.*, CERN 96-01, Physics at LEP2, eds G. Altarelli, T. Sjöstrand and F. Zwirner (1996) Vol. 2, p. 201.

[65] S. Cartwright et al., J. Phys. **G24**, (1998) 457.

[66] OPAL Collaboration, K. Ackerstaff *et al.*, Eur. Phys. J. **C5** (1998) 411.